ΠΟΛΥΤΕΧΝΕΙΟ ΚΡΗΤΗΣ
TECHNICAL UNIVERSITY OF CRETE

ELECTRICAL AND COMPUTER ENGINEERING DEPARTMENT

A novel multi modal high throughput screening and material identification imaging system.

A THESIS SUBMITTED IN PARTIAL FULFILLMENT OF
THE REQUIREMENTS FOR THE DIPLOMA OF

ELECTRICAL AND COMPUTER ENGINEERING

THESIS COMMITTEE

Professor Balas Costas, *Thesis Supervisor*
Professor Bletsas Aggelos
Associate Professor Angelakis Dimitris

by

Christos Tsiaousis

July 2022

THIS PAGE INTENTIONALLY LEFT BLANK

Abstract

The curiosity-driven impulses of humanity have directed technologies to broaden biological senses, by enhancing the observation capabilities. Since the beginning of scientific evolution, researchers rely on such technologies to visualize new features of diagnostic importance. Demanding tasks with critical time constraints which portray the evolving society, brought the necessity of automation in research spotlight. Today's High Throughput Screening (HTS) technologies are prone to monolithic design, are deficient of a wide palette of imaging modalities and are fast approaching their identification capacity limits. Here, we present a novel Multi Modal (MM) HTS imaging system that overtakes the modality limits of traditional HTS apparatus, by introducing four different Hyper Spectral (HS) imaging modalities that uniquely fingerprint materials. The morphological and molecular structure of specimens is depicted using the Transmission, Reflection and Fluorescence modalities, while a contemporary Polarization imaging technique is used to depict the crystalline structure. Essential high throughput requirements for the latter are real-time and rotation independent measurements, which are achieved by an innovative Polarization State Generator (PSG) – Detector (PSD) design. This expands the identification capacity by generalizing data representation into a high dimensional Multi Modal Feature Space (MMFS). In this space there almost definitely exists a differentiation hyperplane that can separate seemingly similar materials. We leverage this property to demonstrate a new potential supervised classification method that relies on the multi modal feature space and indicate some examples that necessitate it.

Αφιερωμένη στην οικογενειά μου
τον Θανάση, την Ευδοκία, την Ιωάννα και την Μυρσίνη.

Contents

Chapter 1

Introduction

Summary

High throughput screening (HTS) is the use of **automated equipment** to rapidly test thousands to millions of samples for biological activity at the model organism, cellular, pathway, or molecular level. In its most common form, HTS is an experimental process in which small molecule compounds of known structure are screened in parallel. Other substances, such as chemical mixtures, natural product extracts, oligonucleotides, and antibodies, may also be screened. Because HTS typically aims to screen 100 000 or more samples per day, relatively simple and automation-compatible assay designs, robotic-assisted sample handling, and automated data processing are critical.

The electronics laboratory of Technical University of Crete is investing its know-how on the Multi Modal (MM) Hyper Spectral Imaging (HSI) to develop novel HTS technologies. Those technologies aim to broaden the application field of HTS to not only pharmaceutical and biotechnology companies but also many other research facilities that need to have **automated data processing** for variable -bigger- sized specimens.

Researchers dedicate huge amounts of time to **data gathering**. Traditionally, this would involve a person going through each sample individually, assessing and measuring the parameters of the sample, and then recording the quantitative or qualitative values. These values would then be entered into a database for **data analysis**. While this approach generates a great deal of knowledge and experience for the researcher, it also poses a number of challenges or difficulties, such as:

- For trials to be valid, a huge number of samples are required
- One must reproduce the results of those samples for statistical significance
- Trials, repeats, and spot-checking are time consuming for the researcher
- People are prone to making mistakes and after several hours of looking at samples, researchers may get "sample blindness" and this introduces a human error factor. When combined with tiredness or distractions, human error will also contribute to mistakes and misdiagnosis
- Observer bias. People score their samples based off of their own understanding and opinion. This can lead to variation in results if more than one person is reviewing samples

With automated image analysis, the risk of a person making a mistake or interpreting a result incorrectly is eliminated. Moreover, the need for manpower is reduced and the

overall research and processing throughput is maximized.

The HTS instrumentation development is a complex problem as it requires high precission hardware, motorised optics, real-time adjustments, high processing power, data management, resource efficiency while assuring good image quality by auto-focus, appropriate lighting and, ideally, self calibration. Images where samples are very clustered or out of focus are not impossible to work with, although these will require intervention from the researcher.

As of today, most HTS solutions aim to acquire the data in one image modality that yields the highest **contrast** (i.e. Fluorescence Microscopy). Having only one microscopy technique in an automatic device is sub-optimal due to the fact that the device is attached with the specimens that is inspecting and changing a field of interest makes a device modification compulsory and may be impossible. Some instrumentation on the market provide both Fluorescence and Transmission imaging, but only the respective color images are acquired. Thus, if the sample in similar in both **color images**, the need of stochastic software needs to classify two similar samples and this interpretation will lead to false positive - false negative results.

Over the recent years, a wide range of optical imaging modalities based on multiple observation techniques have emerged. The motivation behind this tendency is the fact that a single technique is often unable to provide all of the required information, given optimal temporal and spatial resolution. Complementary techniques are needed, in order to achieve a full understanding of the structural and biochemical changes that occur in cellulosic materials, as they undergo physical, chemical or biochemical processing. Introducing HSI and many imaging modalities to HTS instrumentation minimizes the probability of finding two different samples with the exact same optical features in all those different modalities across the spectrum.

By utilizing the HSI variants of Transmission, Fluorescence and Reflection modalities, a **Multi Modal Feature Space (MMFS)** is obtained for every sample and can be expressed mathematically. This process creates multidimensional spaces for every modality that signature (ground truth) vectors can be observed and relate uniquely to any sample. Each of those modalities serve a purpose for non-destructive chemical analysis of the compounds:

- **Transmission** imaging modality tackles the **molecular structure** of the sample and the intensity of the absorption, as a function of frequency, is the vector that differentiates one compound to another.
- **Fluorescence** imaging modality primarily tackles the electronic structure and the **electron configuration** of the sample. Different emission radiation, as a function of excitation frequency, can be detected and measured.
- **Reflection** imaging modality can tackle the molecular structure of the sample as a function of frequency while also providing a useful macroscopic **morphological representation.**

A complementary imaging modality that provides information about the **crystalline structure** of the material is the **Polarization**. Through it, birefringence parameters of materials can be measured.

The work of this thesis is to develop a **real-time** retardance/birefringence **mapping** module for a high throughput screening microscope in order to broaden the Multi Modal Feature Space by introducing, yet another, dimension.

Acknowledgements

I want to especially thank my Supervisor Costas Balas, for providing clear guidance and supervision in every difficult decision of this thesis, exposing me to Research and Development and forming me into an Electrical Engineer. I also want to thank my co-supervisors Aggelos Bletsas, for showing me the properties of the engineering mentality through his lectures and mind-puzzling projects and Dimitris Angelakis for teaching me the classical and quantum mechanic physics of all common phenomena that enable me to have a deep understanding of my profession. Once again, thank you, for helpful thoughts, discussion and for reading my research report, providing useful feedback.

Moreover, there was huge contribution to my work from the researchers of Electronics Laboratory in Technical University of Crete. I want to thank Thanasis Tsapras, for his incessantly positiveness and patience in explaining me the complex optical setups. Christos Housos, for enabling me in my research, providing helpful thoughts and ideas and helping me understanding firmware development. Makis Stefatos for the continuous conversations on optimization problems while designing the software of the system. Babis Boras for all his useful advises in complex software engineering problems. Christos Rossos for his willing of helping, advising and explaining hardware circuitry. Last but not least, I want to thank to Panagiotis Tsopelas, Panagiotis Takas, Nikos Kaminakis and Nathanail Kortsalioudakis for providing useful help and ideas for the research and development.

Additionally, I want to specially thank my fellow friends Giorgos Protopapadakis, Michalis Nikiforakis, Anna Minadaki and Konstantina Mammou for their love and effort, contributing with ideas and discussions while constructing this report. I also want to thank Yiannis, Chrisostomos, Odysseas, Alex and every other friend that formed my mentality as is. Last but not least I am extremely grateful for my family and the love, happiness and courage they give me each and every day.

This research became possible with all these people and I am thankful for having them in my life.

Chapter 2

Background

2.1 Introduction

The thesis *"A novel multi modal high throughput screening and material identification imaging system"* is about the development of a real-time polarization microscopy module that can yield retardance measurements and birefringence map in video rate. The proposed solution is described in full detail. Before diving into the system design and implementation of the module it is essential to understand some basics.

The goal of this chapter is a) to state the different imaging modalities that can be used for real-time, non destructive analysis in microscopy and b) to introduce the theoretical background for the physics of polarized light as well as the means of measuring birefringence. All theoretical background will be discussed and the chapter's contents are organized in three sections, as follows:

- **Microscopy Technologies**
  The first section is about understanding the basics of microscopy with examples of imaging modalities that will act complementary to our polarization module. Wide-field transmission and fluorescence imaging modalities in microscopy apparatus are presented.

- **Polarized Light**
  The second section is about understanding the physics of polarization in a transverse wave and more specifically, electromagnetic (EM) radiation. A mathematical model describing such phenomena is introduced and based on this model, some useful tools and parameters to express the polarization state of a wave based on measurable quantities.

- **Birefringence**
  The third section is about the means that light interacts with matter in such a way that a double refraction index is observed. How the chemistry of birefringence materials works and how we can forge them into optical elements useful for polarization light microscopy.

- **Retardance/Birefringence Measurements**
  The final and forth section describes the state-of-art regarding polarization microscopy techniques and evaluates them in order to conclude to a design that is not yet available nor in industry or in academic equipment and aims in the real-time aspect of the measurement.

2.2 Microscopy Technologies

Microscopy, as an observation technological sector, uses light and optics to enhance the observer's capabilities of understanding the sample's structure. As a phenomenon, light is complex and it is classically described with a simple model based on rays and wavefronts, which belongs to a larger family of wave-like phenomena, the electromagnetic radiation. The visible light (400 to 700 nanometers) to which the human eye responds, is a very small fraction of the entire electromagnetic radiation spectrum. The remainder of the electromagnetic spectrum is invisible to humans.

Microscopy, in its early days, relied on oil lamps and natural sunlight to provide an external source of illumination for primitive (but often remarkably accurate) microscopes. Unfortunately, these methods did not provide reliable illumination and frequently the area of field illumination greatly exceeded the numerical aperture of the objective, causing glare and flooding.

Evolution of the light sources and optics used for specimen observation, enhanced the imaging quality and thus accuracy of assessment. Modern microscopy have developed a wide spectrum of useful modalities for life science research. These modalities are designed to aid in contrast enhancement and provide better observation and photomicrography of specimens. Having the means of producing multiple modality data, are almost guaranteed to have a hyperplane that can differentiate one sample from another in a deterministic manner. This is due to the contrast enhancement, which we will focus in this thesis later on.

2.2.1 Widefield Microscopy

Widefield microscopy, is fundamentally any technique in which the entire specimen of interest is exposed to the light source with the resulting image being viewed either by the observer or a camera. In this section, microscope configurations for WF imaging will be discussed looking at light paths involved, the problems of out-of-focus light, as well as some of the more advanced WF techniques, such as WF Super-Resolution.

Brightfield Microscopy The most basic form of Widefield microscopy is "brightfield microscopy" in which the entire specimen is illuminated by white light either from above (in an inverted configuration), or below (in a standard upright microscope). This configuration has influence on the specimen which can be investigated. Upright microscopes are commonly used for applications with fixed samples, mounted on glass slides. Inverted microscopes have been invented to watch living cells. They are commonly grown in liquid solutions. Only a configuration with the objective below and the condenser above the specimen guarantees a close enough proximity of the objective to the specimen.

Construction of a microscope using the brightfield microscopy technique, is based on these four components:

- **Light Source:** Trans-illumination below sample that propagates through to condenser and objective lens. Typically a broadband source such as a quartz halogen bulb or LEDs is used.
- **Condenser Lens:** Collects trans-illuminated light and focuses to sample.
- **Objective Lens:** Collects light which propagates through sample and enhances details by a factor of magnification.
- **Eyepiece/Camera:** Views or records the image.

There are some limitations to the brightfield microscopy technique, which include very low contrast or blurriness (out-of-focus material) for cellular or biological samples and low optical resolution due to limitations of light. Finally, samples that are naturally colorless and transparent cannot be seen well and often have to be stained before viewing.

Enhancing the resolution of a Brightfield microscope is accomplished by various simple methods. By reducing or increasing the amount of the light source by the iris diaphragm. Use of a colored (usually blue) or polarizing filter on the light source to highlight features not visible under white light. Use of an oil-immersion objective lens and a special immersion oil placed on a glass cover over the specimen. However, simplicity of the brightfield technique is a huge benefit when first imaging an unknown sample. Additional optical microscopy applications include darkfield illumination, phase contrast, fluorescence, and differential interference contrast.

A typical brightfield illumination image has a dark sample with a white background, the darker the regions on a sample, the more absorption of light that has occurred, as shown in Figure 2.1 (a).

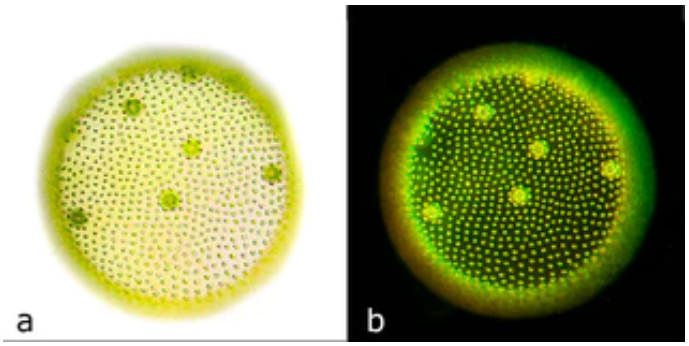

Figure 2.1: Volvox aureus - a fresh water algae. Acquired using Bright Field (a) and Dark Field (b) illumination.

Source: moticmicroscopes.com

Dark-field Microscopy In optical microscopy, dark-field describes a microscopy technique used to enhance the contrast in unstained samples. Dark-field microscopy describes microscopy methods, which exclude the unscattered light beam from the image. As a result, the field around the specimen (background) is generally dark.

Dark-field microscopy is a very simple yet effective technique and well suited for uses involving live and unstained biological samples. Considering the simplicity of the setup, as shown in Figure 2.2, the quality of images obtained from this technique is impressive. Construction of a microscope using the dark-field modality, is based on these four components:

- **Light Source:** Enters the microscope and hits the dark field patch stop, which is a disc used to block light from entering the condenser and leaves a circular ring of illumination. Typically a broadband source such as a quartz halogen bulb or LEDs is used.
- **Condenser Lens:** Collects outer ring of illumination and focuses it on the sample.
- **Objective Lens:** Light hits the sample, and is transmitted or scattered from it. Scattered light enters the objective lens, whereas transmitted light is not collected by the lens. The direct illumination block assists in this step.
- **Eyepiece/Camera:** Views or records the image.

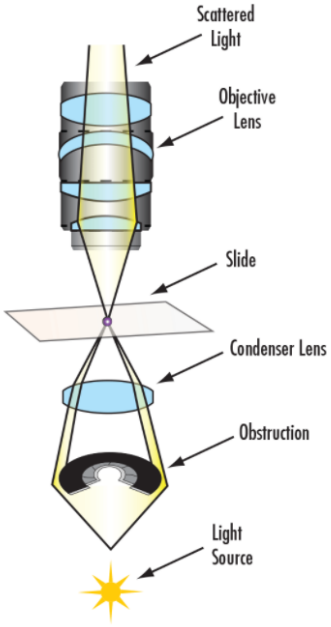

Figure 2.2: Darkfield Microscopy Setup.
Source: edmundoptics.com

Dark-field microscopy has its own limitations. The low light levels seen in the final image, demands that the sample must be very strongly illuminated, which can cause damage. The interpretation of dark-field images must be done with great care, as common dark features of bright-field microscopy images may be invisible, and vice versa. In general the dark-field image lacks the low spatial frequencies associated with the bright-field image, making the image a high-passed version of the underlying structure.

A typical darkfield illumination image has a white/bright specimen with a dark background and environment filling the image. This is the exact opposite of a brightfield illumination image, and is useful for unstained specimens or images that require increased contrast. The advantage with using darkfield illumination is that unstained specimens can remain alive and vital, whereas their brightfield counterparts must be treated and are no longer active. Also, it is possible to acquire more qualitative results with this technique through live cellular analysis, as shown in Figure 2.1 (b).

While the dark-field image may first appear to be a negative of the bright-field image, different effects are visible in each. In bright-field microscopy, features are visible where either a shadow is cast on the surface by the incident light or a part of the surface is less reflective, possibly by the presence of pits or scratches. Raised features that are too smooth to cast shadows will not appear in bright-field images, but the light that reflects off the sides of the feature will be visible in the dark-field images.

2.2.2 Fluorescence Microscopy

By the late 1800s, microscope design was largely figured out, but cells are mostly water, and therefore mostly transparent. An imaging modality that could generate higher **contrast** images was in need. Atomic, molecular, and optical (AMO) science and engineering stands at the confluence of strong scientific and technological currents in physics, chemistry, and electrical engineering. Seeking ways to expand our ability to use light for many purposes: to observe and manipulate matter at the atomic scale, to use nanostructures to manipulate light at the subwavelength scale, to develop quantum devices, and to control internal molecular motion and modify chemical reactivity with light. Fluorescence is a process in which matter absorbs light and re-emits at a different wavelength, thus yielding higher contrast images compared to widefield microscopy.

Light–matter interaction When absorbing a photon, an electron in a molecule becomes "excited" into a higher energy level (states S_n in Figure 2.3. This higher level is unstable, so eventually the electron will relax down to its ground state and can release that energy as a photon in a process called **fluorescence**. While the electron is in the excited state, a very small (generally nanosecond-scale) amount of time passes and a small amount of energy can dissipate in vibrational relaxation. This causes the energy of the emitted photon to be somewhat less than the originally absorbed energy. This results in the emitted photon having a longer wavelength than the absorbed photon. Additionally, the lag between the excitation and emission events is the fluorescence lifetime, which has the temporal profile of exponential decay. Fluorophores have unique absorption and emission spectra and fluorescence lifetimes that are generally dependent on their chemistry, but can also be altered by their environment.

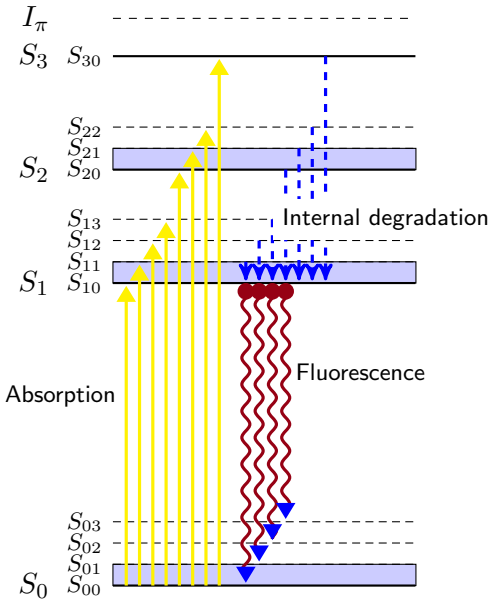

Figure 2.3: The electronic states of a molecule and the transitions between them to produce fluorescent light. (Phosphorescence is omitted)

The basic function of a fluorescence microscope is to irradiate the specimen with a desired and specific band of wavelengths, and then to separate the much weaker emitted fluorescence from the excitation light. In a properly configured microscope, only the emission light should reach the eye or detector so that the resulting fluorescent structures are superimposed with high contrast against a very dark (or black) background. The limits of detection are generally governed by the darkness of the background, and the excitation light is typically several hundred thousand to a million times brighter than the emitted fluorescence.

Vibrational energy is lost when electrons relax from the excited state back to the ground state. As a result of the energy loss, the emission spectrum of an excited fluorophore is usually shifted to longer wavelengths when compared to the absorption or excitation spectrum (note that wavelength varies inversely to radiation energy). This well-documented phenomenon is known as Stokes' Law or **Stokes' shift**. As Stokes' shift values increase, it becomes easier to separate excitation from emission light through the use of fluorescence filter combinations. This feature gives a unique signature of the specimen's **electronic structure**.

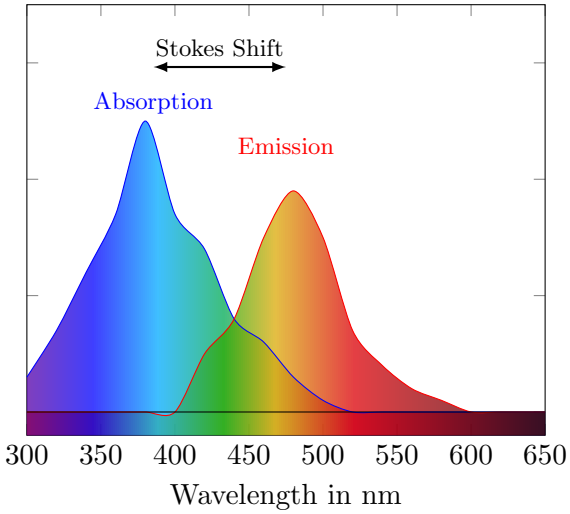

Figure 2.4: Stokes shift: the difference between positions of the band maxima of the absorption and emission spectra of the same electronic transition. $\sim 100nm$ Stokes shift

The effective separation and detection of excitation and emission wavelengths is achieved in fluorescence microscopy through the proper selection of filters to block or pass specific wavelength bands in the ultraviolet (UV), visible (VIS), and near-infrared (NIR) spectral regions. The most important criteria, in view of relatively low fluorescence emission intensities (see discussion above), is that the light source utilized for excitation be of sufficient brightness so that the weak emission light can be maximized, and that the fluorochromes possess adequate absorption properties and emission quantum yields. For that reason, laser light sources, that provide a high optical power, are preferred.

As shown in Figure 2.4, exiting a matterial with high energy light (small wavelength), then an emitted light of lower energy (higher wavelength) may be observed. There are three major categories of filters: excitation, barrier, and dichromatic beamsplitters (or dichroic mirrors). Fluorescence filters were formerly almost exclusively constructed from dyed glass or gelatin sandwiched between two glass plates. However, the current trend is to manufacture high-resolution filters with interference optics for excitation filters to pass or reject wavelengths of light with a great specificity and high transmission. Dichromatic beamsplitters are specialized interference filters designed to reflect or pass light of specific wavelengths when placed into the light path at a 45-degree angle (see Figure 2.5).

Fluorescence microscope schematic Construction of a microscope using the fluorescence modality, is based on these four components:

- **Light Source:** Enters the microscope and hits the excitation filter, which is a bandpass filter used to match the wavelengths that the dichroic mirror reflects. Typically a high optical energy light source is used, such as *Arc-Discharge Fluorescence Lamps*. If a monochromatic laser source is used, then the excitation filter can be ommited.
- **dichroic mirror:** Reflects the excitation wavelengths while allows other (emmited) wavelengths to transmit through it.
- **Objective Lens:** Light hits the sample, and is emitted from it. Emitted light enters the objective lens and is properly allinged to hit the dichroic mirror at a 45° angle.
- **Camera:** Views or records the image.

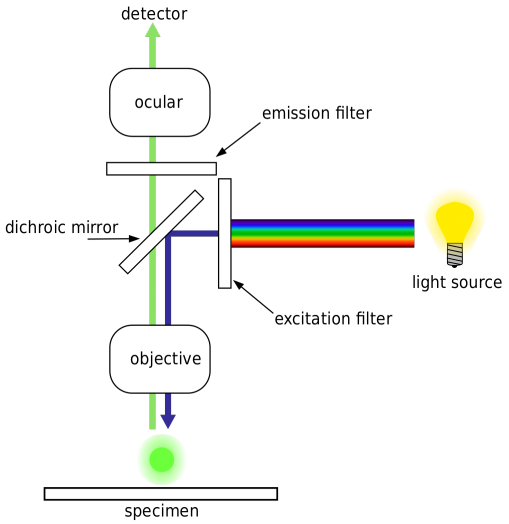

Figure 2.5: Schematic of a fluorescence microscope.
Source: wikimedia.org

2.3 Polarized Light

Light or visible light is electromagnetic radiation within the portion of the electromagnetic spectrum that is perceived by the human eye. Light wave is a transverse wave that has both an electric and a magnetic component. Regular (unpolarized) light waves are the ones that the electric field vectors vibrate in all planes that are perpendicular with respect to the direction of propagation and are random in space and time. If the electric components are restricted to a single plane, then the light wave is referred to as **linearly polarized** with respect to the direction of propagation.

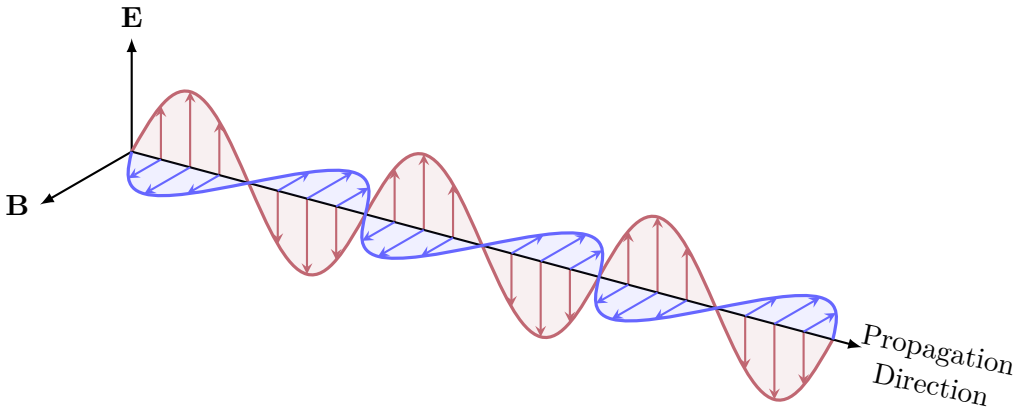

Figure 2.6: A linearly polarized electromagnetic wave with E denoting the electric field plane and B denoting the perpendicular magnetic field.

By the plane wave approximation we can define the electric components as $\vec{E}(r,t)$ as a traveling plane wave, where r denotes the distance from the center of oscillation and t the time. The wave $\vec{E}$ is the **light polarization vector** and is uniform on the plane k such that: $k \perp \vec{E}$. Figure 2.6

The polarization of light can either be **linear**, **circular**, or **elliptical**.

2.3.1 Linear polarization

An unpolarized light beam can easily be linearly polarized by the use of a filter called polarizer. Those filters contain long-chain polymer molecules that are oriented in a single direction. Only the incident light that is vibrating in the same plane as the oriented polymer molecules is absorbed, whereas the light that vibrates vertically to this plane is passed through.

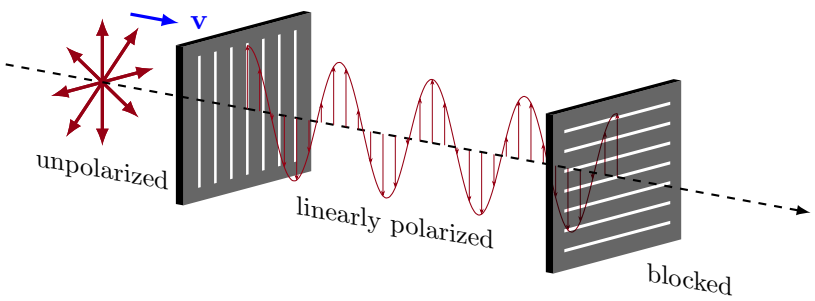

Figure 2.7: Polarization of light in a crossed polarization arrangement.

When the unpolarized beam propagates towards the vertical polarizer of Figure 2.7, all electric field vectors vibrate perpendicular to the direction of propagation with an equal

distribution in all planes (only 8 are visualized). By encountering the first polarized, only the electric vector that lives on the vertical plane is allowed through. Resulting in a vertically polarized light beam. When the latter encounters the horizontal polarizer, then the light is absorbed by the filter and no light beam propagates further. The concept of using two polarizers oriented at right angles with respect to each other is commonly termed crossed polarization and is fundamental to the concept of polarized light microscopy.

2.3.2 Elliptical and Circular polarization

Light that is circularly polarized is the electromagnetic wave in which the electric field vector transcribes the shape of a circle in all planes perpendicular to the direction of propagation. That can be achived with two different linearly polarized light beams that are oriented at right angles with respect to each other, have a phase shift of $\Delta\phi = n \cdot \frac{\pi}{2}$ and carry the same energy (same amplitude).

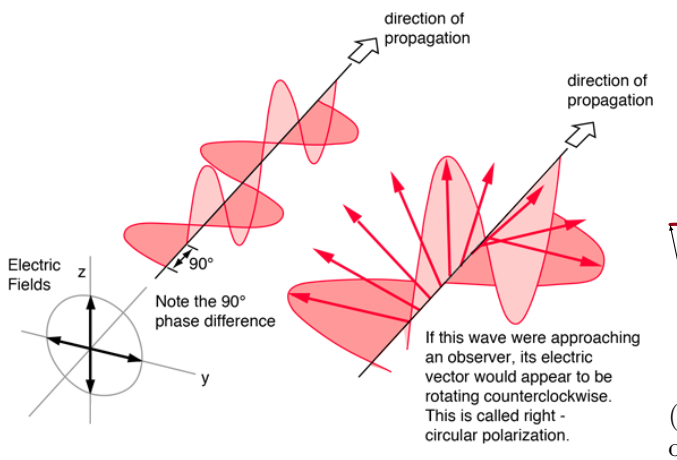

Source: hyperphysics.phy-astr.gsu.edu

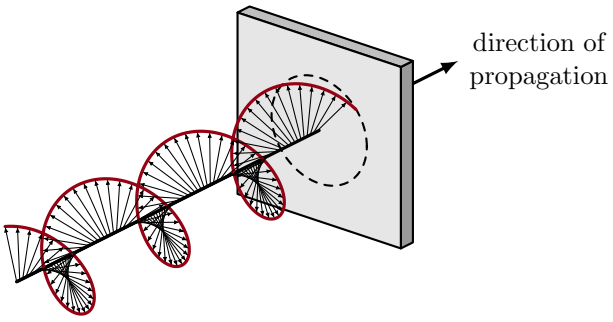

(a) Profile of circularly polarized light on the plane perpendicular to the direction of propagation.

Figure 2.8: Circularly polarized light.

When either the phase shift $\Delta\phi$ or the amplitude of one wave or both change, then the light is described as elliptically polarized. Elliptical polarization, which is a general state of circular polarization, has a rotational "sense" that refers to the direction of electric vector rotation around the propagation axis of the light beam. When viewed end-on, the direction of polarization can be either left-handed or right-handed. Clockwise rotational sweeps of the vector are referred to as right-handed polarization, and counterclockwise rotational sweeps represent left-handed polarization.

From now on, we will refer to left (counterclockwise) circular polarization as **LCP** and to right (clockwise) circular polarization as **RCP**.

As shown in Figure 2.10, the polarization ellipse is highly dependent on the ratio of $\frac{E_y}{E_x}$ and the phase difference between the two components E_y and E_x. Under certain conditions the ellipse may collapse into a straight line, in which case the polarization is called linear. In the other extreme, when the two components are of equal magnitude and 90° out of phase, the ellipse will become circular. Thus linear and circular polarization are the two special cases of elliptical polarization. Linear polarization may be further classified as being vertical, horizontal, or slant.

It becomes clear that when modeling a total polarization state, one should refer to the general case of elliptical polarization. In the next section, a brief description of the formal mathematical model is depicted and considers cases of total, partial and no polarization state.

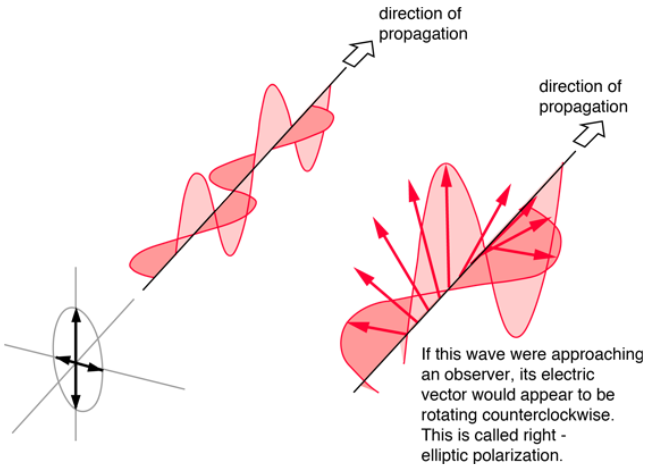

Source: hyperphysics.phy-astr.gsu.edu

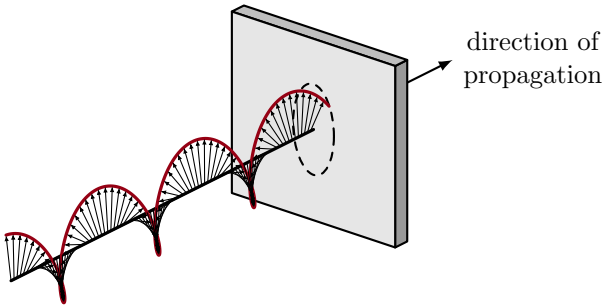

(a) Profile of elliptically polarized light on the plane perpendicular to the direction of propagation.

Figure 2.9: Elliptically polarized light.

2.3.3 Formal description of light polarization

Taking into account the RCP of the Figure 2.8, and recover that in order to have circular polarization the electric field vactors need to *have a phase shift of* $\Delta\phi = n \cdot \frac{\pi}{2}$ *and carry the same energy (same amplitude)* $E_x = E_y = E_0$,

we can yield that

$$\vec{E}_0 = \left(E_0, E_0 e^{i\frac{-\pi}{2}}, 0\right) = (E_0, -iE_0, 0) \tag{2.3.3.1}$$

Thus,

$$\vec{E} = (E_x, E_y, E_z) \propto \left(E_0 e^{i(kz-\omega t)}, -iE_0 e^{i(kz-\omega t)}, 0\right) \tag{2.3.3.2}$$

Taking the real part gives the actual electric field

$$Re\left[\vec{E}\right] = (E_0 cos(kz - \omega t), E_0 sin(kz - \omega t), 0) \tag{2.3.3.3}$$

For LCP, we would have $\phi_x - \phi_y = \frac{\pi}{2}$ and therefore

$$Re\left[\vec{E_{LCP}}\right] = (E_0 cos(kz - \omega t), -E_0 sin(kz - \omega t), 0)$$

We can mathematically define light as a spherical tensor. Therefore the spherical basis model is convenient to express it. In order to do so, a change of basis is required:

$$\vec{E} = \begin{pmatrix} e_x \\ e_y \\ e_z \end{pmatrix} = \mathbf{U}^{-1} \begin{pmatrix} e_+ \\ e_- \\ e_0 \end{pmatrix}, \qquad \mathbf{U}^{-1} = \begin{pmatrix} -\frac{1}{\sqrt{2}} & +\frac{1}{\sqrt{2}} & 0 \\ +\frac{i}{\sqrt{2}} & +\frac{i}{\sqrt{2}} & 0 \\ 0 & 0 & 1 \end{pmatrix} \tag{2.3.3.4}$$

With the transformation matrix $\mathbf{U}$ being a unitary matrix $\left(\mathbf{U}^\dagger = \mathbf{U}^{-1}\right)$

Combining Equation 2.3.3.2 and Equation 2.3.3.4 we can yield that a change of basis for the electric field component of light will be

$$\vec{E} = \begin{pmatrix} e_+ \\ e_- \\ e_0 \end{pmatrix} = \begin{pmatrix} -\frac{1}{\sqrt{2}}(e_x + ie_y) \\ +\frac{1}{\sqrt{2}}(e_x - ie_y) \\ e_z \end{pmatrix} \Longleftrightarrow \begin{cases} E_+ &= -\frac{1}{\sqrt{2}}(E_x + iE_y) \\ E_- &= +\frac{1}{\sqrt{2}}(E_x - iE_y) \\ E_0 &= E_z \end{cases} \tag{2.3.3.5}$$

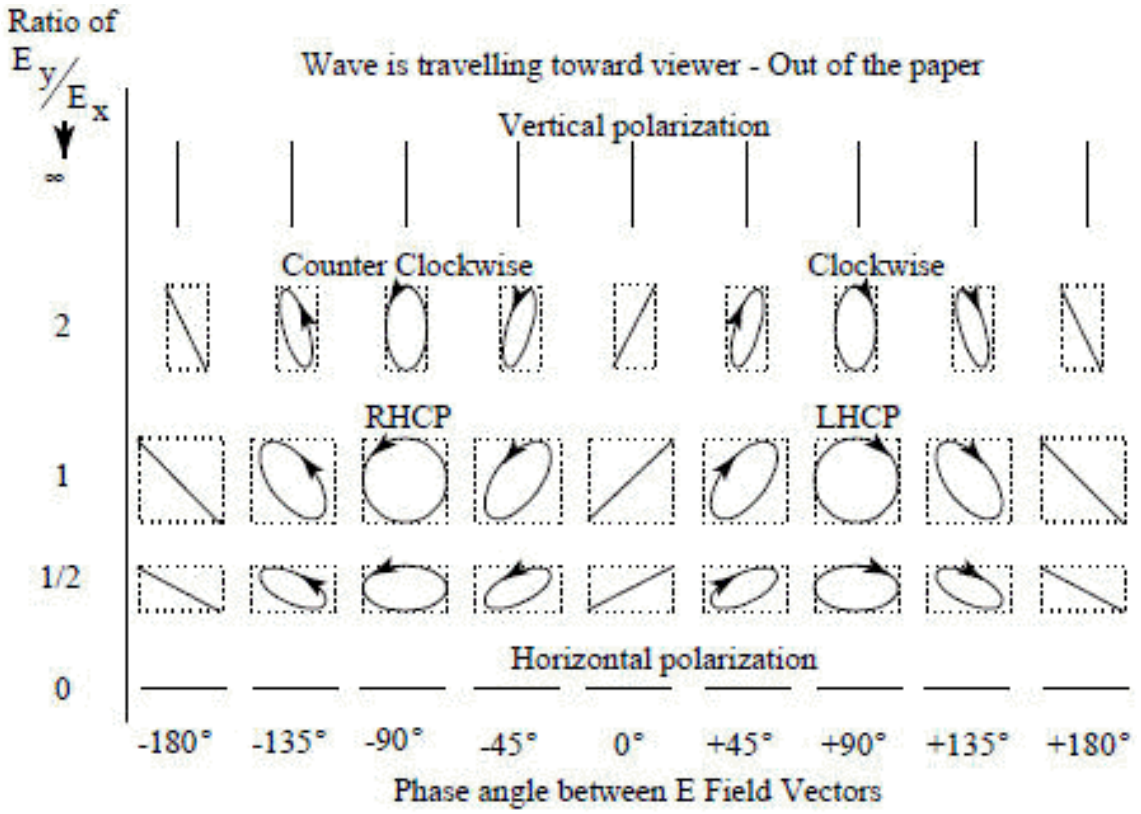

Figure 2.10: Polarization state as a Function of E_y/E_x and Phase angle. Depicts plots of the E field vector while varying the relative amplitude and phase angle of its component parts.

Source: [3]

By having the state of the propagating light's electric field components in the spherical bases, we can proceed analyzing with respect to its density matrix, a matrix that describes the quantum state of a physical system.

2.3.4 Polarization density matrix

The allowed states of light as described, are **RCP** $|\mathbf{R}\rangle$, **LCP** $|\mathbf{L}\rangle$, or **a superposition of both** $\alpha|\mathbf{R}\rangle + \beta|\mathbf{L}\rangle$, where $|\alpha|^2+|\beta|^2 = 1$ corresponding to linear, circular and elliptical polarization. Unpolarized light cannot be described as any state of the form $\alpha|\mathbf{R}\rangle + \beta|\mathbf{L}\rangle$. Unlike polarized light, it passes through a polarizer with 50% intensity loss whatever the orientation of the polarizer; and it cannot be made polarized by passing it through any wave plate. However, unpolarized light can be described as an statistical ensemble, e.g. as each photon having either $|\mathbf{R}\rangle$ polarization or $|\mathbf{L}\rangle$ polarization with probability 1/2.

For this example of unpolarized light, the density operator equals

$$\rho = \frac{1}{2}|\mathbf{R}\rangle\langle\mathbf{R}| + \frac{1}{2}|\mathbf{L}\rangle\langle\mathbf{L}| = \frac{1}{2}\begin{pmatrix}1 & 0\\ 0 & 1\end{pmatrix} \tag{2.3.4.1}$$

By taking into account the spherical basis we can yield

$$\rho^{light} = \frac{1}{3}|\mathbf{e}_+\rangle\langle\mathbf{e}_+| + \frac{1}{3}|\mathbf{e_0}\rangle\langle\mathbf{e_0}| + \frac{1}{3}|\mathbf{e}_-\rangle\langle\mathbf{e}_-| = \frac{1}{3}\begin{pmatrix}1 & 0 & 0\\ 0 & 1 & 0\\ 0 & 0 & 1\end{pmatrix} \tag{2.3.4.2}$$

Having,

$$\begin{array}{c|c|c|c} pure-\mathbf{LCP} & z-polarized & pure-\mathbf{RCP} & unpolarized \\ \rho_{left}^{light}=\begin{pmatrix}1&0&0\\0&0&0\\0&0&0\end{pmatrix} & \rho^{light}=\begin{pmatrix}0&0&0\\0&1&0\\0&0&0\end{pmatrix} & \rho_{right}^{light}=\begin{pmatrix}0&0&0\\0&0&0\\0&0&1\end{pmatrix} & \rho_{unpol}^{light}=\begin{pmatrix}\frac{1}{3}&0&0\\0&\frac{1}{3}&0\\0&0&\frac{1}{3}\end{pmatrix} \\ (\alpha) & (\beta) & (\gamma) & (\delta) \end{array} \tag{2.3.4.3}$$

Generally, for light propagating along the z axis it is true that

$$\rho^{light}=\begin{pmatrix}\rho_{+1+1}&0&\rho_{+1-1}\\0&0&0\\\rho_{-1+1}&0&\rho_{-1-1}\end{pmatrix} \tag{2.3.4.4}$$

With the diagonal elements indicating the light intensity with corresponding polarizations and the off-diagonal elements indicating the correlations between states. Note that the density matrix is **Hermitian** meaning that the matrix is equal to its conjugate transpose $\rho^{\dagger}=\rho$. Lastly, we can yield the energy of the electric field vector by computing the trace of the matrix:

$$Tr\rho=\sum_{q}E^{q}(E^{q})^{*}=|E|^{2} \tag{2.3.4.5}$$

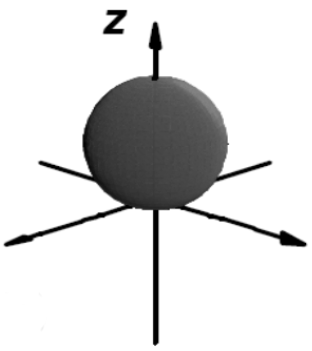

(a) LCP light sphere visualization as described in Equation 2.3.4.3 (α).

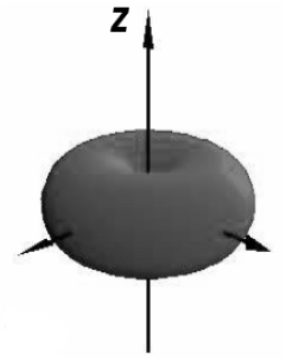

(b) Z polarized light visualization as described in Equation 2.3.4.3 (β).

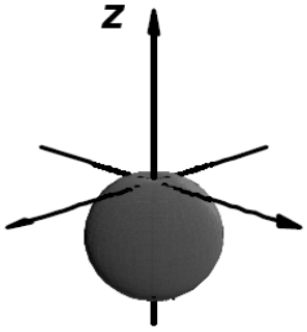

(c) RCP light sphere visualization as described in Equation 2.3.4.3 (γ).

Figure 2.11: Visual representation of the polarization spheres.
Source: berkeley.edu

2.3.5 Stokes parameters

In order to formally describe polarized light, one should know the exact parameters of the elliptical polarization, which includes circular and linear polarization as special cases. The parameters of elliptical polarized light are 1) the **eccentricity** of the polarization ellipse, 2) the **orientation** of the polarization ellipse, 3) the **chirality** (handedness or rotation direction) of the polarization ellipse, and 4) whether the polarization is **total or partial**, and, if partial, the degree of polarization. For the context of this chapter, we will assume that the polarization is total. Further more, and assuming the light is monochromatic, we need to know either the **frequency**, or the wavelength **and** the refractive index

of the medium in which it is travelling. Lastly, the **flux density** of the light in $\frac{W}{m^2}$ which is related to the electric field strength of the electromagnetic wave.

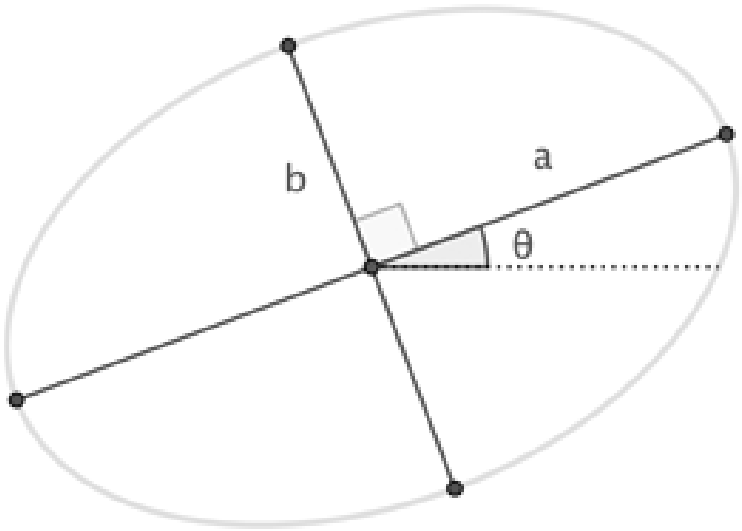

Figure 2.12: The polarization ellipse of light with α and β describing the E_{max} and E_{min} of the electric field component in volts per metre.
Source: math.stackexchange.com

We can compute the eccentricity of the ellipse by using the formula: $\boxed{e = \sqrt{1 - \frac{\beta^2}{\alpha^2}}}$.

The angle θ that the major axis makes with the horizontal describes the chirality, assuming that the observer is looking towards the source of the light.

In order to describe the flux density of the beam, one must know the impedance (in the sense used in electromagnetic theory) of the medium $Z = \sqrt{\frac{\mu}{\epsilon}}$, where ϵ is the permittivity of the medium in which the radiation is travelling and μ is the permeability of the medium and given by the formula $v = \frac{1}{\sqrt{\epsilon\mu}}$, v denoting the speed of the radiation is travelling through the medium.

For elliptical polarized light, the flux density is $F = \frac{\alpha^2+\beta^2}{4Z}$.

Even though the mathematical model seems complete, non of the above parameters are directly measurable. The observer can only measure the intensity of the light beam through different angles of polarizing filters.

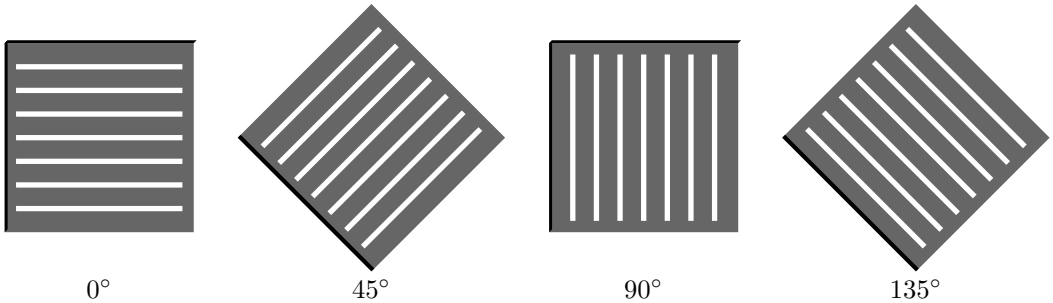

Figure 2.13: Polarization filters in four different angles.

In the Figure 2.13, the lines represent the electric field component allowed through the filter. We can measure the flux density (F) of the light after passage through the filter at each of these angles, and also without the filter, and somehow determine from these measurements the shape and orientation of the polarization ellipse.

The stokes parameters are a set of values that describe the polarization state of electromagnetic radiation and their classical notation is **IQUV**. Since they aim to describe the polarization state —which may be non existent— they should include the intensity of the light (regardless polarization), the intensity of linearly polarized is in two perpendicular planes, and the intensity of elliptical polarized light.

1. $\mathbf{I} = F$ where the flux density (F) is the total flux density of the unobstructed light
2. $\mathbf{Q} = F_{0^\circ} - F_{90^\circ}$ where the degree denotes the flux density of the beam after passing through the filters of Figure 2.13
3. $\mathbf{U} = F_{45^\circ} - F_{135^\circ}$ where the degree denotes the flux density of the beam after passing through the filters of Figure 2.13
4. $\mathbf{V} = 2F_C - \mathbf{I}$ where F_C is the flux density of clockwise circular polarized light

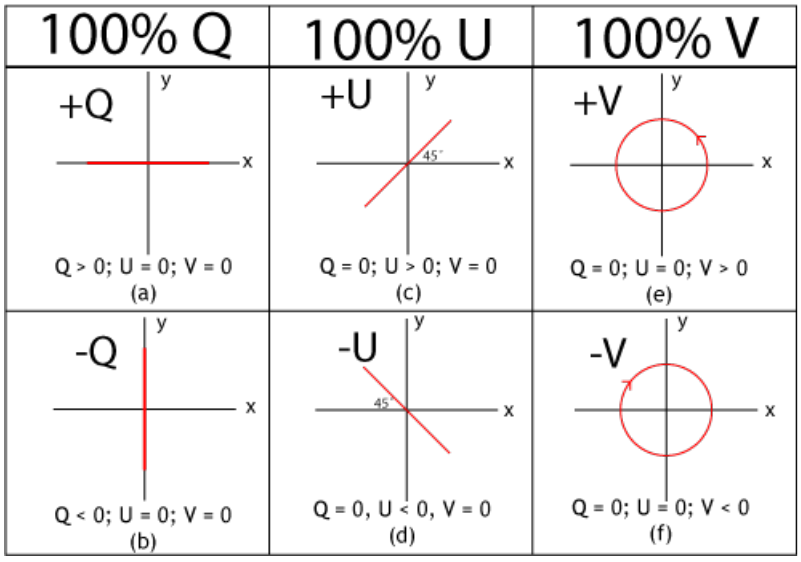

Figure 2.14: Examples of the Stokes parameters in degenerate states.
Source: wikimedia.org

The modern notation for the Stokes parameters is the Stokes vector $\tilde{\mathbf{S}}$ with its components S_0, S_1, S_2, S_3 such as:

$$\vec{S} = \begin{pmatrix} S_0 \\ S_1 \\ S_2 \\ S_3 \end{pmatrix} = \begin{pmatrix} \mathbf{I} \\ \mathbf{Q} \\ \mathbf{U} \\ \mathbf{V} \end{pmatrix} \tag{2.3.5.1}$$

Apart from the total intensity S_0, polarization proper is fully described by the normalized (reduced) three-dimensional (3D) Stokes vector:

$$\vec{s} = \left(S_1/S_0, \quad S_2/S_0, \quad S_3/S_0\right) = \left(s_1, \quad s_2, \quad s_3\right) \tag{2.3.5.2}$$

Q **U** *and* **V**, are all related to the eccentricity e and the inclination θ of the polarization ellipse in a manner that is out of scope for proofing in this context. Hereby I provide the relations without derivation.

$$\mathbf{Q} = \frac{e^2 \cos 2\theta}{2 - e^2} \tag{2.3.5.3}$$

$$\mathbf{U} = \frac{e^2 \sin 2\theta}{2 - e^2} \tag{2.3.5.4}$$

$$\mathbf{V}^2 = \frac{4\left(1 - e^2\right)}{\left(2 - e^2\right)^2} \tag{2.3.5.5}$$

We can therefore yield both the chirality (from the sign of V) and the eccentricity (but not θ) from V alone. The relation between $|V|$ and e is shown in Figure 2.15.

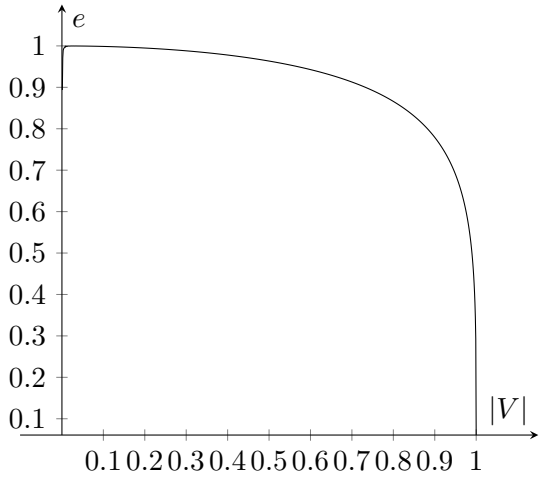

Figure 2.15: Relation between Stokes parameter $|V|$ and eccentricity e of the polarization ellipse.

From the equations 2.3.5.3, 2.3.5.4 and 2.3.5.5 we can derive that, for light that is totally polarized, the parameters Q,U and V are not independent and that:

$$\mathbf{I}^2 = \mathbf{Q}^2 + \mathbf{U}^2 + \mathbf{V}^2 \tag{2.3.5.6}$$

The equations above are valid only for the case of total elliptical polarization and the case of partial polarization proves to be important because most sources of polarized light are more likely to be partially polarized rather than totally polarized.

2.3.6 Partially polarized light and the Poincaré sphere

Natural light, like most other common sources of visible light, is incoherent: radiation is produced independently by a large number of atoms or molecules whose emissions are uncorrelated and generally of random polarizations. Unpolarized light can be described as a mixture of two independent oppositely polarized streams, each with half the intensity. Light is said to be partially polarized when there is more power in one of these streams than the other. At any particular wavelength, partially polarized light can be statistically described as the superposition of a completely unpolarized component and a completely polarized one.

Polarization parameters

An important parameter is the degree of polarization (DOP) and we can derive it through Equation 2.3.5.2,

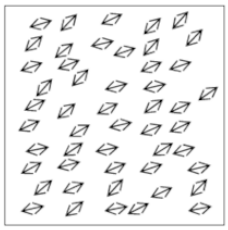

(a) Partially polarized light beam having incoherent polarization components.

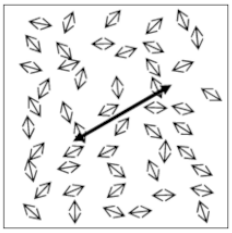

(b) Partially polarized light beam resulting in **plane** polarization. Vertical and horizontal polarization components are **in phase**.

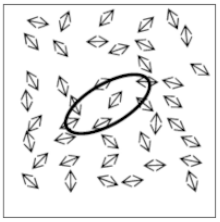

(c) Partially polarized light beam resulting in **elliptical** polarization. Vertical and horizontal polarization components are **out of phase**.

Figure 2.16: Partially polarized light beam, resulting in linear -plane- polarization 2.16b and in elliptical polarization 2.16c depending on the phase of polarization components. Source: phys.libretexts.org

$$DOP = \sqrt{\mathbf{Q}^2 + \mathbf{U}^2 + \mathbf{V}^2} \tag{2.3.6.1}$$

And the normalized (see Equation 2.3.5.2) form:

$$DOP_{norm} = |\vec{s}| = \sqrt{s_1^2 + s_2^2 + s_3^2} = \frac{\sqrt{S_1^2 + S_2^2 + S_3^2}}{S_0}, \qquad 0 \leq |\vec{s}| \leq 1 \tag{2.3.6.2}$$

From Equations 2.3.5.3, 2.3.5.4 and 2.3.6.1 we determine that

$$DOP = \sqrt{\mathbf{V}^2 + \frac{e^4}{(2 - e^2)^2}} \tag{2.3.6.3}$$

Thus from the measurements of $F_0, F_{90}, F_{45}, F_{135}$ and their combinations **IQUV** we have determined, for partially polarized light, the degree of polarization, and the eccentricity, orientation and chirality of the polarization ellipse.

Two rather useful parameters that will be crucial for our application are the degree of linear polarization ($DOLP$) and the degree of circular polarization ($DOCP$) that indicate how much linearly or circularly polarized the light is.

$$DOLP = \frac{\sqrt{S_1^2 + S_2^2}}{S_0} \tag{2.3.6.4}$$

$$DOCP = \frac{S_3}{S_0} \tag{2.3.6.5}$$

The Stokes vector for a partially polarized beam ($DOP_{norm} < 1$) can be considered as a superposition of a completely polarized Stokes vector S_P and an unpolarized Stokes vector S_U which are uniquely related to S as follows

$$\begin{aligned} S = S_P + S_U = \\ = S_0 p \begin{pmatrix} 1 \\ S_1/(S_0 p) \\ S_2/(S_0 p) \\ S_3/(S_0 p) \end{pmatrix} + (1-p) S_0 \begin{pmatrix} 1 \\ 0 \\ 0 \\ 0 \end{pmatrix} \end{aligned} \tag{2.3.6.6}$$

where $p = DOP_{norm}$.

Poincaré sphere

Equation 2.3.6.1 suggests that that the state of polarization of light can be described by a point in **QUV** space. This concept is described by the Poincaré sphere:

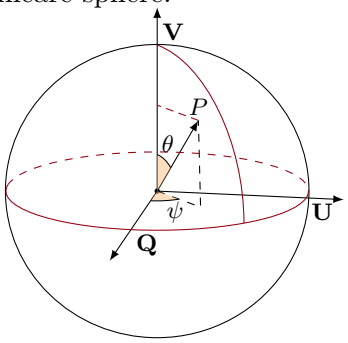

Figure 2.17: The Poincaré sphere.

In the **QUV** space, the Poincaré sphere is the unit sphere, $p = |\vec{s}| = 1$, and represents all states of total or complete polarization. Its center at the origin, $p = |\vec{s}| = 0$, represents unpolarized or randomly polarized light, and its interior, $0 < p = |\vec{s}| < 1$, represents all states of partial elliptical polarization. Inside the sphere, excluding the origin, the equatorial plane ($\mathbf{V} = 0$) represents partial linear polarization states, and the **V** polar axis represents partial circular polarization states.

Note that the angle θ of Figure 2.17 differs from the one of Figure 2.12.

2.4 Birefringence

2.4.1 Theory

A number of materials in nature are isotropic, meaning that they have a molecularly ordered crystal lattice structure that has the same optical properties (e.g. refraction index) at any orientation. However, the majority of materials do not have such a well-ordered structure and are called anisotropic. As a result, these materials exhibit double refraction of light that is also known as *birefringence*.

Anisotropic crystals, such as quartz, calcite, and tourmaline, have crystallographically distinct axes and interact with light by a mechanism that is dependent upon the orientation of the crystalline lattice with respect to the incident light angle. When light enters the optical axis of anisotropic crystals, it behaves in a manner similar to the interaction with isotropic crystals, and passes through at a single velocity. However, when light enters a non-equivalent axis, it is refracted into two rays, each polarized with the vibration directions oriented at right angles (mutually perpendicular) to one another and traveling at different velocities. This phenomenon is termed double refraction or birefringence and is exhibited to a greater or lesser degree in all anisotropic crystals.

To describe the birefringent properties of a crystal, we first need to define the optical axis. The optical axis, also known as the long axis - or fast axis - in birefringent crystals, is the direction upon which the incident light experiences only one refraction index, thus the birefringent material behaves as isotropic. If the incident light enters the material with an angle with respect to the optical axis it is refracted in two waves with perpendicular polarizations (see Figure 2.18):

1. ordinary ray (in short o-ray) traveling with the same velocity along the effective refractive index $n_\circ$ regardless of the direction in the crystal

2. extraordinary ray (in short e-ray) traveling with a velocity related to an effective refractive index between $n_\circ$ and n_e and is dependent upon the propagation direction within the crystal

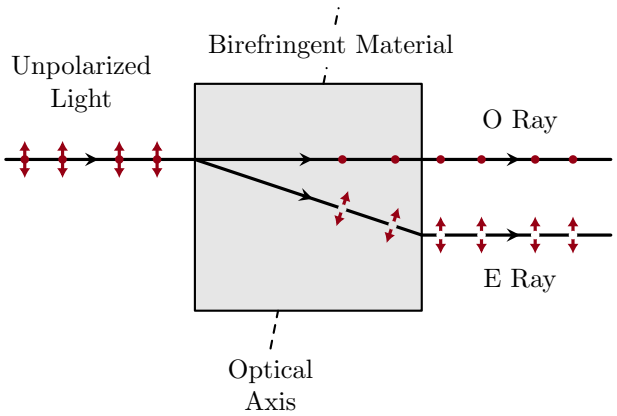

Figure 2.18: Visualization of double refraction due to birefringence in a crystal. The ordinary and extraordinary rays have perpendicular polarizations. Moreover, at an arbitrary angle between the optical axis and the incident light the two waves travel different paths in the crystal.

The birefringence Δn of a crystal is define as the difference $n_e - n_o$ between the ordinary and extraordinary indexes. The polarization of the e-ray is always perpendicular to the polarization of the o-ray. The wave travelling along the path with highest refractive index is called the slow wave while the ray travelling along the path with the lowest

refractive index is called the fast wave. When $n_e > n_o$ then the material has a positive birefringence so the fast wave coincides with the ordinary wave while the slow coincides with the extraordinary wave. The opposite holds when $n_e < n_o$, then fast coincides with the extraordinary wave and slow with the ordinary wave.

2.4.2 Polarized Light Microscopy

Polarized light microscopy is an ideal tool for observing phase transitions in optically transparent anisotropic crystals. Isotropic materials, such as unstressed glasses and cubic crystals, demonstrate the same optical properties in all directions. They have only one refractive index, and therefore, no restriction on the vibration direction of light passing through them. Anisotropic materials, in contrast, have optical properties that vary with the orientation of incident light with respect to the crystallographic axes. They demonstrate a range of refractive indices depending both on the propagation direction of light through a substance and on the vibrational plane coordinates.

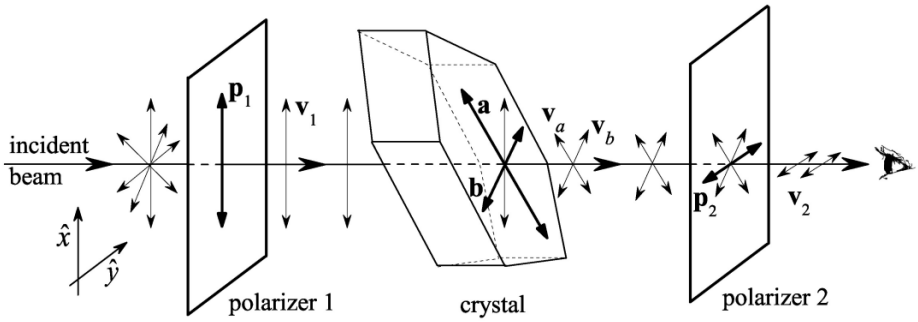

Figure 2.19: Diagram of an anisotropic crystal beam-splitting light between crossed-polarizers.

Source: [33]

By placing an anisotropic crystal with unique crystal axes, whose directions are represented by vectors a and b,

$$\vec{a} = a_x\hat{x} + a_y\hat{y}, \qquad \vec{b} = b_x\hat{x} + b_y\hat{y} \tag{2.4.2.1}$$

between two crossed-polarizers, where the polarizing direction of the first polarizer $\mathbf{p_1}$ is parallel to the x-axis ($\mathbf{p_1} \parallel \hat{x}$), and orthogonal to the second polarizer $\mathbf{p_2}$, which is then parallel to the y-axis ($\mathbf{p_1} \perp \mathbf{p_2} \parallel \hat{y}$) and then rotating the crystal, the optical axes of the crystal can be identified. To achieve this, we begin by describing how an anisotropic crystal behaves between cross-polarizers. First of all, when the incident beam, travels though the first polarizer, all vibrational directions, except those parallel to the x-axis are filtered out, Figure 2.19. The remaining "polarized" light beam then enters the crystal, which acts as beam splitter and divides light ray into two parts, such that the polarized light vector, $\vec{v_1}$, can be written as a linear combination of the crystal vectors a and b,

$$\vec{v_1} = a_1\,\vec{a} + b_1\,\vec{b} \tag{2.4.2.2}$$

to give two new light ray vectors $\vec{v_a}$ and $\vec{v_b}$,

$$\begin{aligned} \vec{v_a} &= a_1(a_x\hat{x} + a_y\hat{y}), \\ \vec{v_b} &= b_1(b_x\hat{x} + b_y\hat{y}). \end{aligned} \tag{2.4.2.3}$$

After the light has passed through the crystal, it enters the second polarizer, which filters out all light, but that which is along the y-axis, such that

$$\begin{aligned} \mathbf{p_1} \cdot \vec{v_a} &= a_1 a_y \hat{y} \\ \mathbf{p_2} \cdot \vec{v_b} &= b_1 b_y \hat{y}, \end{aligned} \tag{2.4.2.4}$$

and the final observable light ray $\vec{v_2}$ is

$$\vec{v_2} = (a_1 a_y + b_1 b_y)\hat{y} \tag{2.4.2.5}$$

2.4.3 Phase difference and direction of the o-ray and e-ray

The visualization of the wavefronts of the o-ray and e-ray in the case of negative and positive birefringence is shown in Figure 4. In both cases, the optical axis is drawn vertically and a point source is assumed to be located at a point along this axis. The ordinary wavefront will be spherical around the point source since it will have the same velocity in any direction. The extraordinary wavefront will have the same magnitude along the optical axis by definition but will encounter variations on the refractive index for different directions. As a result, the extraordinary wavefront will form an ellipse. As the angle between the extraordinary ray and the optical axis increases, the two waves have **different velocities**. This results in a relative phase difference between the ordinary and extraordinary waves.

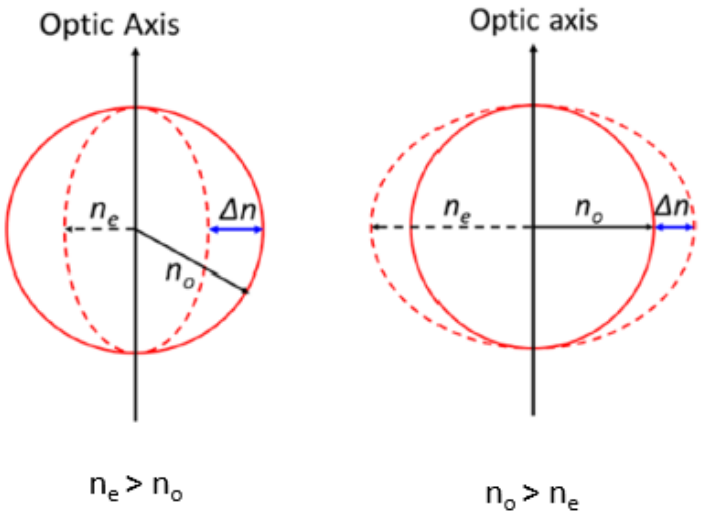

Figure 2.20: Representation of the ordinary (full circle) and extraordinary (dashed ellipse) wavefronts in case of a crystal with positive (left) and negative (right) birefringence. The birefringence, Δn, is indicated in both cases.
Source: [2]

Based on the wavefront representation of Figure 2.20, we can identify three possibilities regarding the direction of the o-ray and e-ray. When the incident polarized light is in a direction parallel to the optical axis of a birefringent material as shown in Figure 2.21(c), the light will experience only one diffraction index so the crystal behaves like an isotropic crystal.

If the incident polarized light is perpendicular to the optical axis as in Figure 2.21(b), the o-ray and e-ray will travel along the same direction but have a relative phase difference when exiting the crystal. As we shall see in the following sections, this orientation is used in the design of retarders. Finally, if the incident light is at an arbitrary angle with respect

to the optical axis as for example in Figure 2.21(a), then the o-ray and e-ray will diverge and exit the crystal at different points and angles.

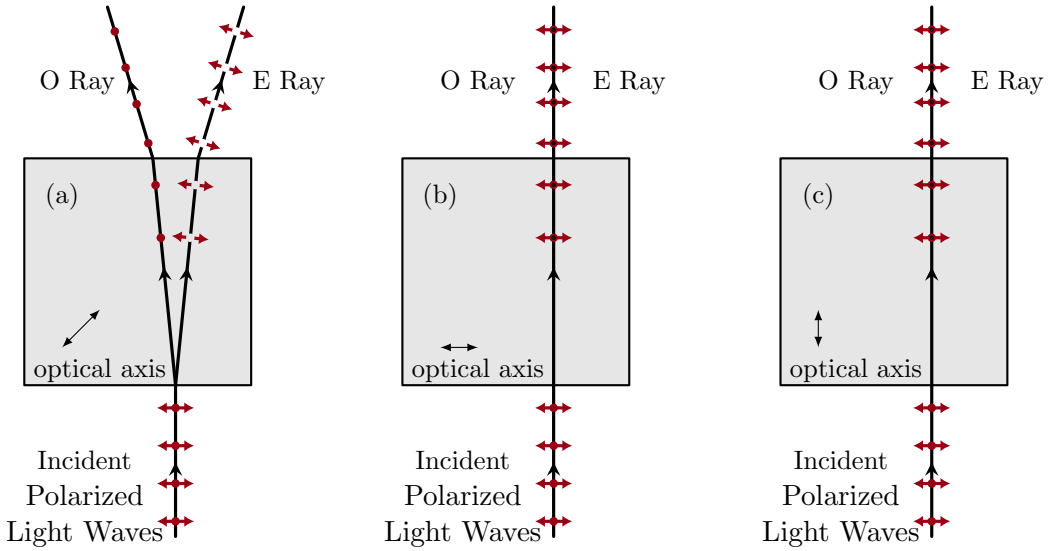

Figure 2.21: Behavior of a birefringent crystal with the optical axis at various angles with respect to an incoming polarized beam. The e-ray and o-ray are further apart at the 45° angle as shown interactively in [4].

As discussed in this section the orientation of the optical axis with respect to the incident light is of paramount importance as it determines whether the o-ray and e-ray have a phase difference but also defines the direction of the two rays exiting the crystal.

2.4.4 Retardance

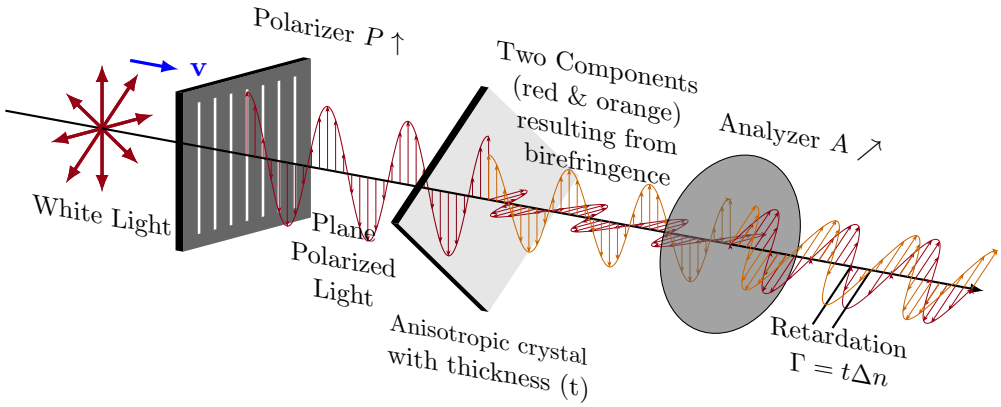

Figure 2.22: Visualization of two perpendicularly polarized waves with a phase difference interfering.

Since the ordinary and extraordinary waves have different velocities, this will result in an optical path difference between them. This optical path difference, also known as retardation Γ and expressed in units of length, is equal to:

$$\Gamma = t\Delta n \tag{2.4.4.1}$$

where t the thickness of the crystal and Δn the crystal's birefringence. This optical path difference introduces a phase difference between the two components that depends on the

wavelength λ of the incident light:

$$\delta = \frac{2\pi t \Delta n}{\lambda} \tag{2.4.4.2}$$

known as retardance (δ) which is expressed in radians. The retardation and its relation to retardance is illustrated in Figure 2.19. A light beam is linearly polarized from the Polarizer P and enters a birefringent object with thickness t. Two waves exit the object with a relative phase difference and perpendicular polarizations. After crossing a second polarizer, often called the Analyzer (A), the two polarized waves interfere and the polarization state parallel to the Analyzer's axis is projected. The retardation, which is the optical path difference of the two interfering waves, is related to the phase difference of the waves and is a function of the wavelength.

2.4.5 Retarders/Waveplates

As briefly described, to shift the phase of a polarized light wave we need to introduce a birefringent crystal along the path of the polarized light. This can be achieved by using specially designed optical elements made of birefringent crystals called waveplates or retarders. The design principle of retarders is based on cutting the birefringent crystal such that the optical axis is parallel to the plane of the surface as depicted in Figure 2.21(c). Then the two indexes of refraction, ordinary and extraordinary, have maximum and minimum values along two orthogonal axes, which are also named slow and fast [5]. The extraordinary axis is parallel to the optical axis and the ordinary axis is perpendicular to the optical axis. Thus, as depicted in Figure 2.23, in a retarder made of a crystal with positive birefringence the slow axis matches the extraordinary axis. The opposite holds for a crystal with negative birefringence (slow axis matches the ordinary and fast the extraordinary axis).

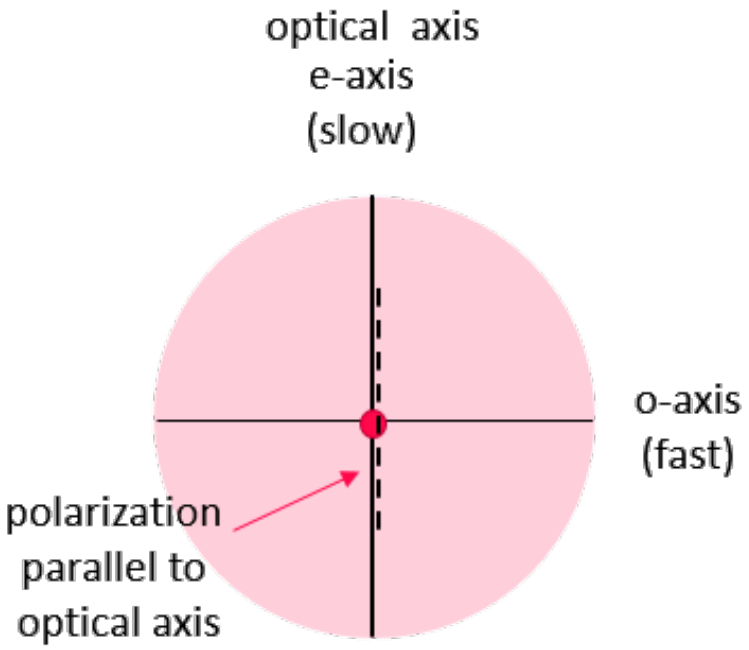

Figure 2.23: Drawing of the optical ordinary and extraordinary axis in a retarder with positive birefringence. In this case, the axis with the highest refractive index (slow) is parallel to the optical axis.

It is important to note again that the wave plate retards the velocity of only one component, the e-ray. This needs to be considered when calculating the phase difference

on the polarized state after the retarder. Also, in case unpolarized light is transmitted through a retarder, it will remain unpolarized when exiting. Thus, use of waveplates makes sense when using partially or totally polarized light [6].

Full Wave Plate

A Full Wave Plate (FWP) introduces a phase difference, or retardation, of 2π to an incoming polarized light of wavelength λ. As a result, the polarization state of the exiting light will remain the same.

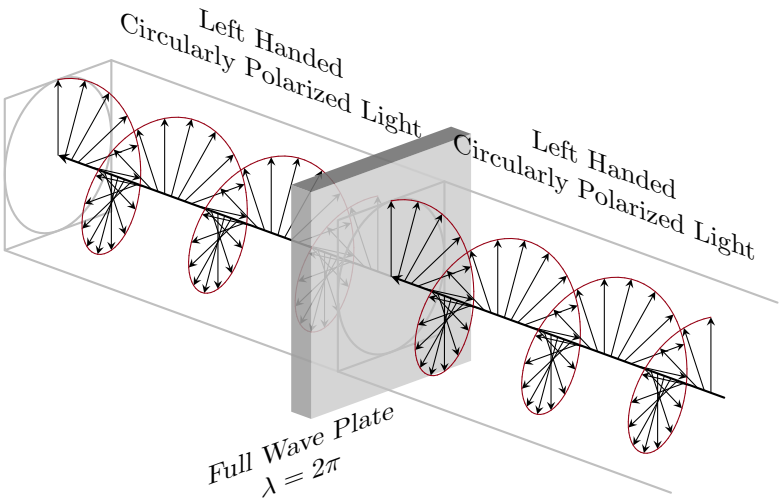

Figure 2.24: A circularly polarized wave traversing a Full Wave Plate. The perpendicularly polarization components exit with a phase difference of 2π. The combined wave due to interference will have the same polarization.

It is important to note that the FWP introduces a phase difference of 2π independently of the orientation of the slow axis of the retarder. Moreover, a FWP will introduce a 2π phase difference to one specific wavelength, i.e. the wavelength for which retardation $d\Delta n$ in (Eq. 2) is tuned as such that $\Delta = 2\pi$. This means that for a polychromatic source, all other wavelengths will experience a phase difference ϕ in the range of $0 < \phi < 2\pi$ and will be elliptically polarized when exiting the FWP. As we will explain in Section 3, FWPs are used in applications where the order of retardation and the sign of birefringence need to be determined.

Half Wave Plate

A Half Wave Plate (HWP) can introduce a phase difference of π between the o-ray and e-ray in a linear polarized light. If the incident light has a polarization parallel to the optical axis, the polarization state after the retarder will remain unchanged. However, if the polarization is at an angle θ with respect to the optical axis as depicted in Figure 9 (left), the polarization component parallel to the slow axis will travel faster than the polarization component perpendicular to it (or parallel to the fast axis). When the two components exit the crystal their relative phase difference is π and as a result, the polarization is shifted at an additional angle θ, thus 2θ with respect to the optical axis.

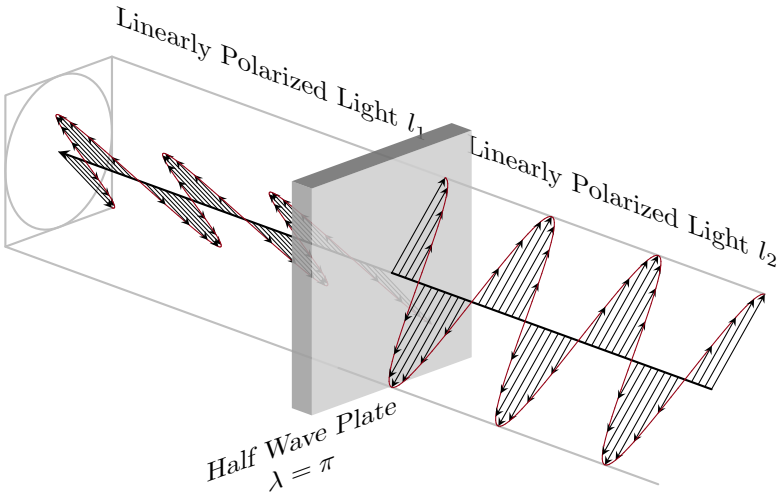

Figure 2.25: A linearly polarized wave traversing a Half Wave Plate. The perpendicularly polarization components exit with a phase difference of π. The combined wave due to interference will have perpendicular polarization ($l_1 \perp l_2$).

Quarter Wave Plate

For a crystal with birefringence Δn, the thickness t of the crystal can be tuned such that for a wavelength λ the relative phase difference is $\pi/2$. Such a retarder is known as a Quarter Wave Plate (QWP).

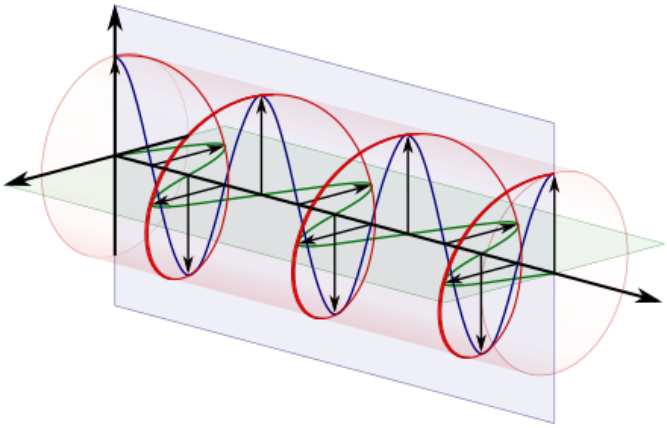

Figure 2.26: Two components with different amplitudes and a phase difference of $\pi/2$ interfering and forming elliptically left-handed/counterclockwise polarized light.
Source: wikimedia.org

These retarders are of particular interest since they can be used for the generation of elliptically or circularly polarized light. When linearly polarized light enters a QWP, the phase shift between the e-ray and o-ray components is $\pi/2$. However, if the incident light is at an angle θ with respect to the optical axis, then the component of the light that experiences the retardance, the e-ray, is smaller (or larger) than the o-ray component. As a result, the interfeing wave will be elliptically polarized (see Figure 2.26).

When the incident polarized light has an angle of $\pi/4$ with respect to the optical axis of the QWP, the amplitudes of the o-ray and e-ray are equal. In this particular case, the output light is circularly polarized Figure 2.27. The fact that circularly polarized light has the same amplitude around the direction of propagation is a feature that is used in a

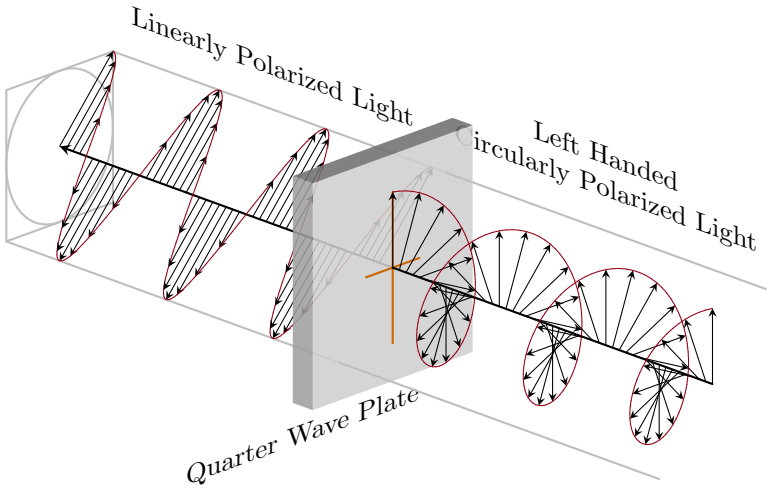

Figure 2.27: Example of a Quarter Wave Plate introducing a phase difference of $\pi/2$ and converting a linear polarized beam to circularly polarized.

variety of birefringent measurement setups as we will see.

The polarization of the incoming photon (or beam) can be resolved as two polarizations on the x and y axis. If the input polarization is parallel to the fast or slow axis, then there is no polarization of the other axis, so the output polarization is the same as the input (only the phase more or less delayed). If the input polarization is 45° to the fast and slow axis, the polarization on those axes are equal. But the phase of the output of the slow axis will be delayed 90° with the output of the fast axis. If not the amplitude but both sine values are displayed, then x and y combined will describe a circle. With other angles than 0° or 45° the values in fast and slow axis will differ and their resultant output will describe an ellipse.

Achromatic Wave Plate

Achromatic (broadband) waveplates (AWP) are a pair of crystalline quartz and magnesium fluoride plates of controlled thickness with crossed fast axes to create a $\lambda/2$ or $\lambda/4$ delay in the broad wavelength range. The difference in dispersion between materials allows the arrangement of a slow phase shift over a broad wavelength range.

Achromatic waveplates are needed for various devices, such as tunable laser sources, multiple laser line systems, and other broad-spectrum sources. Achromatic (Broadband) waveplates could be used to replace a number of single-wavelength quartz waveplates, making your system more convenient and easier to use.

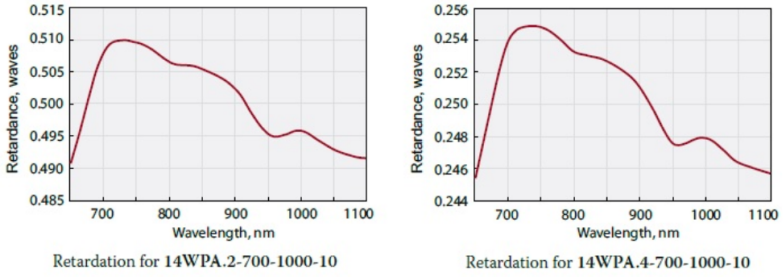

Figure 2.28: Typical retardation curves for 650-1100 nm achromatic waveplates. Source: standaphotonics.com

2.5 Retardance/Birefringence Measurements

The state-of-the-art setups used to identify birefringent properties of samples are presented in this section. The setups are presented in what is considered to be an order of increasing complexity, both in terms of the number of optical elements involved but also regarding the nature of the unknown parameters of the samples under study.

In general, all birefringence measurement setups consist of four parts: the source, the polarization state generator (PSG), the polarization state detection (PSD) and naturally the sample under test (see Figure 12). The source can be a monochromatic or polychromatic where the later allows the utilization of spectroscopy methods and can be a very powerful tool.

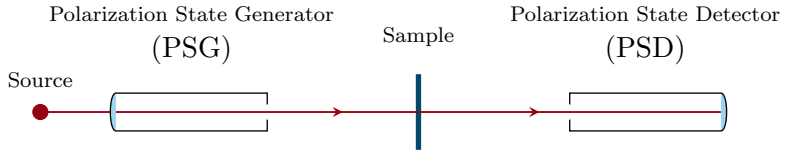

Figure 2.29: General concept of a birefringence measurement setup. The sample is placed between the polarization state generator (PSG) and the polarization state detection (PSD).

The PSG is placed after the source and converts the light to a desired polarization state (e.g. linear, circular). The polarized light passes through the birefringent sample and exits with a different polarization state. The PSD isolates those polarization components of interest which are then measured by one or multiple detectors. In all setups we assume that the light exiting the setup is measure by a detector (e.g. CCD camera) that is a part of the PSD.

2.5.1 Crossed Polarizers

When studying birefringent samples, it is often desired to isolate the sample from the non-birefringent background. This can be achieved by using a pair of polarizers and placing them such that their azimuths are in an angle of $\pi/2$ as shown in Figure 2.30(a). Light exiting the first polarizer (blue) will have a horizontal polarization. By placing the second polarizer vertically with respect to the first polarizer light is filtered out since there is no component with vertical polarization [7]. In this setup the second polarizer, the one closer to the detector, is usually called analyzer.

Suppose we have a birefringent image with its optical axis (dashed line) on the plane perpendicular to the incident light. For a sample with positive birefringence, the o-ray (red) is parallel to the optical axis. If the sample is placed between the polarizers at an angle θ, as shown in Figure 2.30(b), it will behave as a retarder and introduce a phase difference to the e-ray component (green) perpendicular to its optical axis. The interference of the e-ray and o-ray can be visualized as a projection on the analyzer (magenta).

If the angle of the o-ray with respect to the first polarizer is $\pi/4$, then the projection on the analyzer reaches its maximum value. This appears in the detector as the maximum detected light intensity. We have shown that birefringence is a function of retardation Γ and thickness. For samples like fibers, that their thickness is approximately as their width due to the cylindrical shape, we can study how a birefringent fiber behaves between the crossed polarizers. A fiber has a thickness that may vary from a few μm's up to tenths of μm's. If the incident light consists of many bands then a variety of interference colors will appear as shown in Figure 2.31(right). To determine the birefringence of the sample, one needs to measure the retardance by compensating known values of additional retardation. A method of how this is performed is explained in the next section.

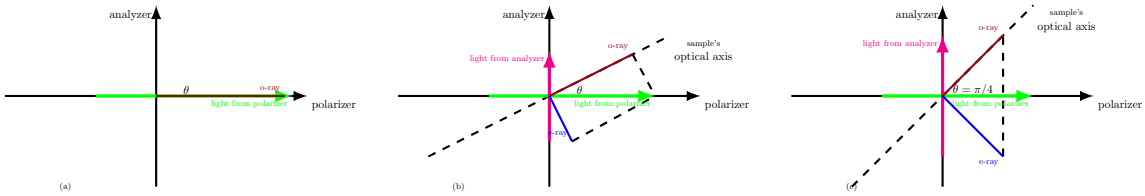

Figure 2.30: The effect of the orientation of the sample's optical axis (OA) on the total light intensity measured after the analyzer in the crossed polarizers setup when the OA is at 0° (a), an arbitrary angle θ (b) and 45° (c).

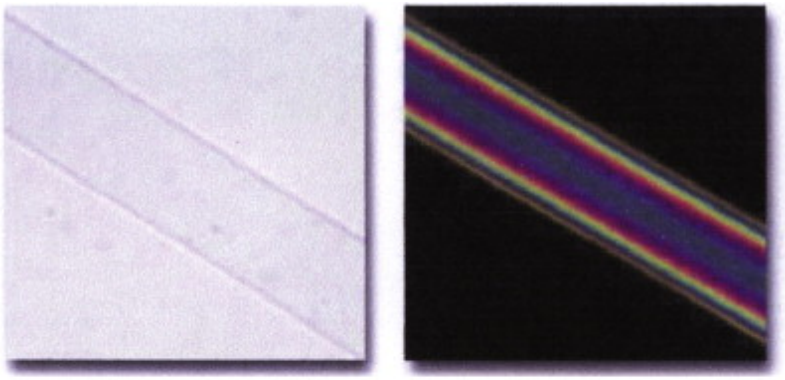

Figure 2.31: Indicative of the fiber's polymer and molecular organization, interference colors can be used to help determine what kind of fiber is being examined.
Source: [9]

2.5.2 Crossed Polarizers with Compensator

A common method used in polarization microscopy for the calculation of birefringence in a sample is based on adding known values of retardances and measuring the maximum interference color.

Suppose our sample consists of a birefringent fiber or crystal. Following the setup described in Figure 2.30(c), we place the sample with its slow axis at $\pi/4$ with respect to the first polarizer. A so-called compensator (e.g. a Full Wave Plate) is then added along the light path with its slow axis at the same orientation as the sample. This relative orientation between **polarizer-compensator-sample-analyzer** not only ensures the maximum intensity of the detected light but also the maximum interference between the o-ray and e-ray of all birefringent elements.

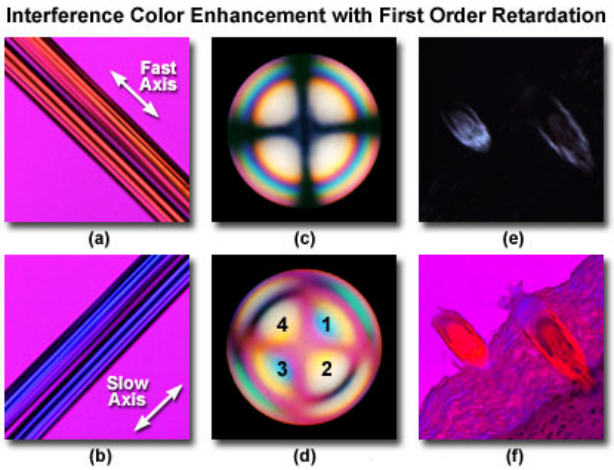

Figure 2.32: Measuring the maximum interference color.
Source: [10]

The result with a FWP, which acts as a compensator, along the light path is shown in Figure 2.32(b). The magenta background appears as a combination of the polarizing/retarding elements and the nature of the source. All light passing the first polarizer is linearly polarized but the FWP of 540 nm introduces a phase difference of exactly 2π only on the green light. As a result, all wavelengths but green are elliptically polarized due to the FWP so any wave with a polarization component will eventually cross the analyzer. Green however keeps its original linear (horizontal) polarization so it will cross the (vertically placed) analyzer (see: [10] Fig. 2). To measure birefringence on an unknown sample with this setup, a variable compensator is needed. The variable compensator is tuned such that compensates the sample's retardance and the sample appears black. This known value of retardance is then used to calculate birefringence either with the Michel-Levy chart or with Equation 2.4.4.1.

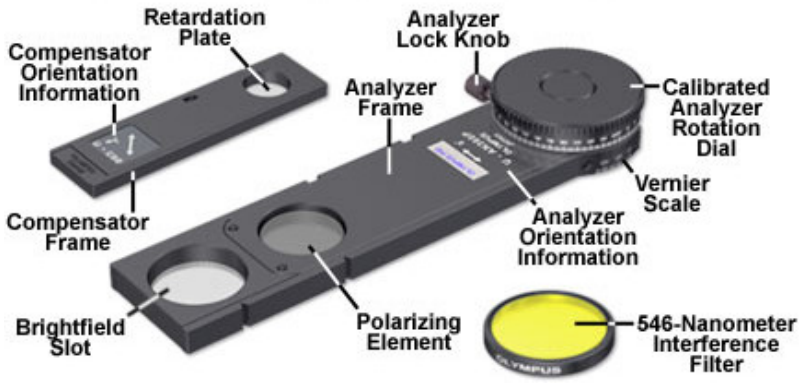

Figure 2.33: The basic optical components necessary to conduct compensation retardation measurements.

Source: olympus-lifescience.com

However, this setup is limited by the dynamic ranges of the available compensators. Moreover, if the samples have different birefringence values then the compensator needs to be tuned and rotated for each measurement making the setup slow and **can not measure in real-time**. A motorized auto adjustment solution is absent from current industry options. This makes this solution sub-optimal and comes in conflict with the high throughput requirements of our imaging system

2.5.3 The Interference Color chart

We consider the case that we will encounter in our studies, that is illumination with white light (polychromatic light). If a crystal is illuminated by white light is viewed with the crossed polarizers off the extinction position, colors, known as interference colors will be seen. These colors result from unequal transmission by the analyzer of the various components of white light. These wavelengths are seen depending on the retardation or path difference produced in the crystal for each of the wavelengths. Let's look at a couple of examples.

Imagine a crystal that has a thickness and birefringence that produces a retardation of 550 nm viewed 45° off extinction. If we look at the graph of Figure 2.34, we can determine the % transmission by the analyzer of some of the components of white light to construct a curve of % transmitted by the Analyzer versus wavelength of light.

This is plotted in the solid curve in Figure 2.35. Note that violet and some blue, as well as some red wavelengths are transmitted, while less of the green yellow and orange wavelengths are transmitted by the analyzer. Thus, the crystal will show an interference color that is reddish violet. We call this color first order, or 1^{st} red.

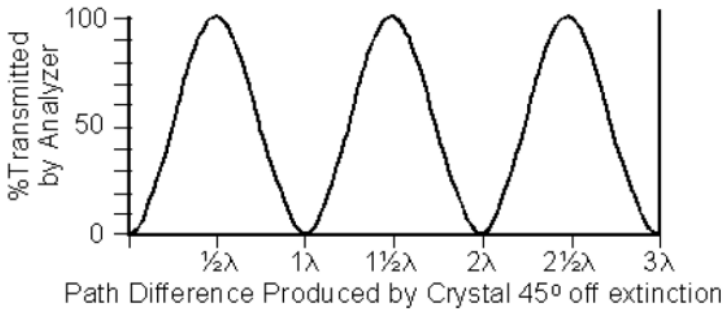

Figure 2.34: Path difference produced by crystal.
Source: [11]

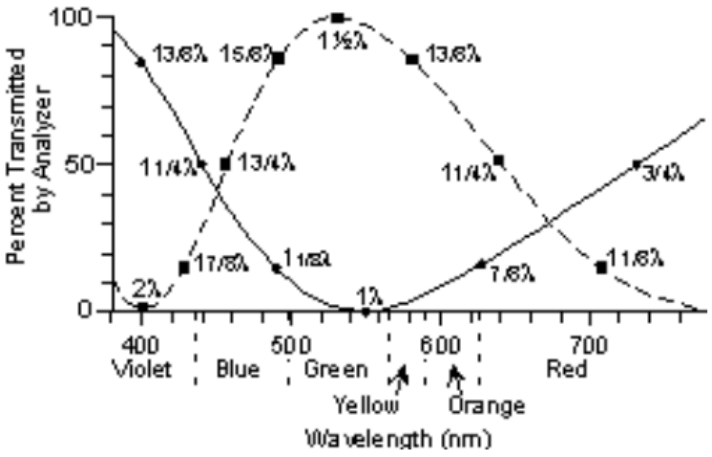

Figure 2.35: Transmission versus wavelength of birefringent material.
Source: [11]

If the crystal produces a retardation of 800 nm, the dashed curve would be obtained. This curve shows little transmission of the violet and red wavelengths, and partial to full transmission of the green, yellow, and orange wavelengths. Thus the crystal will have a greenish interference color.

If this is done for all possible retardations and all wavelengths of light, it produces what is called an interference color chart, or the Michel-Levy chart, shown below. This chart has thickness of the crystal plotted on the y-axis and path difference or retardation, Δ, plotted on the x-axis. The interference colors are divided into orders, every 550 nm of path difference, only 6 orders are shown. Note that first order colors range from black to reddish violet. Blue only appears in the 2^{nd} and 3^{rd} order colors, higher orders have mainly pink and green shades.

The Michel-Levy chart (Figure 2.36) is a form of look-up table that is based on measuring the retardation, to calculate the birefringence using (Equation 2.4.4.1) [12]. The polarization color of a sample is compared to the colors in the Michel-Levy chart. The maximum interference color per order is identified. Supposedly we have measured that the maximum interference color in a birefringent sample is a second order yellow. This corresponds to a value of retardance of ~ 900 nm. If the thickness of the sample is known, e.g. $15\mu m$, then the birefringence can be tracked in the chart. In this case it is about 0.065.

The use of Michel-Levy chart, provides a direct measurement of birefringence via the

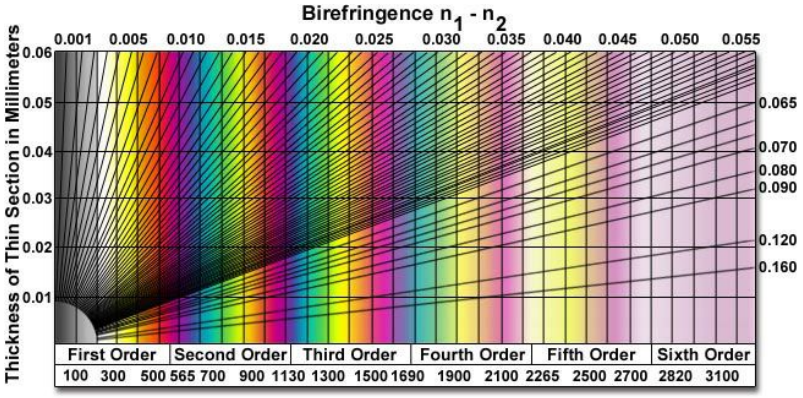

Figure 2.36: The Michel-Levy color chart.
Source: olympus-lifescience.com

generated polarization colors but offers poor discrimination in for higher orders. Plotted on the chart are diagonal lines representing various values of birefringence $n_1 - n_2$ in this case. Thus, if the thickness of the crystal is known, the birefringence for the privileged directions can be determined from the interference color. For example a 0.03 mm thin section crystal that shows 1^{st} red interference colors has a birefringence of about 0.018.

2.5.4 Spectrometric Imaging

A method to measure the retardance of birefringent fibers without the use of a compensator is provided by NFI [13]. The setup is based on the two crossed polarizers concept described in Section 2.5.1, with the birefringent samples under investigation placed such that their optical axis is at 45° with respect to the first polarizer. A liquid crystal tunable filter (LCTF), which acts as both a spectrometer and a polarizing filter, measures the intensity for each wavelength of the halogen light source. A schematic of the setup is shown in Figure 2.37.

The birefringent sample can be described as a retarder with unknown retardance δ. By having the fibers oriented with their optical axis at 45°, the intensity measured by the detector will be maximum as shown in Figure 2.30(c).

Using the LCTF, the polarization spectrum can be measured. Since the retardance δ is a function of the wavelength λ, the measured spectrum will have an oscillating shape due to interference variations between each wavelength. The higher the retardation Γ, the more frequent the oscillations in the measured wavelength range.

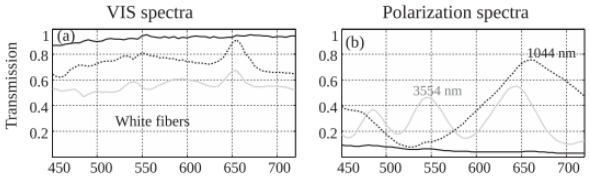

Figure 2.38: VIS and Polarization spectra for acrylic (black), polyester (gray) and polyamide (black dotted). The calculated retardation is shown for two curves.

Source: [13]

In Figure 2.38 the polarization spectra for three different fibers made of difference materials are plotted. The thickness of all fibers tested is known. The retardation for each sample was calculated by comparing the closest theoretical polarization spectrum to the experimental data and the birefringence for each material was then calculated using Equation 2.4.4.1. The calculated birefringence for the samples tested are found to be in good agreement with the expected values of birefringence. Note however that for small values of retardances the oscillation shape is so low frequent that determination of the retardance is not possible.

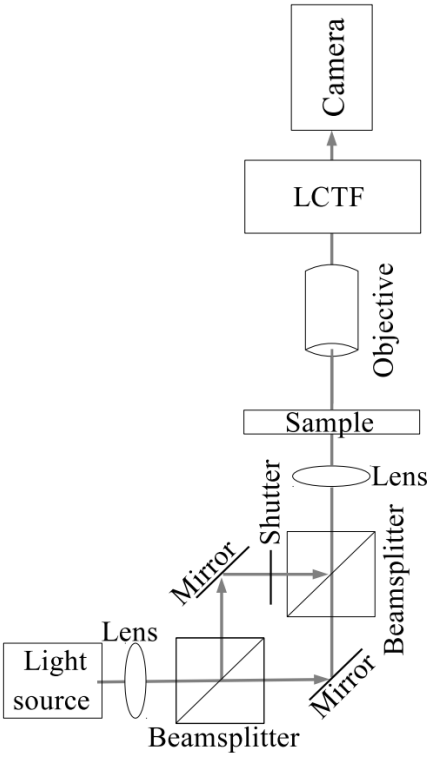

Figure 2.37: The instrumentation proposed in [13], patent pending. The light incident on the sample can either be polarized or depolarized by closing and opening the shutter.

To summarize, the spectrometric method provides a measurement of retardance for a large range (lowest value quoted was 900 nm, highest value quoted was 4600 nm). However, the setup proposed here is not orientation independent since it requires to set the samples at a specific angle. It is limited by the spectra range of the source, which can be extended however by measuring at the UV or IR region. Finally, it is not real-time since it is limited by the measurements of the LCTF. However, the spectrometric method shows some potential since it does not depend on the use of a variable compensator for the measurement of retardation.

2.5.5 Orientation Independent Spectrometric Imaging

A theoretical extension of the spectrometric imaging principle of Figure 2.37 aims to remove the orientation dependency of the sample by adding two retarders. This so-called orientation independent setup is depicted in Figure 2.39.

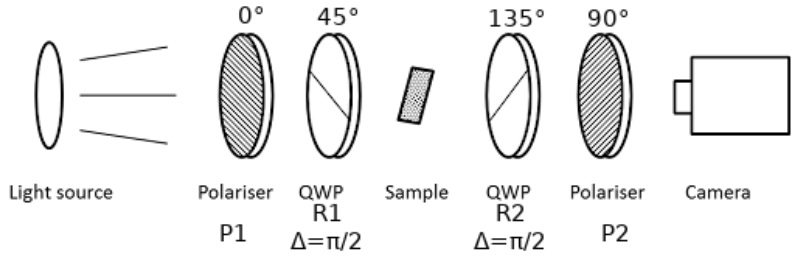

Figure 2.39: Extension of the setup 2.37 with achromatic QWP for orientation independent birefringence measurements.

In this case, the polarization state generator (PSG) is responsible for generating circularly polarized light. Circularly polarized light is generated when a QWP, in the image notes as R1, is placed at an angle of $\pi/4$ after a linear polarizer P1. It is important to note that since the source is a polychromatic beam, in order to apply a retardance of $\pi/2$ on all incident wavelengths an achromatic QWP needs to be used.

The concept of the polarization state detector (PSD) is to receive the circularly polarized light and convert it to linearly polarized at a specific orientation. By adding a second achromatic QWP, in the image noted as R2, the conversion from circular to linear polarization is achieved. The orientation of R2 defines the orientation of the linear polarization. By setting R2 at $\pi/2$ with respect to R1 of the PSG, the output polarized light will have its polarization state at $\pi/2$ with respect to the 1st polarizer. Thus, by setting a second polarizer P2 at that angle, no light passes through. This setup is an extension of the setup with the crossed polarizers with the only difference being that between the two polarizers we have circular polarization of a polychromatic beam.

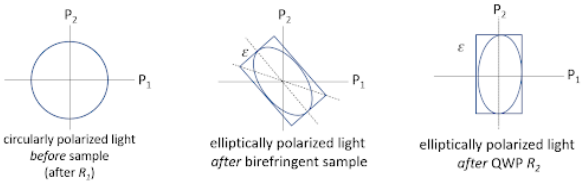

Figure 2.40: Evolution of the polarization state of one wavelength for the orientation independent setup.

Let us follow the evolution of the polarization states for a wavelength λ Figure 2.40. After the PSG and right before the sample, the light will be circularly polarized as shown in Figure 2.40. The sample is described as a retarder with unknown retardance δ set with its optical axis at an unknown angle θ with respect to the azimuth of the first polarizer P1. When the light exits the sample, it will be elliptically polarized as shown in Figure 2.40(center). The ellipticity is a function of the retardance δ, which of course is a function of λ. By introducing an additional retardance of $\pi/2$ the ellipticity is conserved and the long axis of the ellipse is shifted such that it matches the orientation of the second polarizer P2 as shown in Figure 2.40(right). As a result, the maximum intensity is measured by the detector.

According to the theoretical work on [15], the retardation and as a result birefringence can be fitted from the polarization spectra similarly to the method explained in setup 2.37. However, this method does not take into account the fact that the total intensity measured will also include polarization and interference patterns from those parts of the fiber that are in arbitrary angles. Also, there is no mention whether it can be performed in real-time.

A method that attempts to solve the orientation problem and on the same time addresses the issue of additional intensities from parts of the sample in arbitrary orientations is presented in the following section.

2.5.6 2-D birefringence distributions with the LC-PolScope

A technique for a fast measurement of the 2-dimentional birefringence distribution in a sample is described in [16]. The technique utilized, which is also available as a commercial tool under the trademark LC-PolScope [17], is depicted in Figure 2.41.

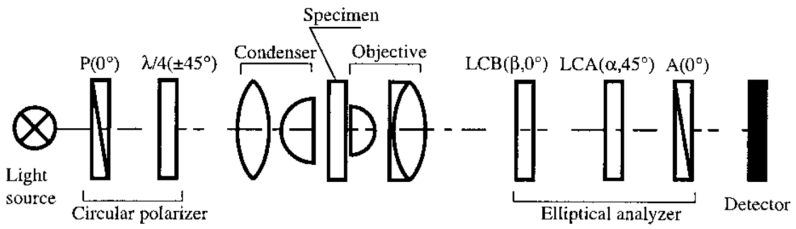

Figure 2.41: Schematic of the LC-PolScope principle. The PSG consists is a circular polarizer and the PSD of a combination of 2 retarders and a polarizer.
Source: [16]

The setup consists of a monochromatic source that intercepts a so-called circular polarizer, which is basically a combination of a linear polarizer and an achromatic QWP. The QWP, is set at 45° with respect to the polarizer's azimuth. The PSD in this case consists of a combination of two retarders and a polarizer. The retarders, LCA and LCB have retardances α and β respectively. Note that in this dual-retarder setup, the background will not appear dark like in all setups described so far but will have an illumination component as in the example with the FWP in Figure 2.32(b). This is referred to as the depolarized background illumination that will be described as an additional term in the measured light intensities.

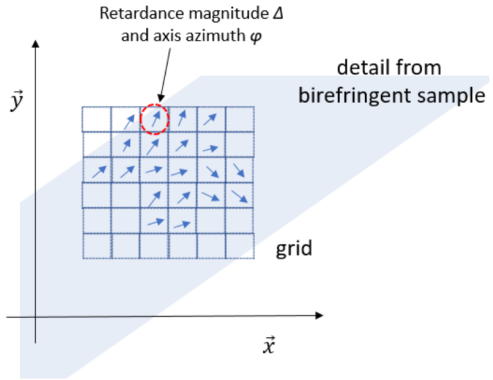

(a) Segmentation of a birefringent sample in a 2D grid. The concept of the setup is to measure the retardance Δ and slow axis angle ϕ for each segment of the distribution.

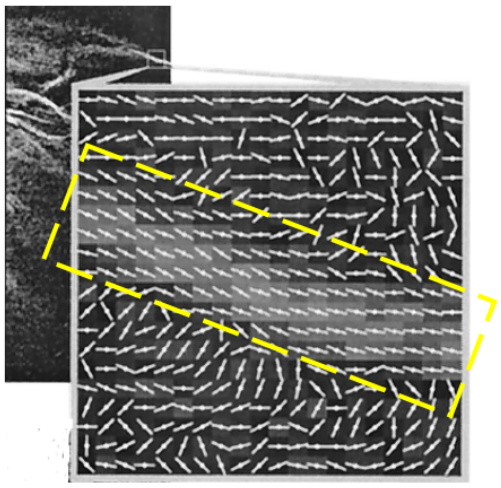

(b) Enlarged detail showing low (black) and high (white) retardance values in each pixel with the overlaid lines corresponding to slow axis orientation. The yellow region is a birefringent microtube in which all birefringent axes are coparallel. Source: [16]

Figure 2.42: Visual representation of 2D birefringence.

One of the particularly interesting features in this technique is the assumption that the sample is a two-dimensional distribution of segmented linear retarders with retardances $\Delta(x, y)$ and slow axis angles $\phi(x, y)$ as depicted in Figure 2.42a. Having an imaging detector with substantial spatial resolution, the distribution of intensities is measured for a combination of retarder settings.

An example of the 2D distributions of the $\Delta(x, y)$ and slow axis angles $\phi(x, y)$ of a birefringent sample is shown in Figure 2.42b. The enlarged detail shows the magnitude of retardances in each pixel (black corresponds to low and white to high retardance values) and the overlaid lines correspond to the orientation of the slow axis. When superimposed to the original image, the white region with the aligned arrows corresponds to the parallel birefringent axis of the microtube.

The LC-PolScope technique shows great potential. The reconstruction of a 2D distribution grid with retardances and slow axis orientation can provide essential information regarding the nature of birefringent samples. Although measurements cannot be performed in real-time due to the number of frames required, this method can be adjusted to our equipment as will be discussed in the following sections.

2.5.7 Extracting Linear Polarization components

An apparatus that follows a different method for the measurement of birefringence is described in [18]. This technique is based on measuring the linear polarization components after the sample (similar to a Stokes meter [19]) and calculating birefringence on the basis of the Stokes parameters.

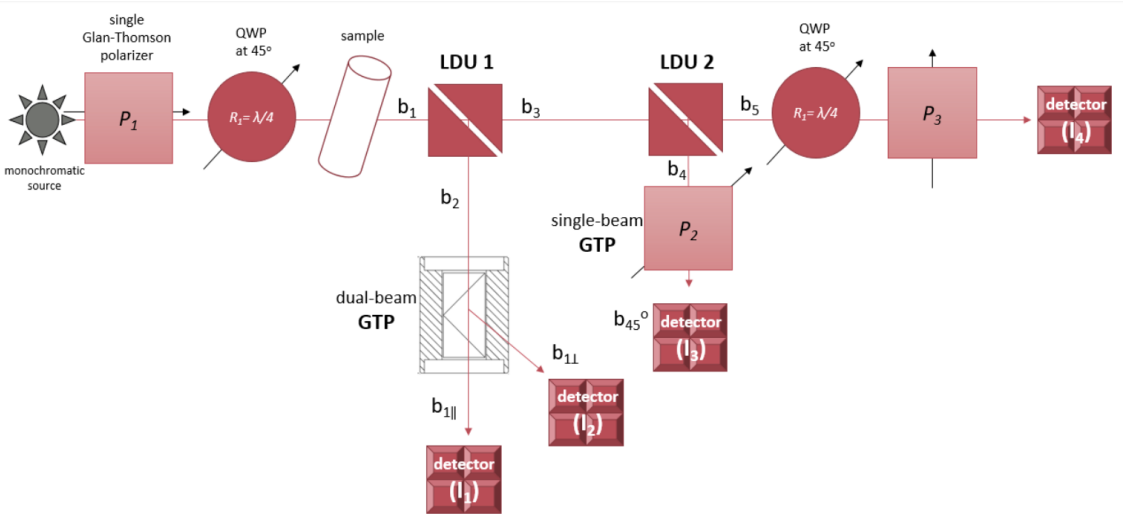

Figure 2.43: Schematic of apparatus that measures linear polarization components (similarly to a Stokes meter). The birefringence is calculated as a function of the Stokes parameters.

A schematic of the apparatus is drawn in Figure 2.43. A monochromatic source becomes circular polarized after crossing a combination of a linear polarizer and a QWP, P1 and R1 respectively. The light exiting the sample at b_1 will be elliptically polarized. The technique used to measure the linear components of the sample's orientation is based on dividing the polarization state and measuring each time a different polarization component. Two so-called light dividing units (LDU) are used to split the beam to the beams $b_2 - b_5$ while maintaining the polarization state at each beam. The first light dividing unit, LDU 1, is placed along the path of b1 dividing the beam to b_2 and b_3. Beam b2 is incident on a dual-beam Glan-Thompson prism where it is further divided into two orthogonally

polarized components $b_{\parallel}$ and $b_{\perp}$ corresponding to parallel and orthogonal polarization respectively. These two orthogonal components are measured by the detectors I1 and I2. Beam b_3 is incident on the second light dividing unit LDU 2 and is split to beams b_4 and b_5. Beam b_4 is incident on a single-beam Glan-Thomson with its transmission axis set at 45°. The b_{45° component is measured by the detector I3. The last divided beam b_5 is incident on a combination of a QWP R2 with its axis set at 45° and a polarizer P3 with its axis perpendicular to the first polarizer P1. The exiting light b_c is measured by the detector I4 and is related to the elliptical/circular component of the Stokes vector.

Using the combination of light diving units and polarizers the components $b_{\parallel}$, $b_{\perp}$, b_{45° and b_c are measured by the detectors I1, I2, I3 and I4 respectively. These intensities are associated to the Stokes parameters S0, S1, S2, S3 described in Section 2.4.5 with the following equations (see also [6]):

$$\begin{aligned} S_0 &\simeq (I_1 + I_2) \\ S_1 &\simeq (I_1 - I_2) \\ S_2 &\simeq (2I_3 - S_0) \\ S_3 &\simeq (S_0 - 2I_2) \end{aligned} \tag{2.5.7.1}$$

Using the Equations 2.3.5.3, 2.3.5.4, 2.3.5.5 and the formula of birefringence with respect to eccentricity $\boxed{B = \frac{\pi}{2} - 2e}$:

$$B = \frac{\pi}{2} - 2\left(\frac{S_3}{S_0 + \sqrt{S_1^2 + S_2^2}}\right) \tag{2.5.7.2}$$

To summarize, this technique provides a full measurement of the polarization components in order to calculate birefringence. It contains no moving parts and can be applied in real-time, therefore is shows great potential to form a basis for ‘‘`A novel multi modal high throughput screening and material identification imaging system`’’ setup.

2.5.8 Summary of current setups

The methods described in the previous sections are summarized in Table 2.1.

Source	Method	Pros	Cons
[13]	Spectrometric imaging	· Simple	· Linear retarder assumption · Orientation Dependency · Multiple order limitation · **Not real-time**
[13]	Orientation Independent Spectrometric imaging	· Simple · Orientation Independent	· Linear retarder assumption · Error prone fit · **Not real-time**
[17]	2-D birefringence distributions with the LC-PolScope	· Fine birefringence results · Orientation Independent	· Involves moving parts · high cost · **Not real-time** · Needs more incident wavelengths · Maximum retardance value is half the λ of the incoming monochromatic light
[18]	Extracting Linear Polarization Components	· No moving parts · Orientation Independent · **Real-time**	· Complicated setup · **Rotation dependent** · **Only point measurements** · Not real-time retardance measurments · No calculation of optical axis

Table 2.1: Summary of current birefringence measurement setups.

The principles of the LC-PolScope [17], in which a 2D distribution of the birefringence and axis orientation is calculated, could be adjusted to our hyperspectral equipment in order to yield a robust retardance measurement and phase **order calculation** (see Figure 2.36). In addition, the apparatus described in [18] provides a very good basis which could be simplified in order to fit our **real-time** requirements.

Chapter 3

A novel polarization imaging module

3.1 Retardance measurements

Many important optical materials exhibit birefringence. Birefringence means that different linear polarizations of light travel at different speeds through the material. These different polarizations are most often considered as two components of the polarized light, one being orthogonal to the other.

Birefringence is an intrinsic property of many optical materials, and may also be induced by external forces. Retardation or retardance represents the integrated effect of birefringence acting along the path of a light beam traversing the sample. If the incident light beam is linearly polarized, two orthogonal components of the polarized light will exit the sample with a phase difference, called the retardance. The fundamental unit of retardance is length, Such as nanometers (nm). It is frequently convenient, however, to express retardance in units of phase angle (waves, radians, or degrees), which is proportional to the retardance (nm) divided by the wavelength of the light (nm). An "average" birefringence for a sample is sometimes computed by dividing the measured retardance magnitude by the thickness of the sample.

As discussed in chapter "Retardance/Birefringence Measurements" there exists a well established instrumentation that can measure retardation adequately. Nevertheless, non of them is focused on **video rate and real-time measurements**. For this reason we took a challenge designing a complete imaging system that can yield as much information from the sample as possible. The goal of this thesis is designing the polarization imaging component of such a system such that it can yield retardance values in real-time.

Retardation has a periodic behavior, as shown in Figure 2.34, and a proper identification of its order is required in order to make use of Figure 2.36. For that reason a spectrometric approach is required and this can be established by using a multi-spectral (MS) detector. Having the transmission spectra in both MS imaging and polarization imaging modalities provides a rich, multi dimensional, **feature space** that can be exploited to have a strong differentiation between similar samples. The approach is to "unwrap" the measured retardance into the absolute retardance using multiple wavelength measurements. This method is applicable to single point measurement of multiple wavelengths, and is thus equally valid for either imaging or point based measurement systems.

Some prior phase unwrapping techniques rely solely upon the identification of the peak regions and their gradients. These methods require robust treatment of spatial information and are prone to errors. The multi-wavelength method of the proposed design, on the other hand, is based upon the information for a single point and less prone to error induced by samples with large spatial diversity. We will therefore avoid using a fitting/predictive

mathematical model and rely upon multiple wavelength measurement in order to yield the actual retardance values just by applying a lookup table.

3.1.1 System Requirements

- **Light Source**
  - Broadband Light
    The wavelengths of the emitted light should be broad. This means that the visible (VIS) spectrum as well as the near infrared (NIR) must be used. This part of the light spectrum is cheap to produce with LEDs and makes the multi modal feature space of each sample broader and at the same time easier to have distinct wavelengths for retardance measurements.
  - Homogenised Beam
    The light should be homogeneous before entering the polarization state generator.
  - Unpolarized state
    The light should be unpolarized in order to be circularly polarized by the polarization state generator as uniformly as possible.
- **Polarization State Generator**
  - Circularly clockwise polarized light
    For every system, in order to identify the transfer function we need to provide a known input and measure the output. The same applies in optical systems. For our microscope, the light before entering the sample should be circularly clockwise polarized so that the polarization state of light detected after leaving the sample can be correlated to the optical properties of the sample.
- **Polarization State Detector**
  - Polarization Component Decomposition
    Like the Stokes meter described in Figure 2.43, the polarisation state detector, should easily (without moving parts) and correctly decompose the polarization state of light into its core components.
  - Extinction Ratio
    An extinction ratio represents the relationship between the maximum and minimum amount of transmitted polarized light through a polarizer. In order to have distinct linear polarization components we require the Extinction Ratio to be > 100.0 for the VIS and NIR spectrum.
- **Camera**
  - Global Shutter function
    Existing CMOS image sensors are unable to accurately identify fast-moving objects, due to the focal plane distortion, which is caused by the rolling shutter function. Global shutter function enables high-picture-quality without focal plane distortion by providing an analog memory inside each pixel.
  - High Frame Rate
    The camera should have > 60 frames per second (FPS) while also providing a trigger mode functionality in order to being able of having fast video feed, as well as, perfectly timed snapshots.

– Polarization Component registration
Each RAW image of the individual polarization components should be spatially co-registered. This means that there will be an algorithm that aligns the RAW data. The algorithm may be, for example, embodied as software or firmware instructions carried out by a digital computer.

3.1.2 High-throughput Screening (HTS)

Advances in molecular biology, human genetics and functional genomics continue to produce increasing numbers of molecular targets available for therapeutic intervention. This, coupled with major increases in compound collections produced by combinatorial technologies, has fueled an important need for improvements in high-throughput screening (HTS) capabilities. As a result, HTS technologies have undergone a revolution in the latter half of the 1990s. Today, most pharmaceutical companies use HTS as the primary engine driving lead discovery.

The increased reliance on HTS labs meant that screening had to change. Assay systems and robotics that were capable of screening thousands of compounds per day in the mid-1990s had to evolve into ultraHTS (uHTS) methods capable of 100,000 assays per day, or more. This explosion in assay throughput meant that reagent production had to be scaled to meet the challenge — or else the HTS labs would have to miniaturize assays to meet the reagent suppliers halfway. Fortunately, many of the technological advances required to reach the goals of miniaturized uHTS have been established and are on their way toward routine use.

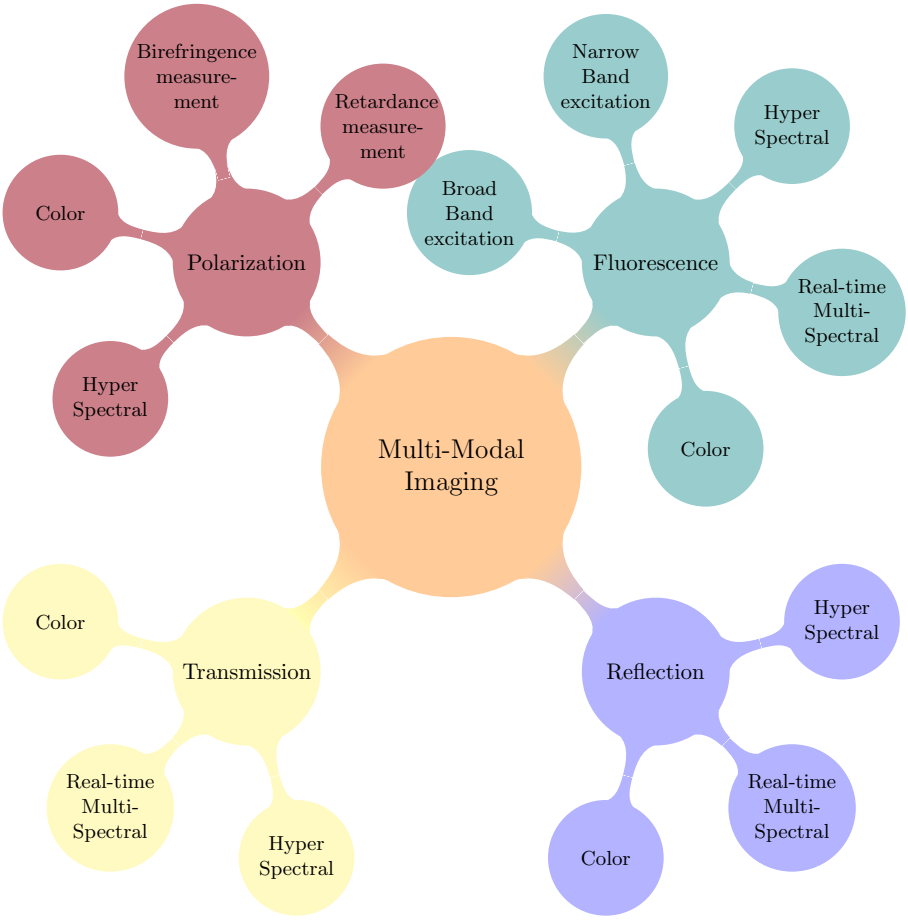

Figure 3.1: Multi Modal imaging graph, illustrating some imaging modalities that can be utilized in HTS.

The electronics laboratory of Technical University of Crete is investing its know-how on the Multi Modal Hyper Spectral Imaging to develop novel HTS technologies. The applications of HTS are broad and the technological advancements of our time pushes scientists and engineers towards complex optimization problems. To automate and optimize the process of sample detection and classification, there exist two approaches. 1) is to have as much *low-dimensional* data in order to morph a **stochastic** model that can identify and classify any sample that was trained to do so. 2) is to have the means of producing *high-dimensional* data, that are almost guaranteed to have a hyperplane that can differentiate one sample from another in a **deterministic** manner. Of course, a combination of the two approaches may be the ultimate, but currently due to the lack of multidimensional datasets in industry and academia, the development of such stochastic models straggles.

For our approach (2) we have found that: **each sample can be uniquely identified by a multidimensional feature space.** Each imaging modality introduces another -usually- orthogonal dimension for a sample's identity and enhancing Color Imaging to Multi or even Hyper spectral Imaging makes each dimension's dataset denser. By adding more and more modalities, one can cave higher certainty about a sample's classification because the orthogonal nature of the data comes from different chemical aspects of a compound.

The *"Transmission"* imaging modality tackles the molecular structure of the sample and the intensity of the absorption, as a function of frequency, varies from one compound to another.The *"Fluorescense"* imaging modality primarily tackles the electronic structure of the sample and the *"Reflection"* imaging modality can tackle the molecular structure of the sample as a function of frequency while also providing useful morphological representation. Lastly, the *"Polarization"* imaging modality can provide information regarding the crystal structure of the material.

HTS usually uses only **fluorescence** imaging to recognize different compounds. This is due to the high contrast of this imaging modality and the ease of image segmentation. A segmented material in the image will have a higher dimensionality and a more complete, non-destructive chemical representation if other modalities can be measured in **real-time**. This is why the need of real-time retardance measurements can find use in all HTS applications.

An example of the available technologies that our optoelectronics laboratory have developed for real-time imaging that can be utilized in HTS is illustrated in Figure 3.1.

3.2 HTS transmission-fluorescence Microscope

For the purpose of this research, we gained access to a HTS transmission-fluorescence multimodal Microscope, as shown in Figure 3.2. The Lumnia microscopes are built upon an innovative modular design comprising a basic digital microscope platform and several add-on units. All Lumnia versions come with the SMMART-HTS software suite, which is operated through a touch screen-based graphical user-interface.

The Lumnia Microscope is a multimodal microscope that can be used in a variety of applications. It is equipped with a moving X-Y stage and can create overviews of samples in any acquisition mode. It is equipped with the **MUSES9-MS** Multi Spectral (MS) Complementary Metal Oxide Semiconductor (CMOS) camera sensor and can acquire MS bright field transmission imaging, as well as color reflection and fluorescence. The polyline light source (a diode laser array) is an epi-illumination system integrated as an attachment onto the basic microscope platform, providing narrow band and efficient fluorescence excitation. Laser line excitation leaves sufficient spectral space for the imaging module to uncouple the emissions from multiple different fluorophores with overlapping spectra. The whole system is built upon an innovative design allowing for the real-time inspection of multiple fluorophores simultaneously and for the quantitative fluorescence intensity mapping.

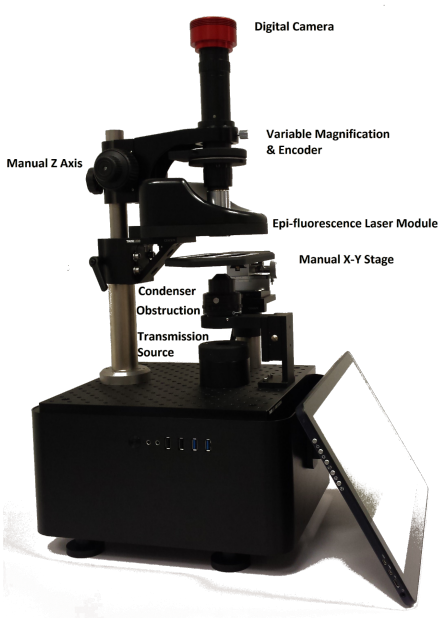

Figure 3.2: A HTS transmission-fluorescence multi modal microscope

Using this microscope and its extended software capabilities, we can configure different automatic acquisition parameters, navigate manually through samples and capture images in different imaging modes with separate controls for each illumination mode. The work of this thesis is to integrate a retartdance measurement module on the Lumnia-FL HTS Multi Modal Microscope through the Polarization imaging modality. This will be achieved by modifying the existing optical setup as well as various firmware and software development that utilizes the General-Purpose computing on Graphics Processing Units (GPGPU) in order to yield **real-time measurements**.

In the following sections of this chapter we will discuss the hardware and software challenges of designing such module and integrating it to the microscope.

3.3 Real-time measurements

3.3.1 Hardware Segmentation

Desired Ellipsometry

In order to yield actual retardance measurements, it is important to firstly define the ellipsometry, or the polarization states that our system will detect. As shown in chapter "Stokes parameters" the states **IV** are adequate for defining the whole polarization states, but so are states **IQU** and the reason is that they are, in a way, complementary.

In order to measure the retardance we need all useful Stoke parameters which for our application that has a real-time requirement are the **IQU**. The four polarization filters described in the Figure 2.13 must be used in the polarisation state detector (PSD) so that all useful information of the polarization state can be obtained. Moreover, to have a good measurement of the sample's optical transfer function (and also the retardance measurement) we need to have a polarization state generator (PSG) that provides circularly polarized light in all wavelengths. This way we can observe for each wavelength how the circular polarization is morphed into an elliptical one. This procedure is illustrated in the following Figure 3.3.

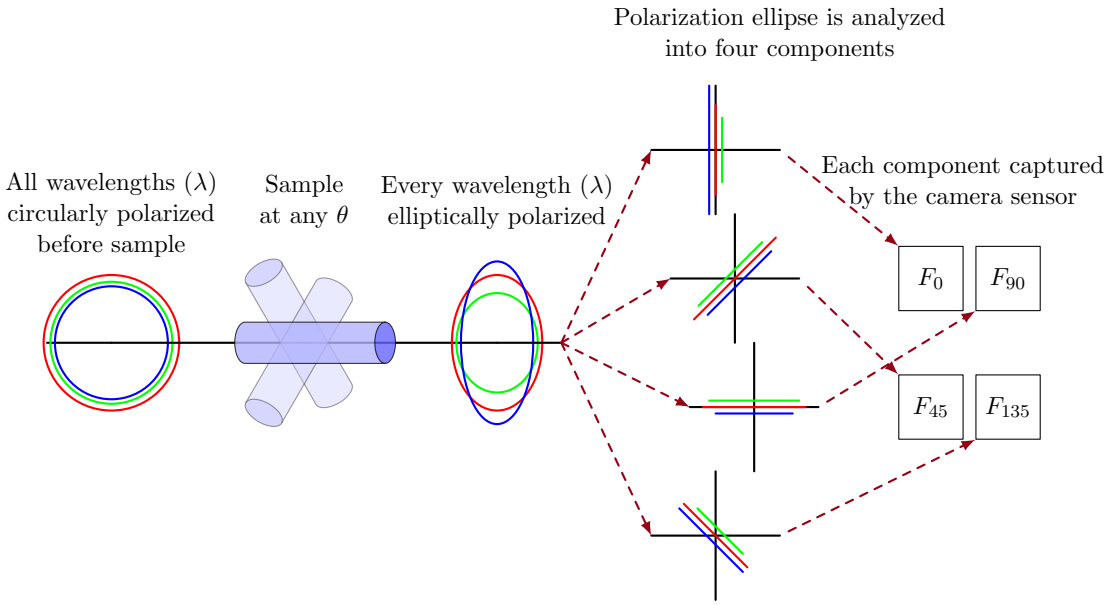

Figure 3.3: The polarization state evolution in the proposed design.

The information an optical system as described can provide is:

Wavelength	F_{0°	F_{45°	F_{90°	F_{135°	$DOLP$
λ_1	$\in [0,1]$	$\in [0,1]$	$\in [0,1]$	$\in [0,1]$	$\in [0,1]$
$\vdots$	$\vdots$	$\vdots$	$\vdots$	$\vdots$	$\vdots$
λ_n	$\in [0,1]$	$\in [0,1]$	$\in [0,1]$	$\in [0,1]$	$\in [0,1]$

Table 3.1: The expected ellipsometry data the microscope will provide in real-time.

Having spectral data for each polarization degree and the useful parameter 2.3.6.4 (DOLP) we can have a real time retardation order estimation as described in [13]. By calculating the order we can compensate the periodic nature of retardance while having more robust birefringence measurements.

Polarization State Generator (PSG)

Light Source

The system's light source is an LED multiplexer, meaning that any part of the visible (VIS) and near infrared (NIR) can be selected, multiplexed, homogenized and emitted with a specified polarization state.

- **LEDs**

  The wavelengths of the emitted light should be broad. This means that the visible (VIS) spectrum as well as the near infrared (NIR) must be used. This part of the light spectrum is cheap to produce with LEDs and makes the multi modal feature space of each sample broader and at the same time easier to have distinct wavelengths for retardance measurements.

- **Connectivity**

  Firmware code is optimized with the help of the powerful and very fast cores of the ESP32 low-cost, low-power System on Chip (SoC), running at 240 MHz, by utilizing the needed blocks of it's functional block diagram. This processor can be used for WiFi - Bluetooth - Radio communications, Cryptography, Low-Power applications and of course for Real-Time processing. Our main goal and the reason why this SoC is used, is to implement independently the Ethernet Communication (Hardware Communication) and the fast "General Purpose Input/Output" (GPIO) manipulation (Hardware Drivers).

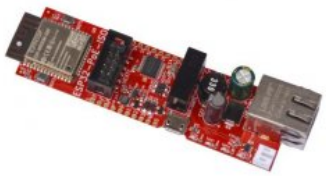

Figure 3.4: The ESP32-PoE is an IoT WIFI/BLE/Ethernet development board with Power-Over-Ethernet (PoE) feature.
Source: olimex.com

  The connectivity is established through the TCP protocol and the Computer running the digital microscope is able to send packages to the micro-controller with firmware instructions to operate the lights.

- **Depolarizing/Homogenizing**

  There exists a need to multiplex every active LED with a beam homogenizer. This is a device that smooths out the irregularities of the light and is convenient because it also acts as the optical waveguide. Light pipe homogenizing rods utilize total internal reflection to homogenize non-uniform light sources regardless of their spectral characteristics. The active LEDs from the broad spectrum LED array are selectable from the ESP32 controller. This results in a modular light source that can either emit narrow or broad band light. Furthermore, the light should be unpolarized before entering the polarization state generator in order to achieve circular polarization. For that reason, a Quartz-Wedge Achromatic Depolarizer is utilized, so that it transforms any input polarization component into an unpolarized one. This behavior is shown in Figure 3.5.

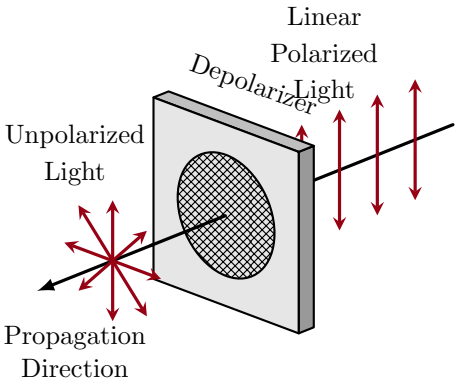

Figure 3.5: Depolarizer diagram.

The complete schematic of our light source is presented below, in Figure 3.6. The computers controls all LEDs individually while a waveguide multiplexes their emission frequency. A depolarizer, then, ensures for a non biased input to the PSG that outputs a circular polarized light, given unpolarized input. An optional condenser then acts as an extra part critical for confocal microscopy.

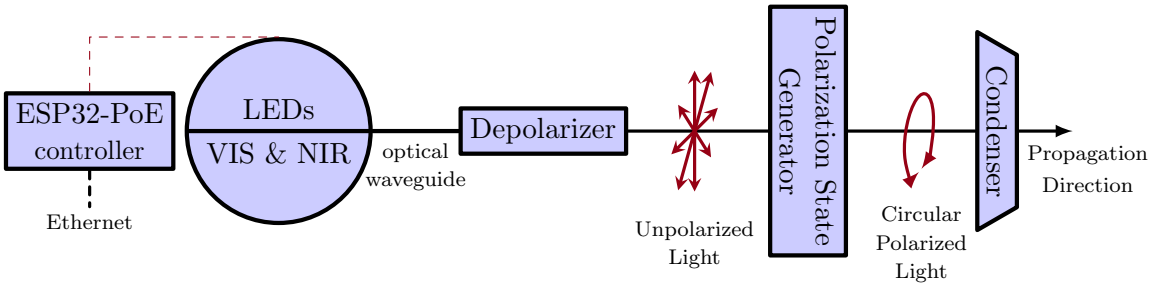

Figure 3.6: Our light source design. LEDs are individually controlled through an Ethernet ESP32 micro-controller. The emitted light can be narrow or broad band and is circular polarized with the use of PSG as shown in Figure 3.7.

Circular Polarizer

For every system, in order to identify the transfer function, a known input needs to be provided and an output measurement to be performed. The same applies in optical systems. For our microscope, the light before entering the sample should be circularly polarized so that the polarization state of light detected after leaving the sample can be correlated to the optical properties of the sample.

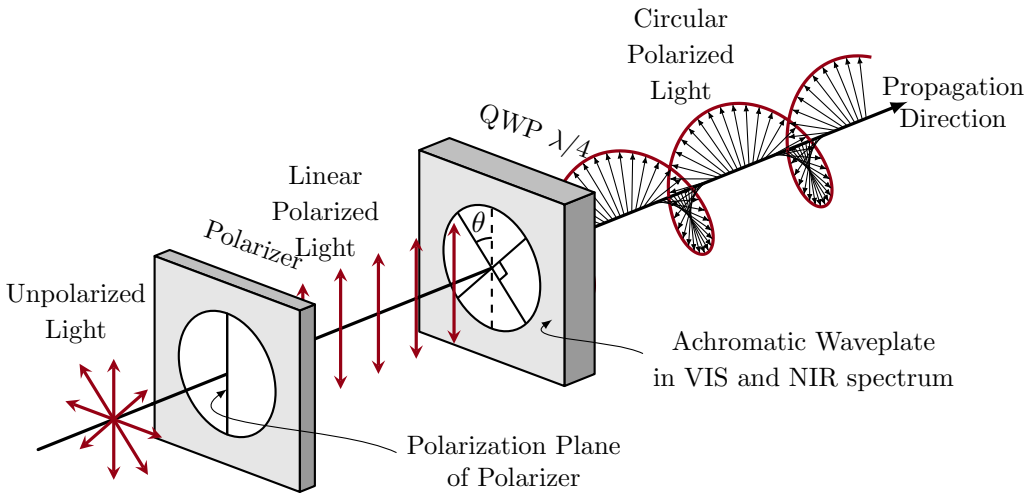

Figure 3.7: Polarization State Generator (PSG).

The PSG includes a linear polarizer that transforms any polarization state into a 0° linear polarized light beam and then an achromatic quarter waveplate transforms the beam into a circularly polarized one. A quarter-wave retarder is used to convert light between circular and linear polarization forms. It changes linearly polarized light to circularly polarized light, when the angle between the input polarization and the retarder fast axis is 45°. In Figure 3.7, linearly polarized light is converted to circular polarized light by the quarter-wave retarder. Upon exiting the quarter-wave retarder, light polarized parallel to the slow axis is retarded by $\lambda/4$ relative to light polarized along the fast axis. When recombined, the exit light is circularly polarized.

Polarization State Detector (PSD) - Camera

A key to real-time imaging applications, is to avoid using moving parts. For that reason it is essential to approach the detector module of the system with an approach similar to that of Figure 2.43, while also trying to keep a low cost. For that reason, a Sony RGB Polar sensor is selected.

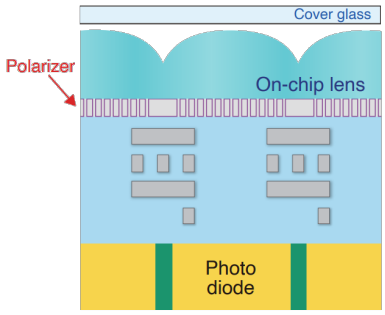

(a) Polarizer is formed on chip under the on-chip lens layer.

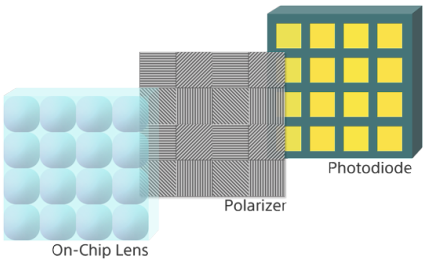

(b) The Bayer filter of the polarization sensors.

Figure 3.8: Sony's RGB polarization imaging sensor.
Source: sony-semicon.co.jp

In the Bayer matrix (named after Dr. Bryce Bayer of Eastman Kodak), a single color filter is placed over each pixel in the mosaic pattern shown in Figure 3.9 (top layer). The filters are similar those used in RGB imaging on a monochrome camera, but the difference lies in the patchwork nature of the matrix. In RGB imaging with a monochrome camera, a red filter is placed over all pixels for one image, a green filter for the next, and a blue for a third. Thus, red, green, and blue signals are measured at each point in the image. Here, each pixel gets only one color – red, green, or blue. (We should note at this point that technically, one should refer to this as a Color Filter Array, or CFA, as there are many possible variants on this basic theme and only this one is properly called a Bayer matrix.) Green pixels outnumber blue and red pixels by a factor of two. This bias towards sampling the green pixels comes from the fact that our eyes have their best sensitivity to green.

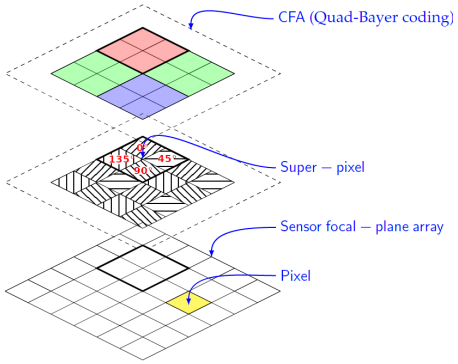

Figure 3.9: The Quad-Bayer filter in the RGB Polar sensor.
Source: [23]

Many would at this point assume that there must be three or four times as many pixels in on the CCD to make this work. For example, if we were to take a small 2x2 area, we would have one red, two green, and one blue samples. Combine these into a single pixel that is twice as big in each direction and you have a single pixel that has full-color data – measures of red, green, and blue for this single, larger pixel. While quite simple, this is not what happens.
In fact, if the monochrome version of a chip has 1024 x 768 pixels, the color version has 1024 x 768 pixels as well and the color image you see has 1024 x 768 pixels. Each pixel has red, green, and blue values assigned to it even though each native pixel had filters that only measured red, green, or blue data.

The process by which this image gets decoded from a color "mosaic" into a full-

resolution color image is called "debayering". There are many ways of reconstructing the color image, ranging from the simple to the exceedingly complex. Some work very poorly, but some work exceptionally well. It is good to keep in mind that in general there is a trade-off between speed and accuracy. If you need an image quickly, the reconstruction of the image will likely be less accurate than if you allow yourself the time and computational resources to perform a more sophisticated reconstruction of the image. This is why webcams that must stream images at 30 frames per second or even digital still cameras (whose users do not want to wait many seconds between snapshots) often produce images that suffer from color artifacts.

That said, all debayering techniques involve interpolation – or the estimation of missing values based on surrounding, known values. Interpolation is an educated guess as to what a missing value should be and it is just that – a guess. But, some guesses can be quite accurate.

The debayering of the RGB Polar sensor can yield 20 representations or RAW data (without calculations like DOLP) like so:

Channel / Angle	RGB	R	G	B
0°	$F_{0°}^{clr}$	$F_{0°}^{red}$	$F_{0°}^{green}$	$F_{0°}^{blue}$
45°	$F_{45°}^{clr}$	$F_{45°}^{red}$	$F_{45°}^{green}$	$F_{45°}^{blue}$
90°	$F_{90°}^{clr}$	$F_{90°}^{red}$	$F_{90°}^{green}$	$F_{90°}^{blue}$
135°	$F_{135°}^{clr}$	$F_{135°}^{red}$	$F_{135°}^{green}$	$F_{135°}^{blue}$

Table 3.2: Representations of the RGB Polar sensor.

Crosstalk Elimination

From a cost-effective perspective, color sensors using CMOS technology and a Bayer filter are a preferred choice. In this section, we describe the different crosstalk phenomena, which occur on this type of sensors as well as their possible consequences during the holographic reconstruction. The term "crosstalk" refers to the undesirable effects that occur when a signal transmitted on a channel modifies or impacts the signals transmitted on the other channels. This global phenomenon leads to a reduction in sensitivity, poor separation of colors and a degradation of spatial and frequency resolution. The main crosstalk phenomena appearing on color sensors are spectral, optical, electronic and for our application polarization. We provide below a brief description of each of these phenomena, focusing on how to quantify and reduce them.

Spectral crosstalk: CMOS sensors classically used in a costeffective lensless color microscopy scheme often do not allow trichromatic information to be obtained at each photodetector. Consequently, the photodetectors are covered by a matrix of chromatic filters called "Bayer color filter array", which filters the incident light by transmitting only one of the three primary components at each pixel. Spectral crosstalk is due to the Bayer filter covering the photodetector layer of the CMOS color sensors: their spectral responses are not ideal bandpass.

Optical crosstalk: Optical crosstalk occurs when the incident angle becomes too large

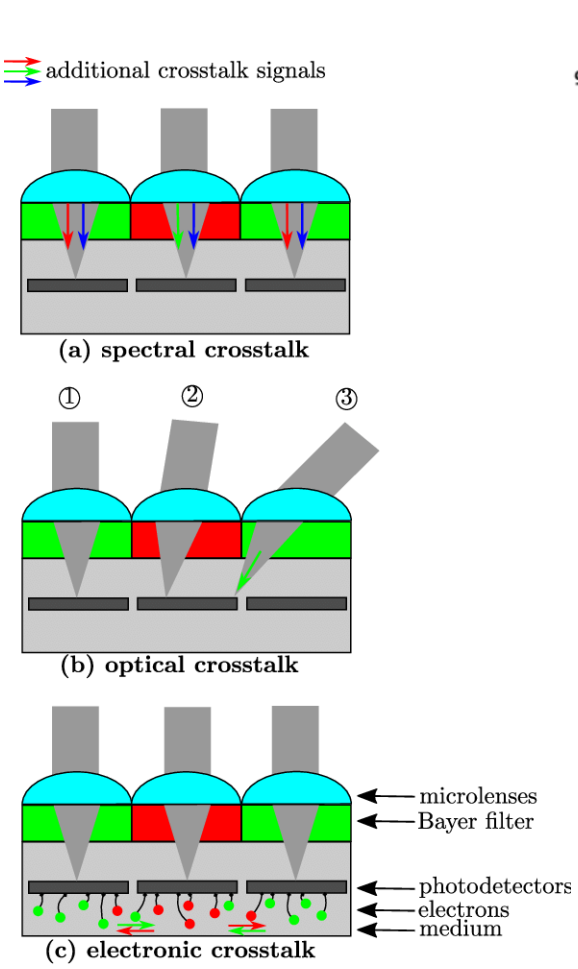

(a) Optical crosstalk.
Source: [24]

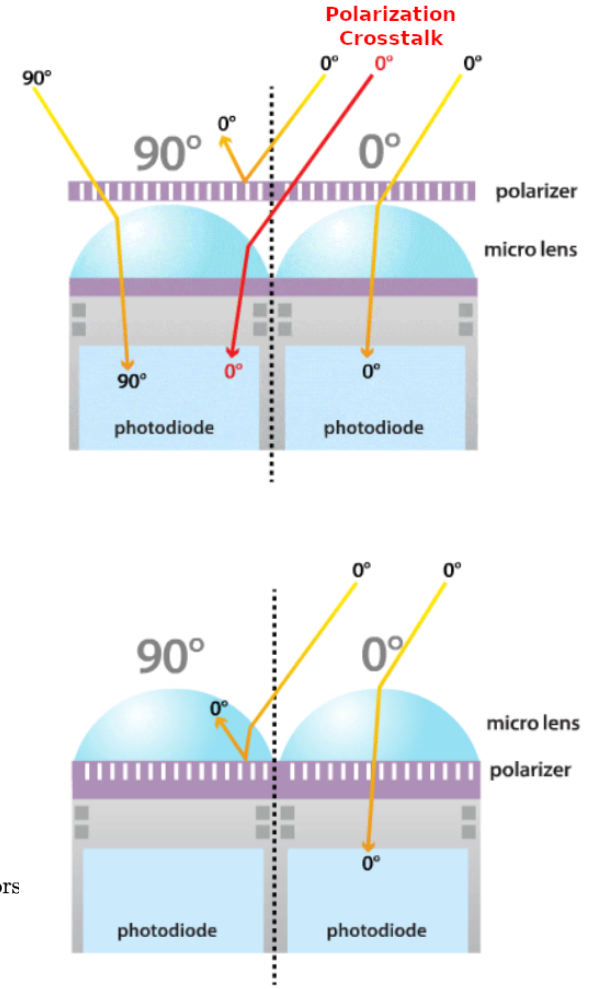

(b) Polarization crosstalk.
Source: thinklucid.com

Figure 3.10: Different cases of crosstalk.

for the microlens array to focus light on the photodetector immediately below. In this case, a portion of the signal of interest may be lost in the gap that separates two adjacent photodetectors or, worse, may impact a neighboring photodetector. Figure 3.10a illustrates this phenomenon. No optical crosstalk occurs at null or weak incidence angles [cases (b)① and (b)②]. At higher incidence angles [case (b)③], optical crosstalk can occur.

Electronic crosstalk: Electronic crosstalk occurs due to an interaction between signals received at two neighboring photodetectors. Some electrons created as a result of detection of light in the depletion zone are diffused to adjacent photodetectors. This results in an additional error in the signal of interest as illustrated in Figure 3.10a [case (c)].

Polarization crosstalk: Optical crosstalk occurs when the incident angle becomes too large for the microlens array to focus light on the photodetector immediately below. It is similar to optical crosstalk and may occur when the micropolarization filters are plased on top of the microlens of the sensor. The signal of interest may be lost in the gap that separates two adjacent photodetectors or, worse, may impact a neighboring photodetector. Figure 3.10b illustrates this phenomenon and how to avoid it as proposed by *Sony Semiconductor Solutions Group*.

Triple bandpass filter

Since polarization and optical crosstalk is minimized by design of the proposed sensor, there is a need to further address the issue of spectral crosstalk. Introducing a triple bandpass filter to the optical design, gives an extra protection layer to the spectral crosstalk phenomenon. Figure 3.11a illustrates the quantum efficiency of the proposed sensor with respect to the wavelength. Figure 3.11b illustrates the proposed bandpass filter that optically blocks the critical crosstalk spectra and thus eliminating the possibilities of false measurement.

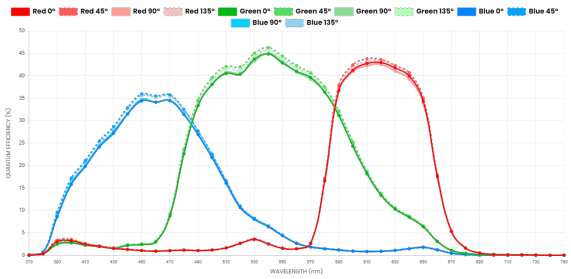

(a) The Quantum Efficiency (QE) of our RGB polarization sensor.

Source: thinklucid.com

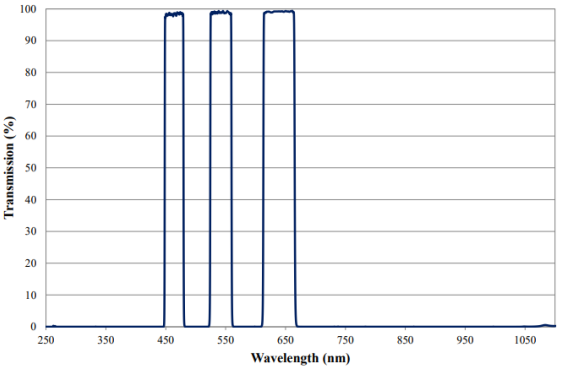

(b) Triple bandpass filter for spectral crosstalk elimination.

Source: edmundoptics.com

3.3.2 Software Segmentation

Since HTS instrumentation is mainly focused in research facilities, in order to have a marketable device it is important to aim not only in automatic data acquisition, but also in the **user friendliness** and manual inspection. For that reason, the device should support both auto and manual acquisition modes.

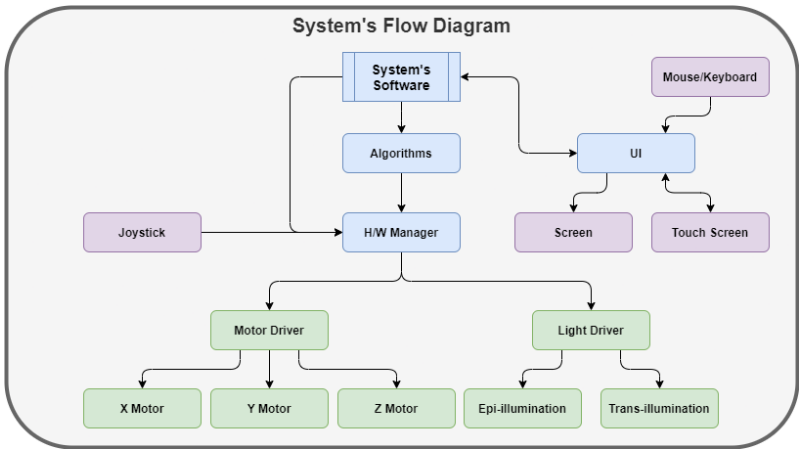

Figure 3.12: System's Block Diagram.

In the **automatic scan**, the user should select a Region Of Interest (ROI) and define the acquisition parameters. The motorized X-Y-Z translators should then move to the specified area and acquire in-focus images for each frame. The lights and camera drivers should also be precisely timed when acquiring different modalities. The resulting frames should be stitched together in order to create a grid-like overview image.

In the **manual scan**, the user should be able to move the motorized stage either from a Graphical User Interface (GUI) or from a physical joystick. Of course, not all modalities can be viewed simultaneously in manual mode, so when the user selects a modality from the GUI, then the software must be responsible to change light and camera settings from predefined and calibrated values.

Furthermore the system should implement inter-connectivity through the internet and provide online database solutions in order to broaden the sample diversity and be able to support the integration of reinforcement learning analysis on late stages of commercialization. Beside being a powerful commercialization strategy, having an all in one solution of a scientific microscope and an Internet Of Things (IOT) concept is something that the needs of our time push manufacturers to be challenged with and clients to require.

Comparing results and creating ground truth feature spaces for new samples is essential for HTS. Our device must have **self-calibration** procedures so that the operator is sure that data gathering was performed correctly and without artifacts.

The diagram of Figure 3.13 presents the fundamental structure of the software of our system. We separately worked into the back end and front end by utilizing some generic interfaces. In terms of height, we observed the system's levels of operation from low to high. In our research, we got involved to several fundamental structures of this software in order to enable the use of the extra polarization module. A brief description of these structures is presented.

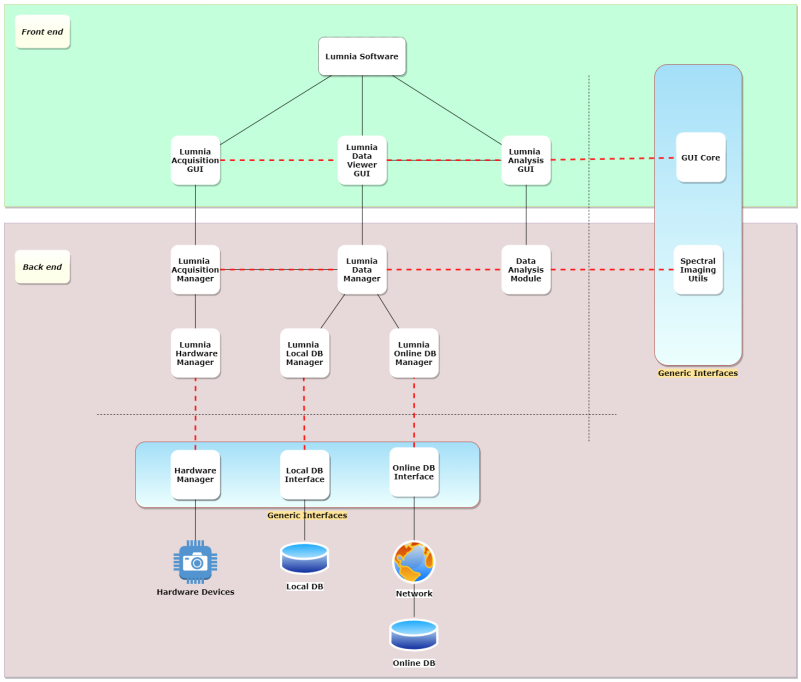

Figure 3.13: Software Functional Block Diagram.

- **Lumnia Hardware Manager**

  The hardware manager unit of the system provides all the low level mechanisms to communicate and control the various hardware components (motors, cameras, light sources, encoders and joysticks). The system recognizes the connected devices and builds up the utilities and software associated with them. Also, this unit provides the ability of utilizing x-y-z motors, encoders, joysticks and the GPU of the system for image capturing and processing. Each hardware device has to be treated separately from the system, because it has its own way of communication and timing. For these reasons a separate driver for each device is created, so mid level access to the hardware components is now available. For our module new camera drivers and GPU firmware binaries were developed in order to utilize the unique debayering and real-time mapping calculations.

- **Lumnia Acquisition Manager**

  This manager, uses the mid level hardware access provided from the Hardware Manager to construct the specific acquisition techniques the microscope will implement. This unit can perform multi spectral and/or hyper spectral imaging, auto focusing acquisition, stitching acquisition and much more. While in these acquisitions, structures of data and images that delineate each case are created. In every capturing occasion, the output structure of this unit will be a fully described object for universal usage. This unit will utilize algorithms specifically designed either to measure application specific image characteristics or to produce real time data providing feedback to the hardware manager's controllers. By optimizing the processing of the data on the system's GPU, it is very efficient in calculating all the needed results for the sample's examination and system functionality.

- **Lumnia Data Manager**

This module, is responsible for all data flow throughout the microscope and acts like a supervisor. It is responsible for handling multi image sets, that contain different image modalities and are either frames or overviews of a selected ROI, by passing them to the viewers, saving them to the disk and local database, or syncing through the online database. It also acts as a credential manager and provides user access rights to separate the level of interaction. This way operators who need an engineering-level interface can have access to these functions. Whereas, basic operators will have access to a simplified interface. Lastly, this module is utilized to attach external files and analysis results to a specified data set. This enables operators to enrich the database (DB) with features obtained with different means of measuring.

- **High Level Functionality**

  The high level functionality of the system provides a wide variety of procedures that the system is capable of executing. By utilizing all the lower level software units, the system creates functions that combines them into complex and very useful software structures. These structures are the core of the system's functionality, as they can handle any occasion and task needed. Finally, their resources are already managed and optimized from the lower level designs so that the system offers a smooth real time experience.

- **Graphical User Interface (GUI)**

  The graphical user interface provides the ease of using a complex machine with simple and understandable structure and appealing appearance. It is always of great importance when designing a system, to work properly not only for users that always know how to use it and interact with it, but also for users that specialize in other scientific fields and can appreciate the machine's outcome from another perspective. That's why a well designed graphical user interface is essential for our system and should be user friendly and intuitive.

In conclusion, this system intents to give the specialists the ability to use a machine capable of executing all the tasks a classic microscope could execute, but at the same time with the ease of speed, accuracy, repeatability, data management and automation without the human surveillance. Reading and loading the microscope's examinations from captured images, within microscope's software, setting up the system in the exact same configuration as when an image was captured and a lot of interesting characteristics are essential.

Chapter 4

Results

4.1 Introduction

So far, we have discussed the need of fast data gathering and analysis that HTS devices specify. We have seen the fundamental physics of polarized light and how different crystalline structures of materials affect the optical property "birefringence". Through a state of art analysis we have shown that no device performs birefringence or retardance measurements in **real-time**, being rottation independent, and acknowledged the need of such instrumentation, especially in High Throughput Screening (HTS) applications.

We then defined the desired ellipsometry that our optical module will provide and how our Polarization State Generator (PSG) and Polarization State Detector (PSD) will be integrated to the Multi Modal (MM) High Throughput Screening (HTS) microscope. We have admit a camera sensor that fits our needs and assured real time stokes parameters measurement.

We have talked about the Multi Modal Feature Space (MMFS) and its contribution to a unique and complete description of the chemical properties of any material and its non-destructive nature of measurement. Furthermore we have discussed about the need of self-calibration in order to have consistency in the feature spaces of the materials. We have then introduced the existing software structure and how to insert a new modality to the microscope, alongside with new and useful features like real-time analysis results.

In this chapter we, first and foremost, will discuss our apparatus calibration procedures, covering spectral spatial and retardation cases. For retardation measurements we will compare a variety of methods until presenting the proposed calibration one. We will present the results of our research through GUI screenshots and comparisons, illustrating the difference of seemingly similar samples. Lastly, a novel MMFS classification technique that depends on the generated birefringence map will be demonstrated.

4.2 Calibration

4.2.1 Mechatronics and Camera calibration

Every instrumentation needs proper calibration. We first of all need to self-calibrate the X-Y-Z translators and assure that upon every startup the mechatronics of the system work properly. We then need to self-calibrate every imaging modality based on a calibration target and fine tune the camera sensors to converge on predefined intensity values.

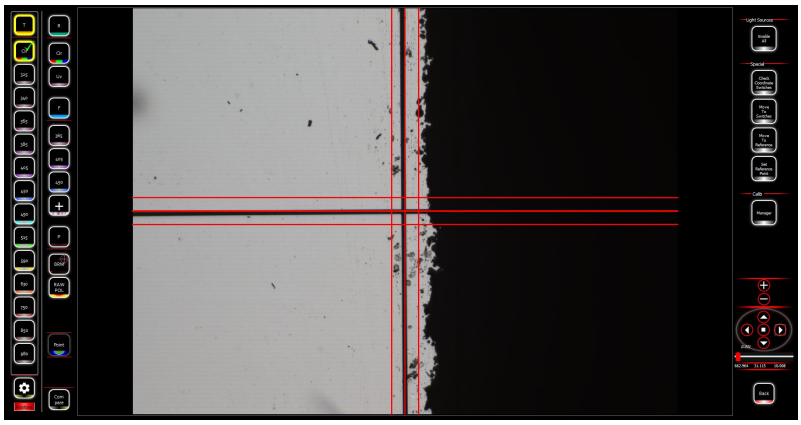

Figure 4.1: The system's calibration target.

When the device finishes initialization, a known calibration target which is placed on the edge of the moving stage and is shown on Figure 4.1 assures that the motors moved the stage within tunable limits. This assertion is performed automatically through image processing and pattern recognition algorithms. If it fails then the user is informed and no data acquisition can be performed until the issue is resolved.

On the left side of the cross, the calibration target is transparent. This side is used to auto calibrate the Transmission and Polarization imaging modalities. The calibration algorithm initially tries to converge to the target intensity through changes on the sensor exposure time (in μs) and analog gain (in %) The user can select the desired imaging modalities to calibrate and start the auto calibration procedure. If everything converged, then the user can accept the new settings or decline. If some modality did not converge, then the algorithm is responsible to change the light source intensity. This is performed through the Ethernet ESP controller that were presented on the previous chapter.
On the right side of the cross, the calibration target is opaque and colored with a fluorescent white paint. This side is used to auto calibrate the Reflection and Fluorescent imaging modalities. The procedure is similar to the Transmission and Reflection calibration.

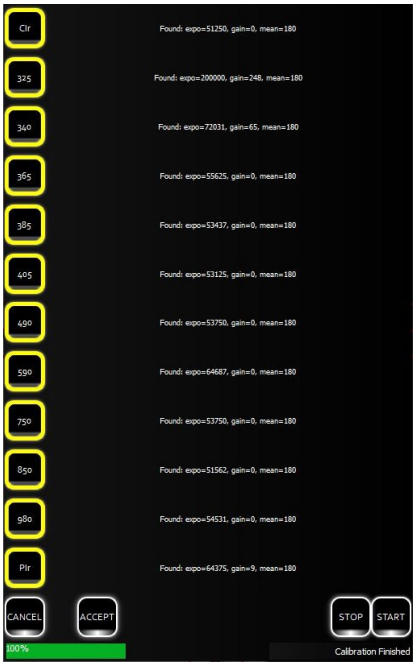

Figure 4.2: The auto-calibration GUI for tuning the camera sensors to predefined intensities.

For Reflection imaging we need to have a balanced white reflection from the target and

so the sensors need to be calibrated homogeneously in every channel. For Fluorescent imaging we have measured the emission spectrum of that paint with and spectrometer. This spectrum is in the 400-470 nm range and so the sensor's channels cannot be homogeneously calibrated in order to see a blue fluorescence. These values are predefined by the manufacturer and if not met then the user is informed through a message on the screen.

After the self calibration procedure finishes and all imaging modalities are calibrated, the user can capture a full data set on the calibration target and assure a 1) flat spectrum, 2) nice reflections, 3) blue fluorescent colors and 4) black background on the polarization modality. This is shown in Figure 4.3 where the GUI is on the **Frame View** page, where the user can perform spectrum and color measurements.

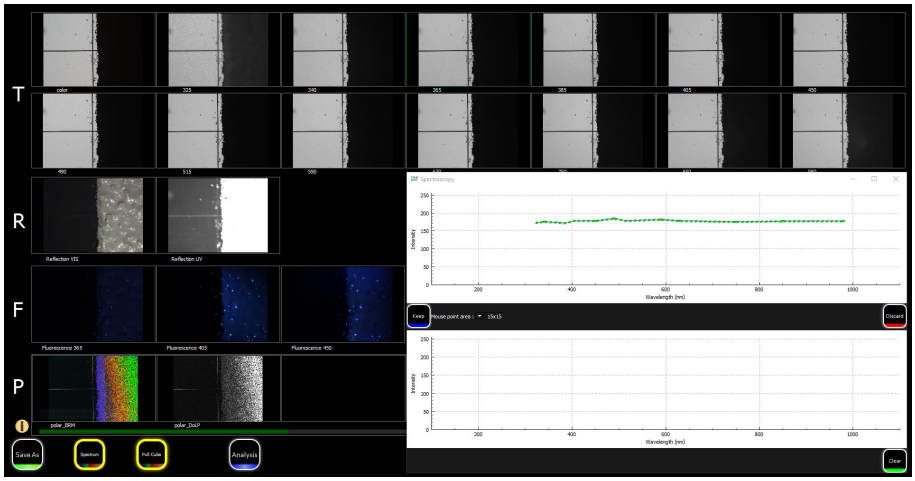

Figure 4.3: A full data-set captured on the calibration target. Transmission spectra are depicted.

Having a bundle of useful polarization data is nice, but in order to be interpreted in real time we need to compose a lookup table like procedure. This will result in interpreting the data in a **rotation independent** manner and yield accurate retardance measurements. This means that a material of a specified retardance x nm capture at an arbitrary angle $\theta°$ will also yield the same retardance measurement x nm if captured at another angle $\phi°$.

In order to self-calibrate in such rotation independent manner, the use of a variable retarder takes place. This device, as its name suggests, has variable retardance depending on the operation voltage and can be the ground truth for our measurements.

4.2.2 Variable Retarder principle of operation

As shown in Figure 4.4, the Liquid Crystal (LC) Retarder is a transparent cell filled with a solution of liquid crystal. The parallel inner faces of the cell wall are coated with a transparent conductive film so that a voltage can be applied across the cell. In the absence of an applied voltage, liquid crystal molecules have an ordered orientation, which is determined by the alignment layer that is created by the organic polyimide (PI) coating and rubbing angle. The orientation, together with the stretched shape of the molecules, creates an optical anisotropy. Thus birefringence is formed across the cell and creates retardance. The total retardance in wavenumbers can be calculated by the Equation 2.4.4.2 ($\delta = \frac{2\pi t \Delta n}{\lambda}$), where here t is the cell gap size; λ is the wavelength; Δn is the difference in the refractive index between the parallel and perpendicular polarization directions.

When an electric field is applied, the molecules will align to the field and the level of birefringence is controlled by the tilting of the LC molecules. Hence, the phase offset in a

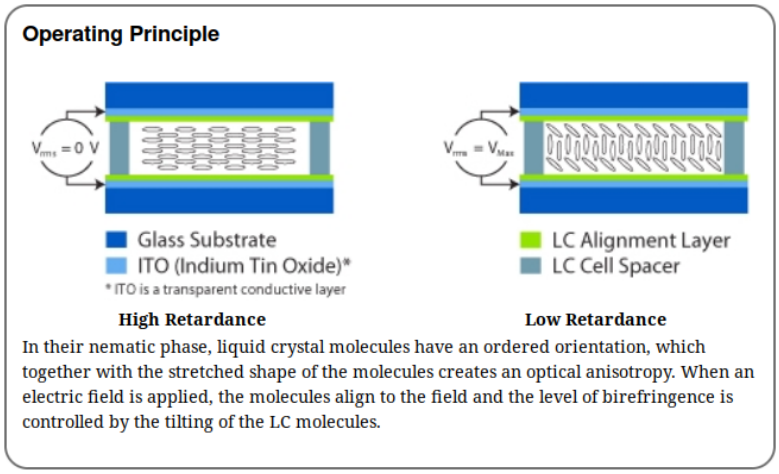

Figure 4.4: Variable Retarder principle of operation.
Source: thorlabs.com

linearly polarized beam of light can be actively controlled by varying the applied voltage. When maximum voltage is reached, the LC molecule will then align to the direction of the incidence beam and the cell will become isotropic.

4.2.3 Calibration procedure

The variable retarder defines its Optical Axis and we can move our microscope stage on its center. We then can align its OA to be parallel with our 0° capture channel and then gradually start measuring the relations of all RGB angles while gradually increase the retardance. This yields a graph as shown in Figure 4.5.

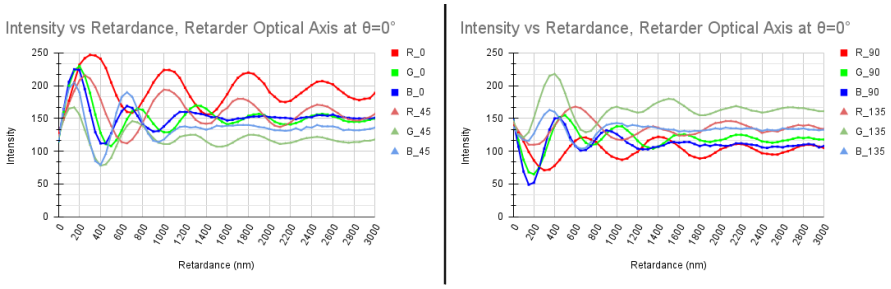

Figure 4.5: Intensity vs Retardance, while aligning the retarder's Optical Axis at $\theta = 0°$ (parallel with our 0° sensor). The RGB channels of 0°, 45°, 90° and 135° are shown.

We can repeat this procedure for every angle $0° \leq \theta \leq 180°$ and measure all relationships of the intensities in order to have a lookup table. We can then provide this table to the GPU to yield real-time retardance matches. This compensates the phase shift effect and can be rotation independent.

We can observe that the closest angles pairs $0° - 45°$ (Figure 4.5 left) and $90° - 135°$ (Figure 4.5 right) are in phase while the polarization ellipse introduces an in-phase $\Delta\phi$ as shown in the peaks of tha wave curves. We can also see that the total RGB intensity averages on a specific value (180°) one pair is maximized, the other is minimized. Those imply that the polarization ellipse is periodically stretched and withdrawed.

4.2.4 Finding Optimal Retardance Classification

Initially the research involved complex machine learning algorithms that could, based on the collected data, correctly classify the retardance value based on the intensity measurements described on Table 2.1 and depicted in Figure 4.5. For that reason we used the *"WEKA Software"* ([27]) and a various collection of rule, tree and function based classifiers was used.

Linear Regression and SMOreg

In machine learning, support-vector machines (SVMs) are supervised learning models with associated learning algorithms that analyze data for classification and regression analysis. Given a set of training examples, each marked as belonging to one of two categories, an SVM training algorithm builds a model that assigns new examples to one category or the other, making it a non-probabilistic binary linear classifier.

In statistics, linear regression is a linear approach for modelling the relationship between a scalar response and one or more explanatory variables. The case of one explanatory variable is called simple linear regression; for more than one, the process is called multiple linear regression. This term is distinct from multivariate linear regression, where multiple correlated dependent variables are predicted, rather than a single scalar variable.

Linear Regression Cross-validation Summary	
Correlation coefficient	0.285
Mean absolute error	947.3747
Root mean squared error	1121.7757
Relative absolute error	93.5257 %
Root relative squared error	95.9104 %

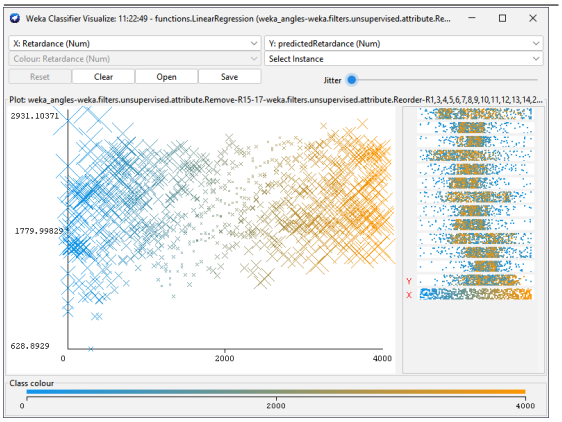

Figure 4.6: Linear Regression Classifier Errors. Actual retardance (x axis) vs predicted Retardance (y axis).

Table 4.1: Linear Regression Cross-validation Errors.

In linear regression, the relationships are modeled using linear predictor functions whose unknown model parameters are estimated from the training data. In our case the training data were all curves acquired with the retarders OA $0° \leq \theta \leq 180°$. Those values had a correlated Retardance (nm) label and we composed a linear regression model through the full training set. We then performed a 10-fold cross-validation to test the accuracy of the model. The confusion scatter of the first fold is depicted in Figure 4.6, on the left, and the summary of the cross validation is also shown. We can see that the correlation coefficient is very low. This means that the predicted retardance varies a lot from the actual retardance. If the correlation coefficient was close to unit, then the scatter plot would have a linear form and the predicted retardances would match the actual ones.

Sequential minimal optimization (SMO) is an algorithm for solving the quadratic programming (QP) problem that arises during the training of support-vector machines (SVM). Support-vector machines (SVM) is an elegant tool for solving pattern recognition and regression problems. Over the past few years, it has attracted a lot of researchers from the neural network and mathematical programming community; the main reason for this being its ability to provide excellent generalization performance. SVMs have also been demonstrated to be valuable for several real-world applications. The SMOreg algorithm ([28]) provides a much better regression compared to the linear regression and this can be validated by the increased correlation coefficient. Although it does not perform correct guesses for the low and high retardance range. This suggests that our data are not linear and such regression models cannot classify retardance adequately.

SMOreg Cross-validation Summary	
Correlation coefficient	0.5121
Mean absolute error	834.1104
Root mean squared error	1009.0812
Relative absolute error	82.3441 %
Root relative squared error	86.2751 %

Table 4.2: SMOreg Cross-validation Errors.

Figure 4.7: SMOreg Classifier Errors. Actual retardance (x axis) vs predicted Retardance (y axis).

Those results suggest that Regression models are not suitable for our case and we need to seek other methodologies for classification.

Random Tree and Random Forest

In mathematics, a random minimum spanning tree may be formed by assigning random weights from some distribution to the edges of an undirected graph, and then constructing the minimum spanning tree of the graph. Random forests or random decision forests is an ensemble learning method for classification, regression and other tasks that operates by constructing a multitude of decision trees at training time. For classification tasks, the output of the random forest is the class selected by most trees. For regression tasks, the mean or average prediction of the individual trees is returned. Random decision forests correct for decision trees' habit of overfitting to their training set.

Random Tree Cross-validation Summary	
Correlation coefficient	0.8452
Mean absolute error	435.3788
Root mean squared error	654.5505
Relative absolute error	42.981 %
Root relative squared error	55.9632 %

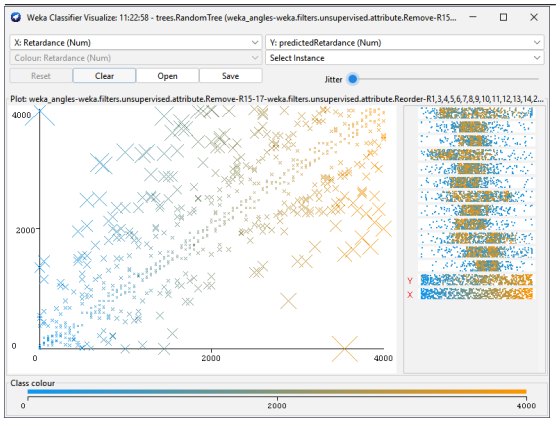

Figure 4.8: Random Tree Classifier Errors. Actual retardance (x axis) vs predicted Retardance (y axis).

Table 4.3: Random Tree Cross-validation Errors.

The random tree implementation yielded a decision tree with a size of 1049 nodes and an option to allow estimation of class probabilities based on a hold-out set (backfitting) was enabled. The results of that approach were good while training (Relative absolute error of $\sim$ 22%), but when performed a a 10-fold cross-validation by suffling the data set this percentage nearly doubled. Although it is clear from Figure 4.8 that there are a lot of useful predictions (indicated by the linear line from the bottom left to the top right corner of the scatter), the variation is big. We have some guesses of actual retardance close to 4000 be predicted to zero. The way of compensationg this variation is not yet clear, but the Random Tree algorithm may be a good candidate for our problem if optimized.

The Random Forest classifier constructs a forest of random trees. For classification tasks, the output of the random forest is the class selected by most trees. Random decision forests correct for decision trees' habit of overfitting to their training set. Even though we did not observe overfitting phenomena in our Random Tree implementation, we do observe a better, less-variated and linear behavior in the classification 10-fold cross-validation test case. With optimization this algorithm could also be used and utilized. What held us back from investing in it is the fact that the prediction to actual retardance function is not an injective one and the relation is not $1-1$. We can see that while the x axis spans from 0 to 4000nm, the y axis spans from ~ 157 to ~ 3726.

Random Forest Cross-validation Summary	
Correlation coefficient	0.9324
Mean absolute error	323.2652
Root mean squared error	440.0977
Relative absolute error	31.913 %
Root relative squared error	37.6278 %

Figure 4.9: Random Forest Classifier Errors. Actual retardance (x axis) vs predicted Retardance (y axis).

Table 4.4: Random Forest Cross-validation Errors.

Decision Table and M5Rules

Decision tables are a concise visual representation for specifying which actions to perform depending on given conditions. They are algorithms whose output is a set of actions.

The information expressed in decision tables could also be represented as decision trees or in a programming language as a series of if-then-else and switch-case statements. In our case the input conditions are a set of RGB values and the output is a set of retardation measurements. We initially except the deterministic nature of decision tables to match our problem, but as we can see the automatic training of them is counter intuitive.

Decision Table Cross-validation Summary	
Correlation coefficient	0.641
Mean absolute error	713.1342
Root mean squared error	901.219
Relative absolute error	70.4012 %
Root relative squared error	77.053 %

Figure 4.10: Decision Table Classifier Errors. Actual retardance (x axis) vs predicted Retardance (y axis).

Table 4.5: Decision Table Cross-validation Errors.

On Figure 4.10 on the left we can clearly see that the corvariance of the predicted and actual values is bigger than expected. As described in [29], decision tables are a hypothesis space for supervised learning algorithms. Decision tables are one of the simplest hypothesis spaces possible, and usually they are easy to understand. As part of the automated construction of the model, 73 rules were created with best first criteria in mind and a stale state was achieved after 5 node expansions. The total number of subsets evaluated was 72 and the metric of best subset found was 859. Indeed, the correlation coefficient was better that the regression models, but a the big relative absolute error is depicted by the graph not following a straight, diagonal from bottom left to top right, line. This means that this algorithm still needs optimization.

Model trees —- decision trees with linear models at the leaf nodes -— have recently emerged as an accurate method for numeric prediction that produces understandable models. However, it is known that decision lists (ordered sets of If-Then rules) have the potential to be more compact and therefore more understandable than their tree counterparts. This combines linear regression with the decision table algorithm and is described in [30]. An example of our use case would be *IF R_90 ≤ 153.5 AND G_0 > 115, THEN RETARDANCE = {a linear regression formula}*. The M5 pruned model (using smoothed linear models) yielded a total of 14 rules by automatic training. A linear behavior is observed and a good correlation coefficient is achieved. Al though this classification scheme seems promising, a better and more restricted regression model at the outcome of every rule needs to be developed because the linear nature of regression gives, sometimes, negative or out of range retardance predictions.

M5Rules Cross-validation Summary	
Correlation coefficient	0.7766
Mean absolute error	562.7901
Root mean squared error	736.8864
Relative absolute error	55.5591 %
Root relative squared error	63.0028 %

Figure 4.11: M5Rules Classifier Errors. Actual retardance (x axis) vs predicted Retardance (y axis).

Table 4.6: M5Rules Cross-validation Errors.

KStar

KStar Cross-validation Summary	
Correlation coefficient	0.8663
Mean absolute error	388.8618
Root mean squared error	650.9168
Relative absolute error	38.3888 %
Root relative squared error	55.6525 %

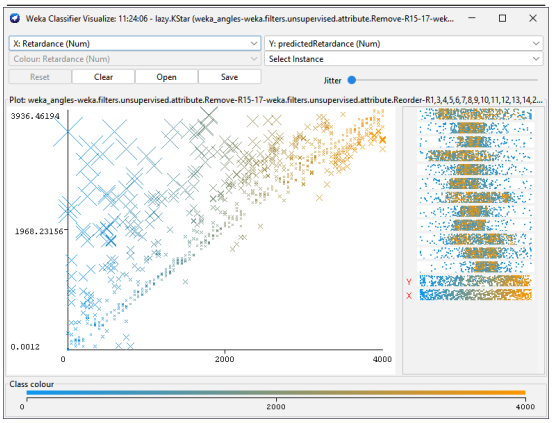

Figure 4.12: KStar Classifier Errors. Actual retardance (x axis) vs predicted Retardance (y axis).

Table 4.7: KStar Cross-validation Errors.

The use of entropy as a distance measure has several benefits. Amongst other things it provides a consistent approach to handling of symbolic attributes, real valued attributes and missing values. The approach of taking all possible transformation paths is discussed. K* [32], an instance-based learner which uses such a measure, and results are presented which compare favourably with several machine learning algorithms. For such interpretation, we need to define the RGB value triplets of each angle as sequences. The key point here is to note that it is possible to associate a probability with each sequence. If the complexity (length) is measured in bits is c then the appropriate probability is 2^{-c}. In particular, it is true that in any well defined distance based on Kolmogorov complexity the sum of this probability over all transformations will satisfy the Kraft inequality: $\sum 2^{-c} \leq 1$.

The distance between instances it is the probability that an instance will be arrived at by doing a random walk away from the original instance. After summing over all paths

this probability can be transformed into units of complexity by taking the logarithm. This algorithm is successfully used to identify distance between sequences of DNA.

For our use case we modified it to be used with numeric sequences instead of symbolic and yielded the results of Figure 4.12 that show a good minimum boundary, but a bigger variance for values bigger than the supremum of the desired linear function. From such distance measure interpretation of the data, we saw that a good correlation coefficient was achieved but the implementation of such algorithm on the GPU would be time consuming and the fine tune of the algorithm would also be difficult. For that reason we tried the idea of calculating **euclidean distances** (instead of entropic) of RGB values.

4.2.5 Proposed Prediction Algorithm

Triplet Euclidean Distance Metric

All methods above aim for dimensionality reduction which is not obligatory for our case since the data gathering performed from the calibration can be available for real-time measurements in the GPU module.

For the development of our retardance prediction algorithm, we have available RGB triplets for every angle in the polarization ellipse as shown in Figure 4.13. Ideally, in order to be rotation independent, the rotation of the ellipse (keeping the axis stable) must yield the same retardance measurements. So what we need to look for is the relationship of the RGB intensities between the four polarization angles. This means that providing the four angles of the measurements and the four labeled angles registered on the lookup table, we need to minimize the euclidean distance of the four measured triplets compared to the lookup table shuffled.

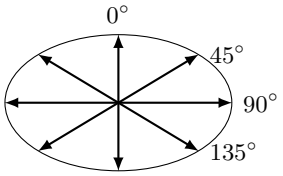

Figure 4.13: Polarization Ellipse.

To do so, we have some measured RGB intensities and one registered to compare every angle. As shown in Table 4.8 we do not calculate arbitrary samples, but in contrary we maintain the neighbor order by "rolling" through them. This gives us four distance metrics, $d_\bullet$, $d_\star$, $d_\diamond$ and $d_\dagger$ each one representing the euclidean distance from each formation. The actual distance D to compare is defined as $D = \min(d_\bullet, d_\star, d_\diamond, d_\dagger)$ and yields the best found distance between all possible formations.

Measured \ Registered	F_{0°	F_{45°	F_{90°	F_{135°
F_{0°	$\bullet$	$\star$	$\diamond$	$\dagger$
F_{45°	$\dagger$	$\bullet$	$\star$	$\diamond$
F_{90°	$\diamond$	$\dagger$	$\bullet$	$\star$
F_{135°	$\star$	$\diamond$	$\dagger$	$\bullet$

Table 4.8: Measured vs Registered Retardance Triplet Comparison. We want to allow rotation of the axis but not mixtures, so the cases of $\bullet$, $\star$, $\diamond$ and $\dagger$ are compared.

The proposed algorithm for computing the best retardance match is shown below:

Input : $A = [\ ]$, a non empty list of labeled retardance measurements.
Input : S, an valid, unlabeled retardance measurement.
Output: A labeled retardance measurement.
$d \leftarrow \max$
$tmpM \leftarrow S$
for $i \leftarrow 0$ **to** $\texttt{size}(A) - 1$ **do**
  if $D(S, A[i]) \leq d$ **then**
    $d \leftarrow D(S, A)$
    $tmpM.label \leftarrow A[i].label$
  end
end
return $tmpM$

Algorithm 1: Find best retardance match from a lookup set A

Where $D(S, A[i])$ is the minimum distance D 4.2.5, as described in Table 4.8.

We thus only need to keep in computer's memory a small amount of measurements and this estimation can be performed in real time on the GPU upon the debayering procedure in order to yield **per-pixel retardance measuremens**.

From the above calibration we yield in **real-time** a pseudo color image that follows the Michel-Levy 2.5.3 chart principle. The value ranges of this image are shown in Figure 4.14.

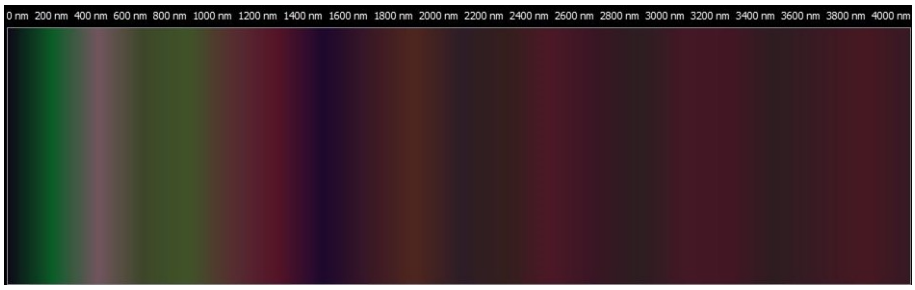

Figure 4.14: Retardance Pseudocolor Mapping lookup table that follows the Michel-Levy principle.

This color mapping can be used not only to have retardance measurements but also, combined with our **Analysis toolkit** and the accurate morphological measurements, yield birefringence values through the aforementioned Equation 2.4.4.2 and the calculated thickness.

4.3 Measurements

The system is equipped with a Joystick with buttons. A Joystick and some buttons are used to interact with the motorized system. This is very important as the feel of the joystick does not require any skill to understand and it is subconsciously associated with the motorized motion. This is the main user interface when someone is navigating using **manual mode**. In this mode all imaging modalities are available to observe the samples.

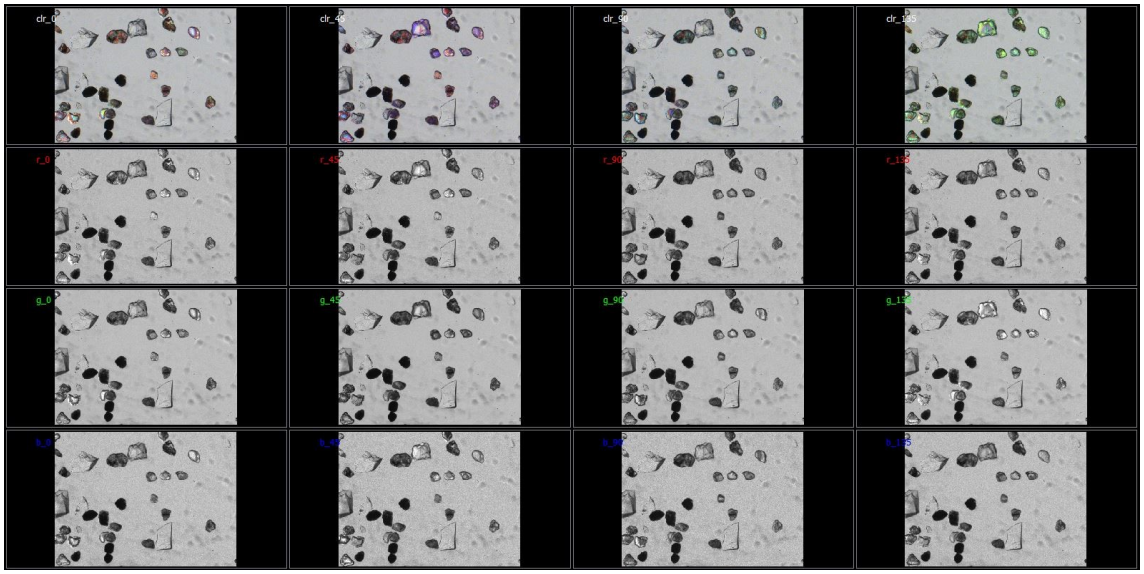

Figure 4.15: Raw polarization images, as introduced on the system design and discussed on Table 3.2.

Figure 4.15 show the RAW polarization images acquired by the polarization module. On the top row we see the color image for every angle of polarization. The three rows below them are the red, green and blue channels of the color images. All those are shown in real time and the operator can see all the polarization features like the interference colors.

The annotated samples in Figure 4.16 shows that even if at some angle two samples can seem extremely similar, we can in fact be sure that their crystalline structure differs when comparing them at every polarization angle. This implies that the polarization data do in fact provide useful information and an **extra dimensionality** for the Multi Modal Feature Space.

The sample shown in Figure 4.16 is carefully prepared with controlled conditions in our laboratory and contains only human hair, "leaded glass", which is potassium silicate glass which has been impregnated with a small amount of lead oxide in its fabrication and "quartz sand", which is very similar to glass due to its composition being mainly silicon dioxide (SiO_2). As we see in Figure 4.17, Quartz has well defined crystalline structure and is *anisotropic* thus provides retardation values. On the contrary, silica glass is *isotropic* and no birefringence property is observed.

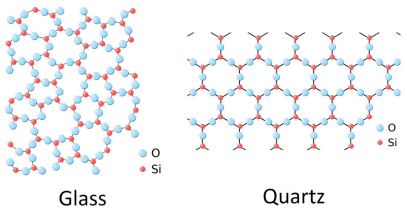

Figure 4.17: Atomic-level representations of glass (silica) and quartz.
Source: visionlearning.com

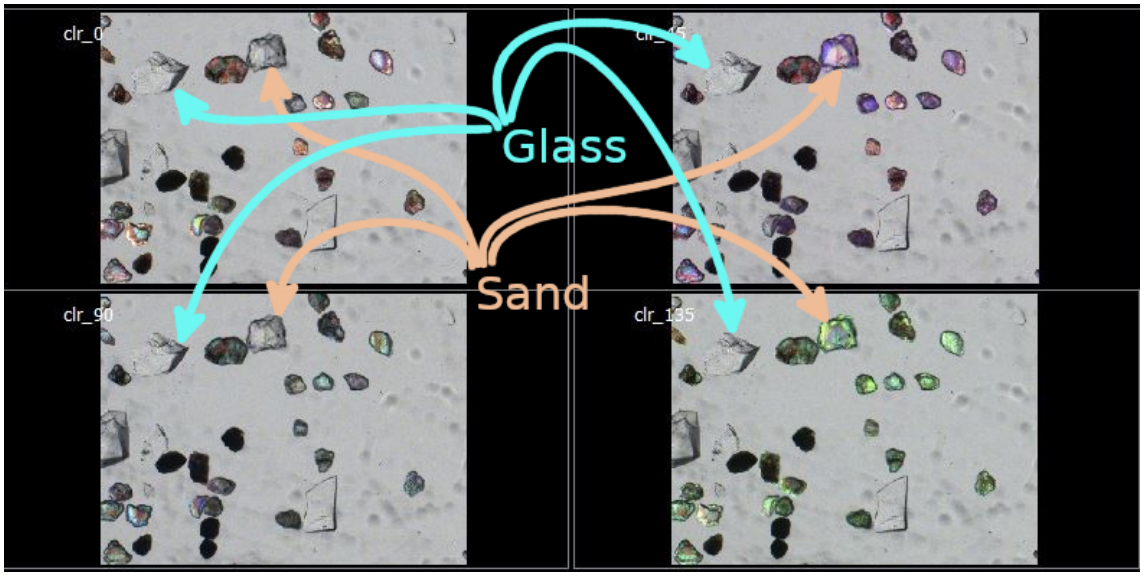

Figure 4.16: Color polarization images. Here we see birefringent materials having a lot of interference colors while non birefringent materials being homogeneous for every polarization angle.

Overview Viewer The look and feel of the overview viewer is organized in a four column structure. Every column is assigned for each imaging modality and provides its own control buttons. From left to right we have:

- **Transmission**

  This viewer depicts all images acquired in the Transmission imaging modality. On its right side has control buttons that change between the color image and the Hyper Spectral bands. The available wavelengths span from the Ultra Violet (300 nm) up to the Near Infrared (980 nm). It is pre-calibrated to have a background intensity value of 180 for each wavelength and a flat background spectrum is acquired each time.

- **Reflection**

  This viewer depicts all images acquired in the Reflection imaging modality. On its right side has control buttons that change between the color image and the Ultra Violet reflection image. The color image can be useful for morphological measurements while the Ultra Violet image can be used to yield textures from the surface of the objects.

- **Fluorescence**

  This viewer depicts all images acquired in the Fluorescence imaging modality. On its right side has control buttons that change between the color images acquired with different excitation wavelengths (360, 405 and 450 nm). This is useful to observe the different stokes shift of the samples. Each material provides different fluorescence colors as a function of the excitation frequency.

- **Polarization**

  This viewer can be used to observe the Retardance pseudo color map as well as a gray-scale image that depicts the DOLP. On its right side has control buttons that change between the two different images. This is useful to observe the different retardations of each specimen.

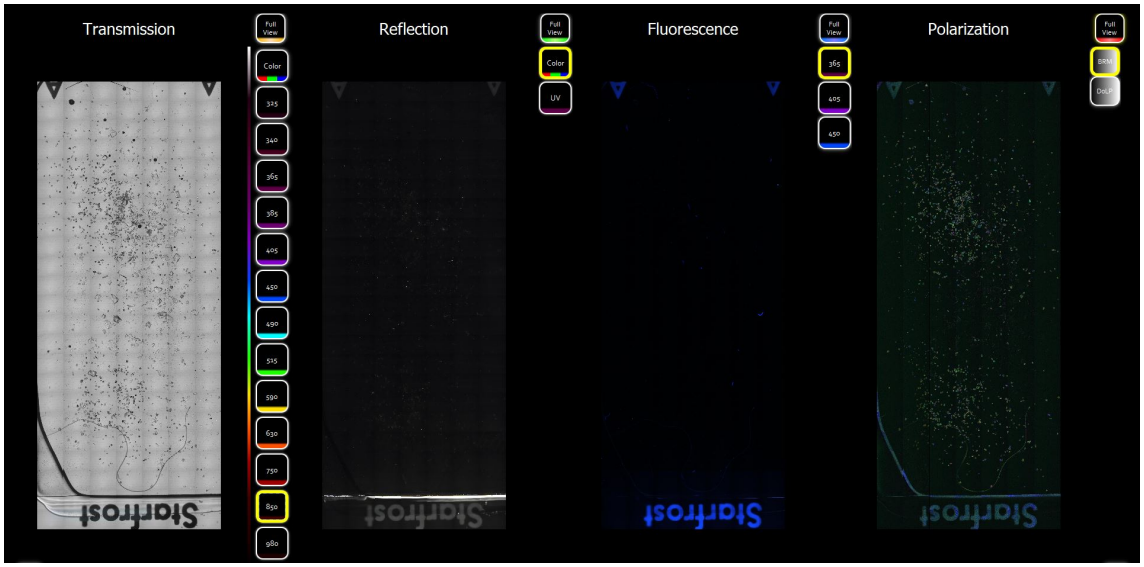

Figure 4.18: Overview Viewer: A complete ROI scanned in every imaging modality. It is a microscope glass slide, stitched together and the user can intuitively navigate through it by dragging the mouse. Advanced measuring and viewing can be performed while the system actively scans and attaches new frames to the overview.

The user can intuitively zoom in and navigate to the overview by grabbing the mouse. Navigating this way on the overview feels like using a digital maps application and is very user friendly. In Figure 4.20 we can see a sub-area of Figure 4.18 that is zoomed in and the features of the specimens can be observed in detail.

We can compare glass and sand samples as well as a human hair crossing the bottom left of the area. Sand has a big diversity between transparent, semitransparent and opaque and could otherwise labeld as glass. The use of the polarization imaging modality resolves the ambiguity since glass is always non birefringent while sand is.

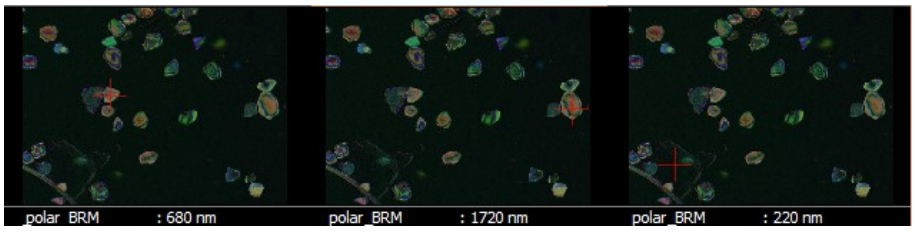

Figure 4.19: Retardance Measurements on various points. We can see sand particles having a range from 600 nm to 2000 nm retardance while glass has a much smaller ($\sim$ 200 nm).

Per-pixel retardance measurements shown in Figure 4.19 yield retardance values above 600 nm for sand particles, while glass is only 200 and is always “transparent” on the retardance map.

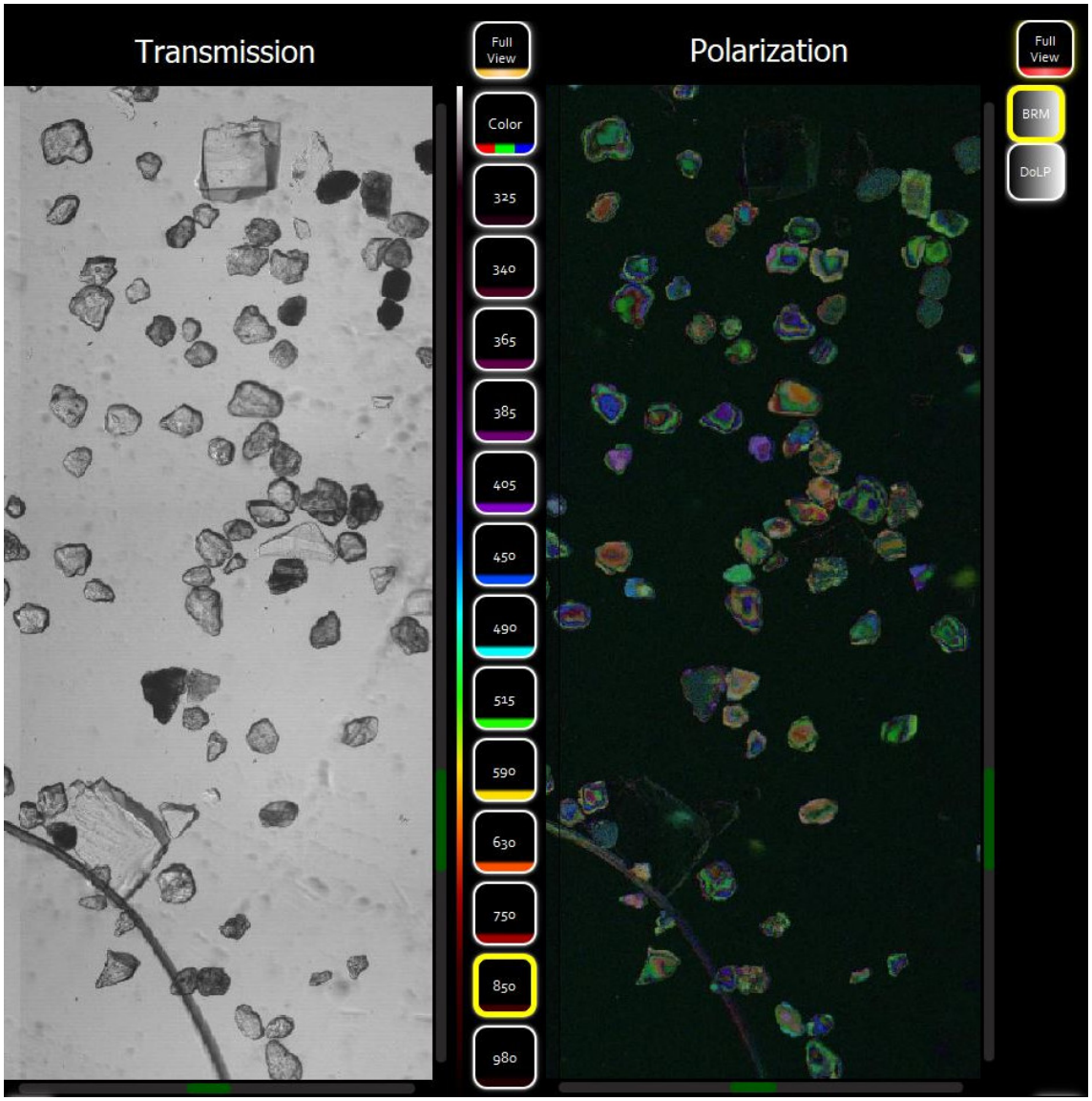

Figure 4.20: A zoomed area that depicts the retardation difference between sand and glass particles along side with a hair. One can see that glass has nearly zero birefringence (same as background) while sand has higher birefringence and gives beautiful interference colors. The hair also has a really low Fluorescence value.

4.4 Multi Modal Feature Space Analysis

Acquiring a full data set of a frame, is a bundle of useful information that awaits to be analyzed and processed. As discussed in previous chapters having the four *complementary* imaging modalities of Transmission (TR), Reflection (RE), Fluorescence (FL) and Polarization (POL) give a feature space that, for most of the cases, gives a certain differentiation factor between seemingly similar samples.

Although the data exists, there is no clear way of computationally and automatically differentiating one sample from another. We need to perform a **knowledge transfer**. This means that there exists a need to mimic the resolving process that the analyst is performing, and translate it algorithmically.

4.4.1 Knowledge Transfer Example

Let us now assume that we are an analyst at a forensic institute and a new, unknown to us, sample arrives at the laboratory. The main traces that could contribute to the crime discovery are human DNA samples such as **skin**, **blood** or **hair**, various environment specific features like **sand** or **glass** and if external data are provided such as description of what a suspect was wearing then such **fiber** discovery would be crucial.

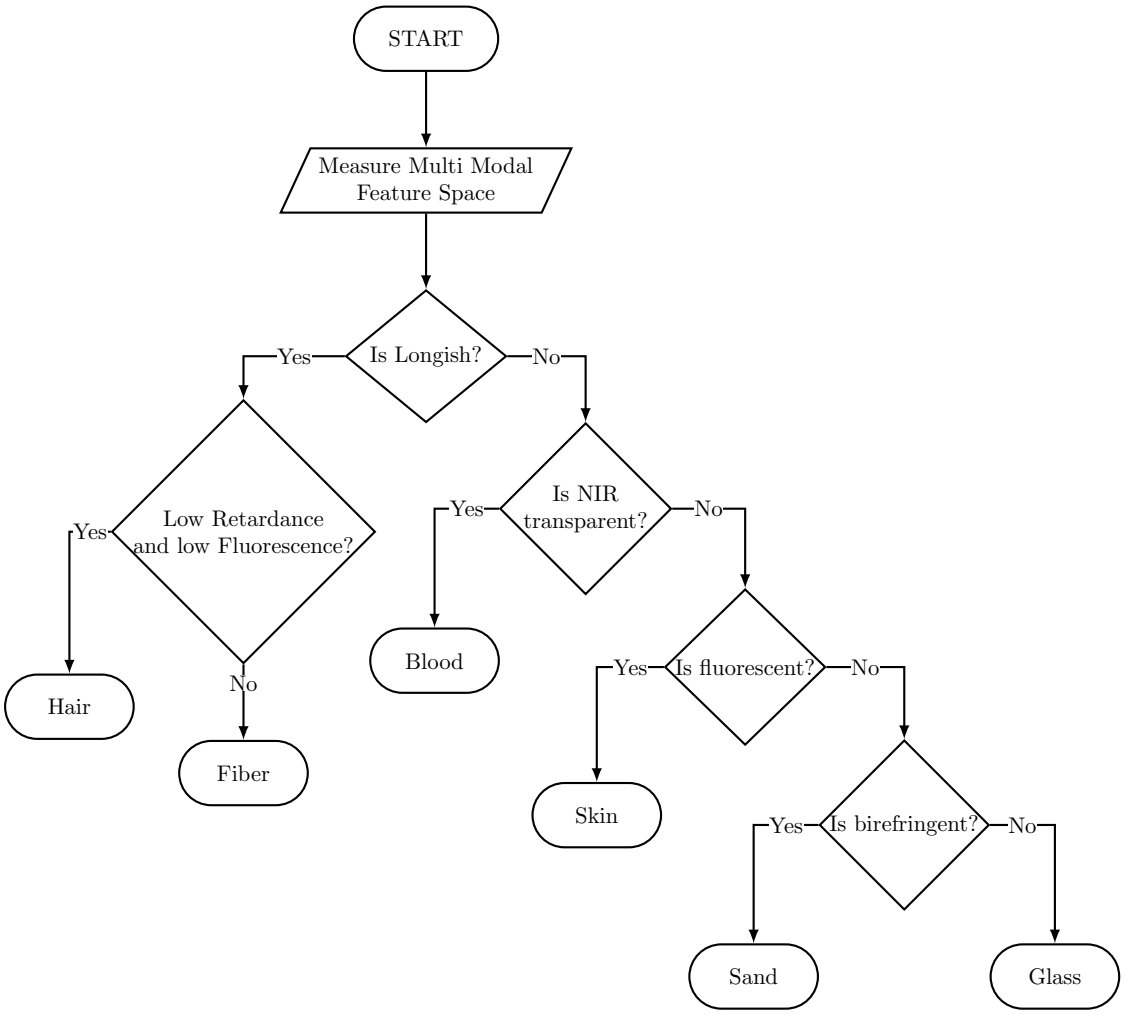

Figure 4.21: A decision table - like training file that utilizes the deterministic nature of the Multi Modal Feature Space to yield a decision for forensic trace analysis.

We can see that all modalities play a critical role to this example. If we had only

traditional HTS equipment which usually acquires Transmission and Fluorescence imaging, then the majority of the samples would yield an indecisive result. In the contrary, having Reflection imaging we can more easily distinguish morphological features, HSI in the transmission we can see features like the transparency of blood due to its spectra signature and Fluorescence to separate fluorescent and non fluorescent materials. Through our research we have found that Polarization imaging is complementary to the others and plays a critical role of differentiating between sand-glass and hair-fiber.

The crystalline structure of materials contributes as a major factor on recognizing them. This enables us to use thresholding techniques and perform **real-time analysis** without the use of stochastic models. This comes with a lot of benefits because the only "training" that the system needs is a simple instruction file in the form of Figure 4.21.

On the contrary, if we chose to walk the neural networks route, a lot of considerations would occur. 1) Initial training on the analysis software is most often a part of the purchased software package, and this training will prove invaluable to the users when setting up new trials or when doing spot-checking and trouble-shooting on the system. 2) Image analysis software and algorithms can be expensive to buy. Algorithms are also brand specific, so they must be purchased from the original supplier. This binds potential customers and if research is the selling point this should be avoided. 3) Optimization time is required to fine tune the algorithms for image analysis. Algorithms are designed with a certain task in mind, for example, to pick out individual traces. Adding a new class to a supervised model is very time consuming. 4) The software requires training for optimal use and accurate results. Although training is often included with the purchase of the software, any new staff will also need to be trained, either in-house or another training session needs to be purchased.

Finally, for all the aforementioned reasons and because the Neural Networks act like a black box that removes intuition from the researcher, we decided to design our analysis suite with deterministic algorithms that can be reconfigured by the end user, while also retaining the possibility of using Neural Networks by exporting the Multi Modal Feature Space.

4.4.2 Analysis Results and Comparison

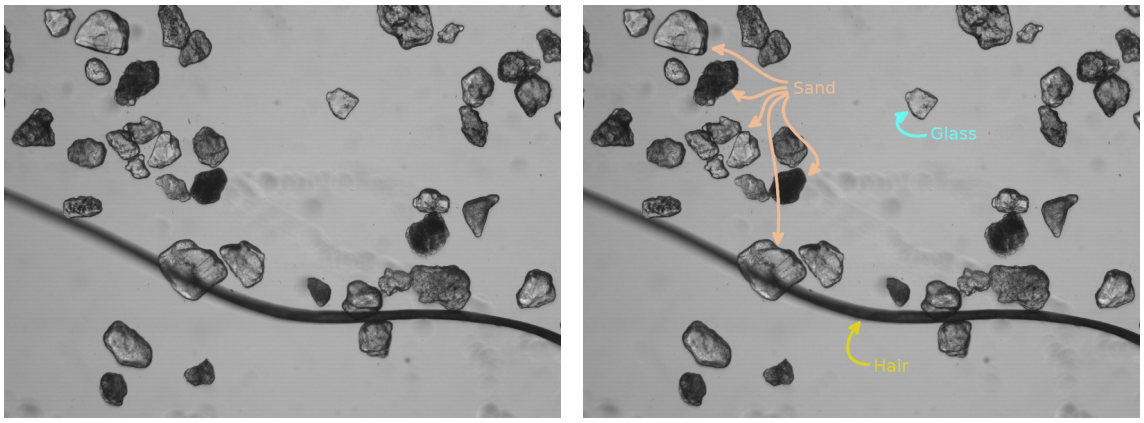

Figure 4.22: A reference image that will be used in the following section. The RAW transmission image at 450 nm is shown on the left, an annotation of the frame's samples is shown on the right.

The most of this frames specimens are *"silica sand"*, also known as quartz sand, and is very similar to glass due to its composition being mainly silicon dioxide (SiO_2). There is

an individual specimen of *"leaded glass"*, which is potassium silicate glass which has been impregnated with a small amount of lead oxide in its fabrication, and is really similar to quartz sand due to the fact that both substances are silica based. Lastly there is a longish specimen that is **"human hair"** and can be easily differentiated from sand and glass due to its morphology but not from a synthetic fiber.

As shown in the decision flow chart of Figure 4.21, retardance measurements play a critical role to differentiate between sand-glass and hair-fiber. Let us now try to analyze the frame of Figure 4.22, with and without the retardance measurements.

Without Retardance Measurement

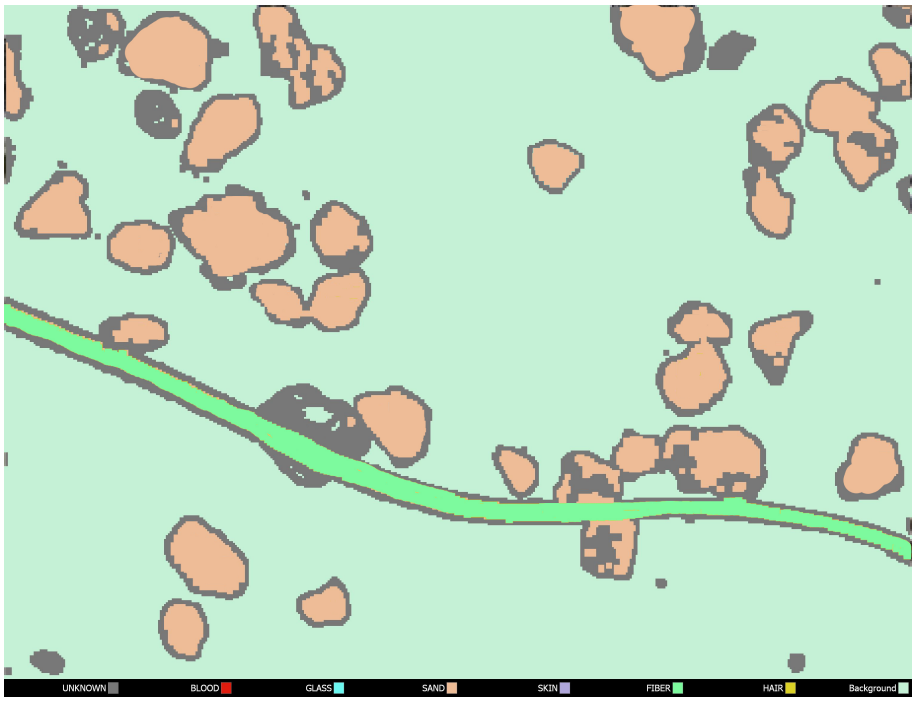

Figure 4.23: Analysis result **without** Retardance Measurement.

We can see that without retardance measurements the system can very easily confuse the glass specimen to be a sand one. It also confuses the human hair and identifies it as a synthetic fiber. That implies that the Multi Modal Feature Space is incomplete and an image modality misses. The addition of the Polarization imaging modality as it will be later demonstrated introduces an important dimensionality that will introduce a hyperplane of differentiation between the samples that are mixed up.

Avoiding this issue without the Polarization imaging modality may not be impossible but solving it with very strict parameters will introduce a bias factor to the decision flow that will lead to **data over-fitting**. This means that the training file with the thresholds on the decision table will have an observer bias and will not apply to a wide sample variety.

What we can see from Figure 4.23 is that through the calibration of the device we can have a nearly perfect background extraction despite dealing with semitransparent specimens. The background is extracted and highlighted with the low saturated light green color. The unknown samples are highlighted in gray and are the pixels that their feature space does not match any of our predefined classes. We usually see the border of each contour highlighted in gray due to the fact that objects have shadows introduced by the optics and the height of the glass slide. Those shadows do not match the threshold values of the predefined classes and thus labeled as unknown. The sand class is highlighted

with beige. The glass class (ciel) does not take into consideration the retardance values and thus the glass particle, as annotated in Figure 4.22, is miss-classified as sand.

With Retardance Measurement

As shown in Figure 4.17, we expect sand to be birenfringent while glass not. The same applies to fiber and hair identification. Synthetic fibers have a wide range of birefringence that mainly rely on fabrication procedures and molecule composition. Organic (human) hairs on the other side have a very specific range of birefringence. Depending on the magnification of the device the synthetic fibers can be differentiated from hairs morphologically and based on the texture, but a ground truth imaging modality that can be utilized to yield an accurate decision is Polarization. Due to the crystalline structure of lipid layers, any light transmitted from the organic hairs will have a small, yet measurable, DOP.

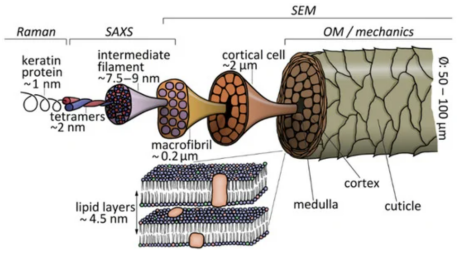

Figure 4.24: Hierarchical structure of hair under various magnifications. The size range accessible to the respective test method is also indicated in the figure.

Source: [26]

So if there exists a longish material in the MMFS that has non-zero but small retardance value, then we can be sure that this fiber is organic and not synthetic.

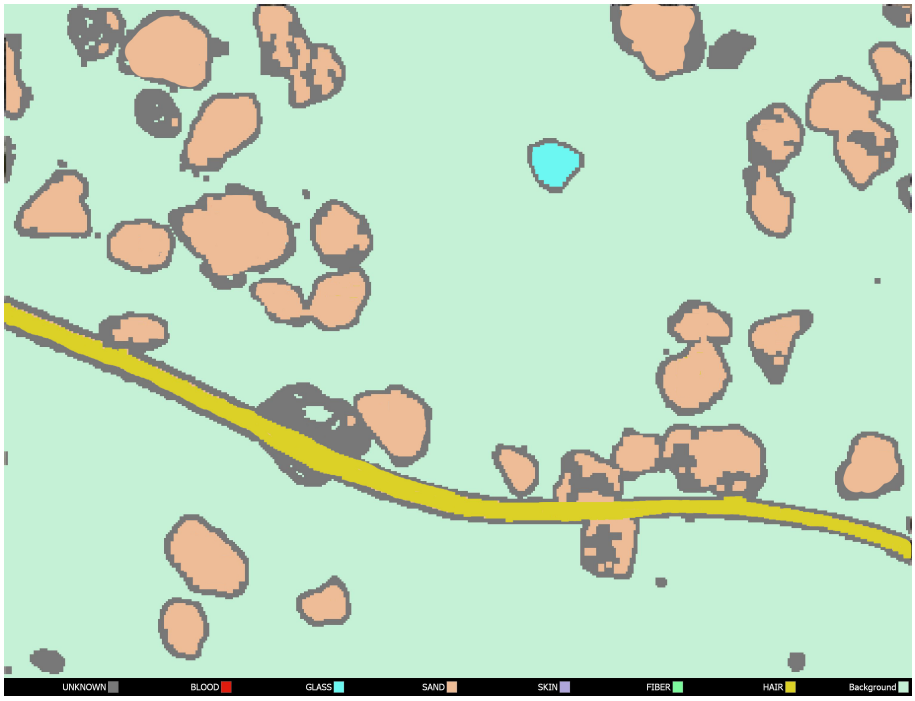

Figure 4.25: Analysis result **with** Retardance Measurement.

We can again observe a nearly perfect background extraction. The background is calculated by the self calibrated value in the spectral cube and visualized with the low saturated light green color. The same applies to the unknown class which is highlighted in gray and are the pixels that their feature space does not match any of our predefined classes. We can again see the border of each contour highlighted in gray due to the fact these objects have shadows introduced by the optics and the height of the glass slide. Those

shadows do not match the threshold values of the predefined classes and thus labeled as unknown.

The glass sample on the top center of the frame is now correctly classified. The classification algorithm now accounts the low retardation of this contour's MMFS and can easily differentiate it from the sand class. The same applies to the contour of the human hair. The classification algorithm that now has the retardance information combined with the low fluorescent blue color feature of the human hair and the longish contour, that was pre-labeled by the morphology analysis, can decide correctly for the class of that contour and label it as organic hair.

Chapter 5

Conclusions & Future Work

In this thesis, a real time birefringence mapping microscope was developed, as well as a novel retardance estimation technique and supervised specimen classification, based upon the Multi Modal Feature Space (MMFS) measurements from the microscope.

Conclusions

Concluding, what this thesis has to offer, is an experimentally validated real-time retardance measurement apparatus. Even though the trend nowadays is towards neural networks, the lack of application dependent Multi Modal (MM) datasets pushed us towards a novel development of a supervised classification technique that utilizes Multi Modal (MM) data to construct the optimal separating hyperplane. It was also shown for the first time, that rotation independence can be achieved in real-time retardance measurements and High Throughput Screening (HTS).

Future Work

As far as real-time retardance is concerned, future research will focus on the phase unwraping techniques and the robustness of the estimation algorithm, as well as the integration of real-time optical axis and specimen thickness measurements. Regarding classification technique for MMFS, future work would try to integrate reinforcement learning through relabeling and cross-validation training. Last but not least, measuring more spectral bands would make the device more robust and efficient for demanding application.

The application field may be wide for such devices. HTS may not only be applied to research centers, but for industry quality control for production pipelines that need to assure no stretch-induced birefringence. Furthermore, this technology can be utilized in agricultural industry for seed quality control and assurance. Lastly, a vary interesting field of application as discussed in [34], is to investigate the characteristics of birefringence in human sperm heads and apply polarization microscopy for sperm selection at intracytoplasmic sperm injection.

List of Figures

List of Tables

List of Abbreviations

A

AMO Atomic, Molecular, and Optical. 11
AWP Achromatic Wave Plate. 31

C

CCD Charge-Coupled Device. 51
CFA Color Filter Array. 51
CMOS Complementary Metal Oxide Semiconductor. 47, 52

D

DB Database. 57
DNA Deoxyribonucleic Acid. 67, 73
DOCP Degree Of Circular Polarization. 22
DOLP Degree Of Linear Polarization. 22
DOP Degree Of Polarization. 21, 76

E

EM Electromagnetic. 7

F

FL Fluorescence. 73
FPS Frames Per Second. 44
FWP Full Wave Plate. 29

G

GPGPU General-Purpose computing on Graphics Processing Units. 47
GPIO General Purpose Input/Output. 49
GPU Graphics Processing Unit. 56, 67, 68

H

HS Hyper Spectral. 1
HSI Hyper Spectral Imaging. 4
HTS High Throughput Screening. 1, 4, 58, 78
HWP Half Wave Plate. 29

I

IOT Internet Of Things. 55

L

LC Liquid Crystal. 60
LCP Left Circular Polarization. 15
LCTF Liquid Crystal Tunable Filter. 37
LDU Light Dividing Units. 40
LED Light-Emitting Diode. 44

M

MM Multi Modal. 1, 4, 58, 78
MMFS Multi Modal Feature Space. 1, 5, 58, 76, 77, 78
MS Multi Spectral. 47

N

NIR Near Infrared. 12, 44
nm nanometers. 43

O

OA Optical Axis. 33, 62

P

PoE Power Over Ethernet. 49
POL Polarization. 73
PSD Polarization State Detector. 1, 32, 58
PSG Polarization State Generator. 1, 32, 50, 58

Q

QE Quantum Efficiency. 54
QP Quadratic Programming. 63
QWP Quarter Wave Plate. 30

R

RCP Right Circular Polarization. 15
RE Reflection. 73
RGB Red Green Blue. 51
ROI Region Of Interest. 55

S

SMO Sequential Minimal Optimization. 63
SoC System on Chip. 49
SVM Support Vector Machines. 63

T

TCP Transmission Control Protocol. 49
TR Transmission. 73

U

UV Ultra Violet. 12

V

VIS Visible. 12, 44

References

[1] Elizabeth A. Wood. *"Crystals and Light"*. Dover Publications, 1977.

[2] W. Zhang. *"Phase-Matching in Nonlinear Optical Compounds: A Materials Perspective"*. Chemistry of Materials, 2017.

[3] NAVAL AIR WARFARE CENTER WEAPONS DIV POINT MUGU CA. *"Electronic Warfare and Radar Systems Engineering Handbook"*. 2013.

[4] Douglas B. Murphy. *"Birefringence Variations with Crystal Orientation"*. Olympus Microscopy, [Available Online]

[5] Sharma K. K. *"Optics: principles and applications"*. Academic Press, 2006.

[6] Collett E. *"Field Guide to Polarization"*. SPIE, 2005.

[7] N. P. Cheremisinoff. *"Condensed Encyclopedia of Polymer Engineering Terms"*. Butterworth-Heinemann, 2001, pp. 32-38.

[8] G. Boulon. *"Encyclopedia of Materials: Science and Technology" — "Nonlinear Optics: Molecular Engineering"*. Elsevier, 2001, pp. 6259-6264.

[9] Max M. Houck, Jay A. Siegel. *"Fundamentals of Forensic Science" — Chapter 15 - Textile Fibers*. Academic Press, 2012, pp. 381-404.

[10] Michael W. Davidson. *"The First Order (Full Wave) Retardation Plate"*. Olympus Microscopy, [Available Online]

[11] Stephen A. Nelson *"Interference Phenomena, Compensation, and Optic Sign."* Tulane University, 2014.

[12] J. G. Delly. *"The Michel-Lévy Interference Color Chart"*. Hooke College of Applied Sciences, 2012.

[13] J. van der Weerd, T. van Oijen. *"Spectrometric Imaging of Polarization Colors and Its Application in Forensic Fiber Analysis"*. Applied Spectroscopy, 2015.

[14] E. Hecht. *"Optics"*. Addison-Wesley, 2002.

[15] I.H. Shin, S.M Shin, D.Y. Kim. *"New, simple theory-based, accurate polarization microscope for birefringence imaging of biological cells"*. Journal of Biomedical Optics, 2010.

[16] R. O. Michael Shribak. *"Techniques for fast and sensitive measurements of two-dimensional birefringence distributions"*. Optical Society of America, 2003.

[17] R. Oldenbourg. *"Polarization microscopy with the LC-PolScope"*. Woods Hole, 2005, pp. 205-237.

[18] Y. K. Seiji Takeuchi. *"Method and Apparatus for measuring birefringence"*. USA Patent US 7,286,226 B2, 2007.

[19] M. F. A. Cacciani. *"A complete Stokes-meter"*. Solar physics, 1971, pp. 270-276.

[20] N. Theofanous, A. Arapoyianni. *"Effect of multiple reflections on retardation-based electro-optic measurements"*. J. Optical Society of America, 1991, pp. 1746-1754.

[21] Keikhosravi A., Shribak M., Conklin M.W. et al. *"Real-time polarization microscopy of fibrillar collagen in histopathology"*. Sci Rep 11, 2021.

[22] Freudenthal et al. *"Unambiguous Retardance Measurement"*. USA Patent US 0,091,416 A1, 2016.

[23] Spote A., Pierre-Jean T. et al. *"Joint demosaicing of colour and polarisation from filter arrays"*. Color and Imaging Conference, 2021, pp. 288-293.

[24] Flasseur O., Fournier C. et al. *"Self-calibration for lensless color microscopy"*. Applied Optics, 2017.

[25] Song J., Zeng N. et al. *"Stokes polarization imaging applied in monitoring dynamic tissue optical clearing"*. Biomedical Optics Express, 2021, pp. 4821-4836.

[26] Müllner ARM, Pahl R, et al. *"Different Structural Levels in Human and Yak Belly Hair and Its Effect on Hair Dyeing"*. Molecules, 2020.

[27] Eibe Frank, Mark A. Hall, and Ian H. Witten. The WEKA Workbench. Online Appendix for *"Data Mining: Practical Machine Learning Tools and Techniques"*. Morgan Kaufmann, 2016.

[28] S.K. Shevade, S.S. Keerthi, C. Bhattacharyya, K.R.K. Murthy. *"Improvements to the SMO Algorithm for SVM Regression"*. IEEE Transactions on Neural Networks, 1999.

[29] Ron Kohavi: *"The Power of Decision Tables"*. 8th European Conference on Machine Learning, 1995, pp. 174-189.

[30] Geoffrey Holmes, Mark Hall, Eibe Frank. *"Generating Rule Sets from Model Trees"*. Twelfth Australian Joint Conference on Artificial Intelligence, 1999, pp. 1-12.

[31] Leo Breiman. *"Random Forests"*. Machine Learning, 2001, pp. 5-32.

[32] John G. Cleary, Leonard E. Trigg. *"K*: An Instance-based Learner Using an Entropic Distance Measure"*. 12th International Conference on Machine Learning, 1995, pp. 108-114.

[33] Slikboer E. *"Investigation of Plasma Surface Interactions using Mueller Polarimetry"*., Université Paris Saclay, 2018.

[34] Gianaroli L, Magli MC, et. al. *'B. Sperm head's birefringence: a new criterion for sperm selection"*. Fertil Steril, 2008.